ISSN 1016-197X

Nuclear Science and Applications

Volume 30 Number 1 & 2 June, December 2025

The Journal of
BANGLADESH ATOMIC ENERGY COMMISSION

CONTENTS

NUCLEAR SCIENCE AND APPLICATIONS VOLUME 30 NUMBER 1 & 2 June, December 2025

Comparative Study for Beam Quality of High Energy Linear Accelerator with Monte Carlo Code PHITS

M.I. Hossain[1], A. Tabassum[1], J. Sarker[1], M. Khan[1], M.M. Rahman[2], M.F. Rabby[2], R. Ahmed[2], M.M. Islam[3,5] H. Watabe[4] and M.R. Islam[5*]

[1]*Department of Physics, University of Rajshahi, Rajshahi-6205, Bangladesh*
[2]*TMSS Cancer Center, Bogura, Bangladesh*
[3]*Department of Physics, Mohammadpur Kendriya College, National University, Dhaka, Bangladesh*
[4]*Research Center for Accelerator and Radioisotope Science, Tohoku University, Sendai, Miyagi, Japan*
[5]*Institute of Nuclear Medical Physics, Atomic Energy Research Establishment,Bangladesh Atomic Energy Commission, Savar, Dhaka, Bangladesh*

Abstract

The precision of radiotherapy is essential for successful cancer treatment. This study confirms the beam quality of high-energy photons (10 MV and 15 MV) from a Varian Vital Beam linear accelerator using the Particle and Heavy Ion Transport code System (PHITS). A detailed model of the LINAC head, including the tungsten target, primary collimator, flattening filter, and secondary jaws, was implemented in PHITS. Simulations were done to calculate percentage depth dose (PDD) curves and beam profiles for a 10×10 cm² field at a 100 cm source-to-surface distance (SSD). The results were benchmarked against measured data from a clinical Vital Beam system. The simulated PDD curves showed excellent agreement with the measurement, with d_{max} values of 2.5 cm for 10 MV and 3.5 cm for 15 MV. Beam profile analysis yielded flatness (2.43-4.20%) and symmetry (0.76-0.99%) values within the clinical tolerance limits stipulated by AAPM guidelines. This work confirms the efficacy of PHITS as a reliable tool for independent beam data validation and quality assurance in modern radiotherapy.

Keywords: Cancer, Radiotherapy, Linear Accelerator, Beam Quality Assurance, PHITS.

1. Introduction

Cancer is still one of the major causes of illness and death globally, creating ongoing challenges for healthcare systems. According to the National cancer institute (NCI),"Cancer is a disease in which some of the body's cells grow uncontrollably and spread to other parts of the body" [1-2]. After the discovery of X-rays in 1895, by Wilhelm Conrad Röntgen from Germany, its clinical usefulness as a means of cancer treatment was first appreciated [3]. Since the discovery of X-rays, radiation therapy has continually advanced, evolving from the utilization of cobalt-60 sources to modern linear accelerator systems. Among all radiotherapy technologies, the linear accelerator (LINAC), often regarded as a heroic figure in modern radiotherapy, is a highly effective machine that delivers precise, high-energy beams (typically 6 MV to 25 MV). Due to high energy, their penetrating ability and relatively precise beam shaping capabilities make them highly effective in achieving conformal dose distributions. This machine gives treatment to patients in various modalities such as three-dimensional conformal radiotherapy (3DCRT), intensity modulated radiotherapy (IMRT), volumetric modulated arc therapy (VMAT) etc. Very recent, with the advent of modern technology, flattening filter-free (FFF) facility is added to the LINAC to give the high dose within a very short time [4].

On the other hand, one of the key aspects of radiotherapy is accurate characterization of the therapeutic photon beam. The depth-dose distribution within a medium, typically represented by the percentage depth dose (PDD), is essential for quantifying how the x-ray beam attenuates as it traverses tissue-equivalent material. Equally important is the beam profile, which provides information about the spatial distribution of dose across the field, enabling assessment of beam flatness and symmetry. Together, PDD and beam profiles form the foundation for beam commissioning, quality assurance, and treatment planning system (TPS) validation in radiotherapy. The accuracy of the TPS is fundamentally dependent on the input beam data-primarily percentage depth dose (PDD) curves and beam profiles-characterizing output. TPS can determine the amount and direction of radiation exposure needed to match the desired dose while minimizing the dose to healthy tissue around it [5].

The main goal of radiation therapy is to deliver the highest dose to the tumor while maintaining minimum dose to the surrounding healthy tissues [6]. To achieve this purpose, the dose distribution in the treatment area must be calculated and verified by an accurate method [7]. Monte Carlo (MC) simulation is an accurate and detailed method for simulating complex source configurations and geometries in radiotherapy [8]. While experimental measurement is the clinical standard, Monte Carlo (MC) simulations have emerged as a powerful tool for validating beam models. MC methods simulate the random nature of radiation transport and interactions, providing a first principles calculation of dose deposition [9]. The Particle and Heavy Ion Transport code System (PHITS) is a general purpose MC code that excels in simulating the transport of various particles, including photons and electrons, over a wide energy range [10]. Its advantages include precise geometry modeling and advanced visualization features, making it

*Corresponding author: mripbaec@gmail.com

highly effective for simulating complex LINAC head structures.

However, this study aims to utilize the PHITS code to simulate the photon beam output of a Varian VitalBeam LINAC at 10 MV and 15 MV, and validates its accuracy by comparing simulated and measured clinical data for key dosimetric parameters, including percentage depth dose (PDD) and beam profiles at different depths.

2. Materials and Methods

In this study, a Varian Vital Beam linear accelerator at Thengamara Mohila Sabuj Sangha (TMSS) Cancer Center, Bogura, Bangladesh was used as a radiation energy source. This machine provides two photon energies (10 MV and 15 MV) and five electron energies (4, 6, 9, 12, and 18 MeV). In this work, 10 MV & 15 MV photon beam was measured and simulated to evaluate their dosimetric characteristics. The PHITS code was installed on a computer with Intel core i7 2450 M CPU and 1.8 GHz processor, the operating system windows 10 version 10.0.19045 and the system type 64 bit. The installed physical memory (RAM) is 16.0 GB.

2.1. PHITS Monte Carlo Code

The application of the Monte Carlo (MC) method in radiation therapy was first postulated by Mackie and Battista [11], since that time MC method has been used in many areas including radiation dosimetry, treatment machines, and treatment planning calculations. MC method is a powerful tool for the study of the effect of LINAC head components on dosimetric characteristics of photon and electron beams [12]. By the time of advancement of radiotherapy, Several Monte Carlo based codes have been developed, including Fluka, MCNP, Geant4, EGSnrc and Penelope. But in application, the results vary due to differences in computational systems and in nuclear data libraries included with the respective MC packages [13]. One limitation of MCNP is that it does not provide direct visualization of particle trajectories. Meanwhile, Geant4 and Penelope are usable only for specific energy ranges. But PHITS is capable of visualizing particle trajectories and specific energy ranges.

The traces of particle tracking can be visualized using the Particle and Heavy Ions Transport code System (PHITS), a nuclear simulation program developed by the Japan Atomic Energy Agency (JAEA). The PHITS program is suitable for simulating both charged and neutral particles. It is also equipped with a tally that can visualize particle traces in two dimensions and calculate physical quantity of interest [14].

In this study, PHITS is used to clearly show how X-rays are produced in the LINAC and to better calculate the PDD curve and beam profiles. Accurate results for these values are necessary before the LINAC can be safely used for treatment.

2.2. LINAC Head Modeling and Simulation Setup

In the context of LINAC-based photon beams, Monte Carlo simulations allow for highly accurate modeling of treatment head components such as the target, flattening filter, collimators, and multi-leaf collimators, all of which significantly influence the resulting beam quality.

The geometry of the VitalBeam treatment head was meticulously modeled within the PHITS (version 3.35) environment. The design of the LINAC head is important, as it is the part of the machine where X-ray photons are generated. However, the process of LINAC head modeling shown in Fig. 1(a), while Fig. 1(b) and Fig. 1(c) illustrates both 2D and 3D view of LINAC head. The simulation included all important components that significantly influence the beam's characteristics:

- **X-ray Source & Target:** A circular source was defined. Electrons with a 1 mm radius beam were directed onto a cylindrical tungsten target.
- **Primary Collimator:** A conical tungsten block designed to define the initial beam divergence.
- **Flattening Filter (FF):** A conical filter made of stainless steel was modeled to flatten the naturally forward-peaked photon beam.
- **Secondary Collimators (Jaws):** Two pairs of movable jaws (X and Y) were implemented using PHITS's [transform] section to allow rotation and define a precise 10×10 cm² field at the isocenter.
- **Water Phantom:** A cubic water phantom (30×30×30 cm³) was placed at a source-to surface distance (SSD) of 100 cm. Water is the standard medium for reference dosimetry due to its tissue-equivalence.

For simulation setup, the number of simulated particle histories, crucial for statistical accuracy, was controlled by the maxcas (histories per batch) and maxbch (number of batches) parameters. A total of 5.0×10^7 particle histories were simulated, implemented as 1.0×10^6 histories per batch with 50 batches in PHITS, resulting in statistical uncertainties below 2%. The field size was: 10×10 cm², SSD = 100 cm. The incident particles were electrons with energy 10 MV and 15 MV. Key tallies were used to assess physical quantities: T-Track for visualizing particle trajectories, *T-Deposit* for calculating dose in the water phantom, and *T-Cross* for scoring particles across planes to derive beam profiles. To visualize particle tracks, *track_yz.out* file and *track_xy.out* were defined as well as *OCR.out* and *PDD.out* were also defined to record beam profiles and PDD respectively.

2.3. PDD and Beam Profiles Measurement

In radiotherapy treatment planning process, quality assessment (QA) is indispensable for achieving accuracy and avoidance of treatment errors [15]. Percentage depth dose (PDD) provides information about the dose variation with depth along central-axis and beam profile give information about dose variation across the field at a given depth. To achieve this purpose, the primary dosimetric parameters namely PDD, beam profile, flatness and symmetry is measured by Varian VitalBeam LINAC using two photon energy.

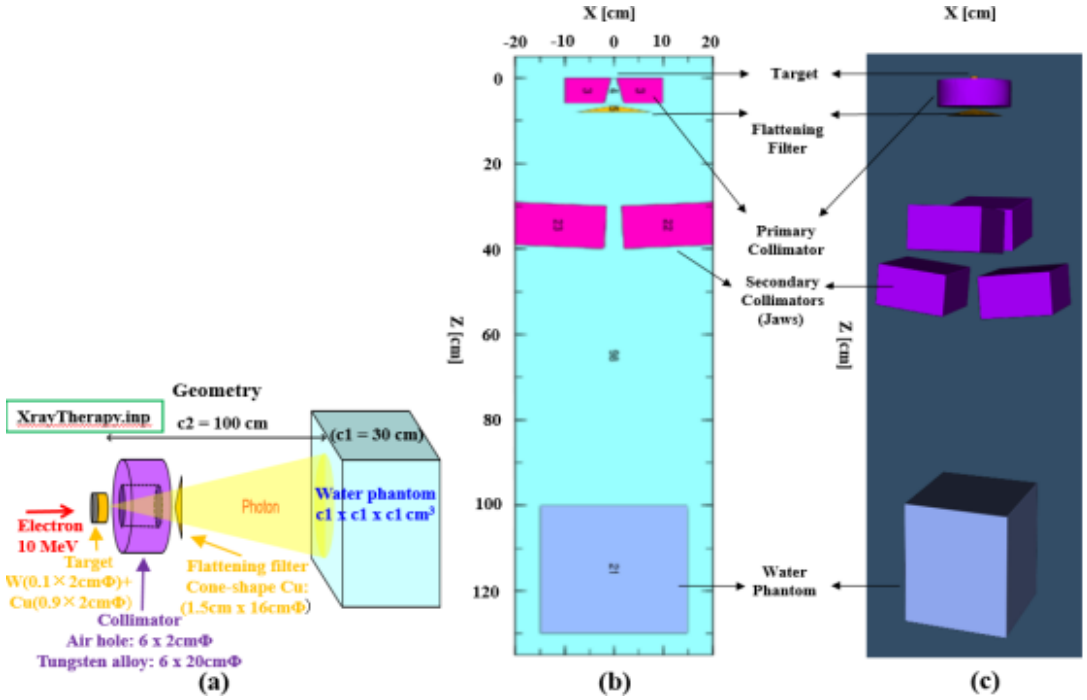

Fig. 1: (a) Indicates how the geometry defined, (b) represents 2D and (c) 3D LINAC head and water phantom modeling with PHITS code.

The dose data was normalized to 100% at the depth of maximum dose (d_{max}). The PDD was calculated using equation -1:

$$\text{PDD (d)} = 100 \times \frac{D_d}{D_{dmax}} \qquad (1)$$

Where, D_d is absorption dose at the depth d and D_{dmax} is the maximum absorption dose.

At the same time, beam profile was calculated as the ratio of the dose at an off-axis point to the dose on the central axis at the same depth. Beam flatness and symmetry were quantified within the central 80% of the field size according to the American Association of Physicists in Medicine (AAPM) Task Group guidelines [16].

The flatness and symmetry was calculated using the standard formula equation-2 and equation-3:

$$\text{Flatness} = \frac{D_{max} - D_{min}}{D_{max} + D_{min}} \times 100\% \qquad (2)$$

D_{max} = maximum dose in the defined central region, D_{min}= minimum dose in that same region

$$\text{Symmetry} = \frac{\text{Area}_{left} - \text{Area}_{right}}{\text{Area}_{left} + \text{Area}_{right}} \times 100\% \qquad (3)$$

Where, Area_{left} and Area_{right} are the areas bounded by the profile on the left and right of the beam central axis.

3. Results and Discussion

3.1. 2D and 3D Simulated Particle Tracking

Two-dimensional (2D) particle tracking distribution in the vertical (XZ plane) of the LINAC head and water phantom obtained from PHITS code are shown in Fig. 2.The interaction of accelerated electrons with the target results in the production of X-ray photons which subsequently traverse the primary collimator, flattening filter, secondary collimator, and finally enter the water phantom, as shown in Fig. 2(a). The photon flux reaches its highest near the target at about 10^{-1} p/cm²·s (red) and progressively reduces with distance, dropping to approximately 10^{-10} p/cm²·s (light blue) at the phantom surface.

The electrons tracking shown in Fig. 2(b), this track shows how secondary electrons are produced and move through the system. The highest electron density is observed near the target and flattening filter, where photon interaction produce a cascade of electrons. As these electrons move downward, they scatter in different directions and lose energy. This can be seen in the faint green areas spreading into the phantom.

The Fig. 2(c) shows the neutron track produced mainly photonuclear reactions at high photon energies (above 10 MeV). The green lines indicate where neutrons are generated, mostly within the upper parts of the LINAC head, such as target and collimators. The neutron intensity inside the phantom is very low, meaning that neutrons add little to the patient's dose.

According to the modeling, the interaction of electrons with the target produces X-ray photons **(**mainly bremsstrahlung photons**)** and secondary electrons are produced when photons interact with materials (target, flattening filter, collimator, phantom) [17]. Photons travel longer than electrons because electrons are charged particles.

At the same time, secondary charged particle like electrons are produced. Photon beams from radiotherapy units, are no longer pure photon beams, but a mixture of photons and a small amount of electrons produced by the photon beams [18]. This is called electron contamination. These electrons deposit dose near the surface, affecting the surface and build-up region dose.

Medical LINACs which operate above 10 MV for high energy photon therapy inevitably produce neutron contamination [19]. The contribution of neutron contamination from the primary collimator in producing neutrons is about 55-60% of the total neutrons generated from the interaction of photons with LINAC head components [20]. The contribution of neutrons to the total dose in high energy radiotherapy is small but biologically notable [21].

Overall, the figure shows how primary and secondary particles move and interact in a medical LINAC system. It helps us to understand how energy is transported and how secondary radiation is produced, which is important for accurate dose calculation.

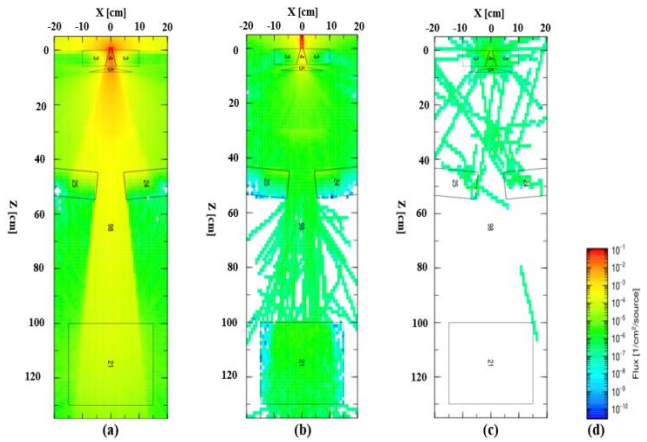

Fig. 2: 2D particle tracking with PHITS code; (a) photon, (b) secondary electron, (c) neutron track respectively. The color scale (d) represent the flux intensity.

Another advantage of PHITS is its ability to generate 3D view of particles tracking. Fig. 3(a) illustrates the combined simulated particle trajectories originating from the LINAC head. The cyan rays Fig. 3(b) and red rays Fig. 3(c) indicates the trajectories of photon and secondary electrons respectively.

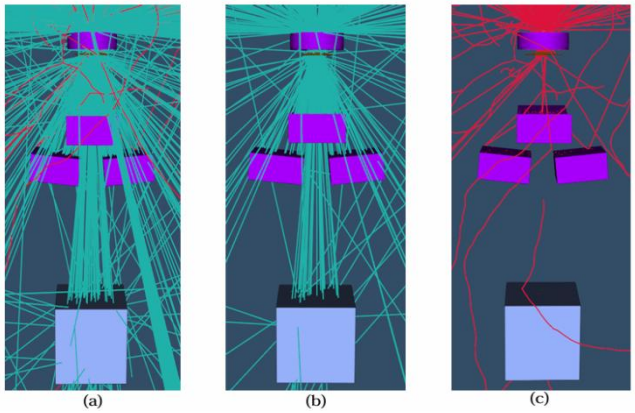

Fig. 3: (a) Represent combined simulated 3D particle tracking, while (b) photon, (c) electron tracking shown separately with PHITS.

3.2. Percentage Depth Dose (PDD) Analysis

Fig. 4(a) and Fig. 4(b) represent measured (orange) and simulated (blue) PDD curves for 10 MV and 15 MV photon beams in a water-equivalent phantom, respectively. The maximum dose for 10 MV and 15 MV beam energy with a 10×10 cm² field size is reached at depths of 2.5 cm, and 3.5 cm, respectively. The dose rises sharply from the surface to the depth of maximum dose (d_{max}) due to electron buildup. The measured data and the PHITS simulation agree well in the build-up region and around the depth of maximum dose (~102–104 cm). Beyond this depth, the dose gradually decreases with increasing depth due to photon attenuation and reduced scatter. Slight deviations are observed at greater depths (>120 cm), where the simulated dose falls slightly below the measured values, likely due to modeling or statistical uncertainties in the simulation.

A comparison of d_{max} and PDD at 10 cm depth for 10 MV and 15 MV photon energies, as calculated by the PHITS code and measured data reported in the British Journal of Radiology (BJR)-25 data, are shown in Table-1. In this study, the simulation geometric model and materials were same as reference data. Both the values of d_{max} and PDD measured in this study found strong agreement with those report in BJR-25 supplement [22]. However, measured results and PHITS simulations match BJR-25 trends in the build-up and mid-depth regions, while differences at large depths are due to PHITS scatter and beam modeling.

Table 1: Comparison of d_{max} and PDD at 10 cm depth (D_{10}) with BJR-25 reference data.

Energy	Field Size (cm²)	This Study (PHITS)		BJR-25	
		d_{max} (cm)	D_{10} (%)	d_{max} (cm)	D_{10} (%)
10 MV	10×10	2.5	72.25	2.1	73.0
15 MV	10×10	3.5	75.25	3.3	77.0

The simulated PDD curves Fig. 4(a) and Fig. 4(b) match well with measured data, confirming that PHITS correctly represents central-axis dosimetry, including build-up and

photon attenuation. Minor differences observed in the deeper region of the phantom may arise from uncertainties in LINAC head details, simulation noise, or geometry simplifications. Still, the agreement of d_{max} and D_{10} with BJR-25 data supports the model's accuracy.

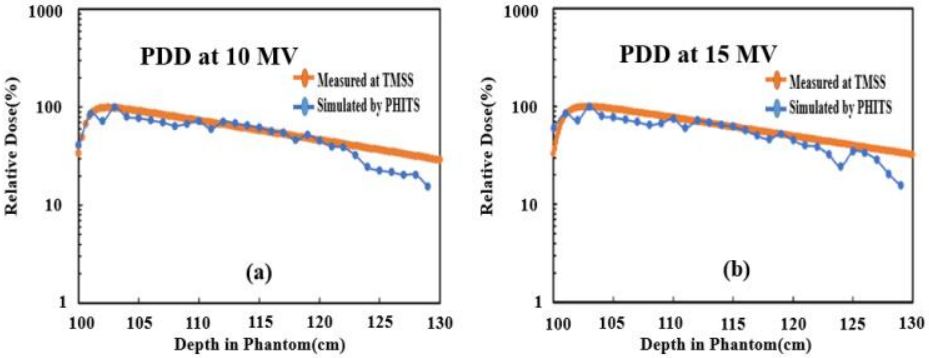

Fig. 4: Comparison of measured and PHITS simulated PDD curves for the photon beam of (a) 10 MV and (b) 15 MV (where field size 10×10 cm², SSD=100 cm).

3.3. Beam Profile Analysis

Similarly, the beam profiles at a specific depth is the ratio of the absorbed dose at an off-axis point (a point away from the central beam axis) to the dose at the central axis. The lateral beam profiles showed remarkable agreement between simulation and measurement for both energies. Monte Carlo data is plotted as blue triangle, while experimental measurements are plotted as an orange circle. The profiles exhibit the characteristic flat central region and sharp dose fall-off in the penumbra. Our beam profiles result observed at beam energy 10 MV by PHITS code system is compared with the measured data from TMSS at 5 cm, 10 cm, 20 cm and 30 cm depth from the surface of the water phantom are shown in Fig. 5(a) to Fig. 5(d), respectively.

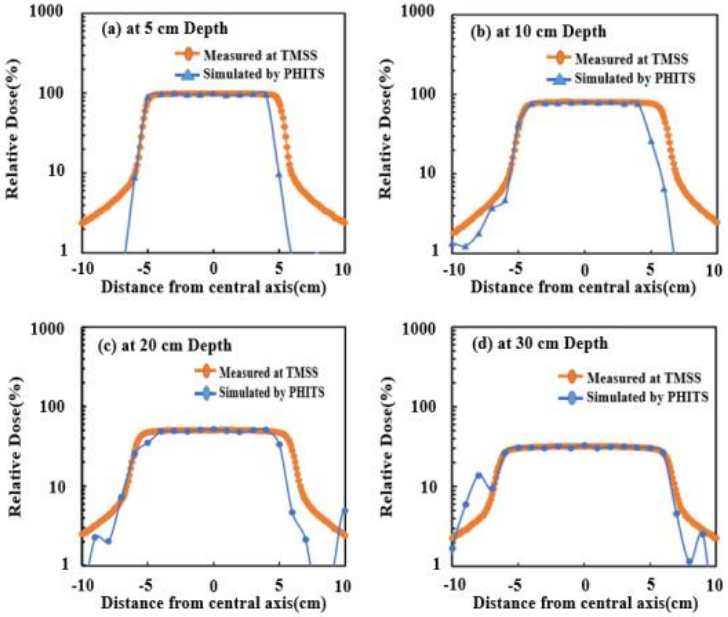

Fig. 5: Simulated and measured cross-line profiles for the 10 MV beam at (a) 5 cm depth, (b) 10 cm depth, (c) 20 cm depth and (d) 30 cm depth respectively.

Similarly, beam results simulated (blue circle) with the PHITS code system for 15 MV beam energy were compared with experimental measurements (orange circle) obtained from TMSS. The comparisons were conducted at depths of 5 cm, 10 cm, 20 cm, and 30 cm in the water phantom, offering insight into dose distribution behavior. The findings are illustrated in Fig. 6(a) to Fig. 6(d) respectively.

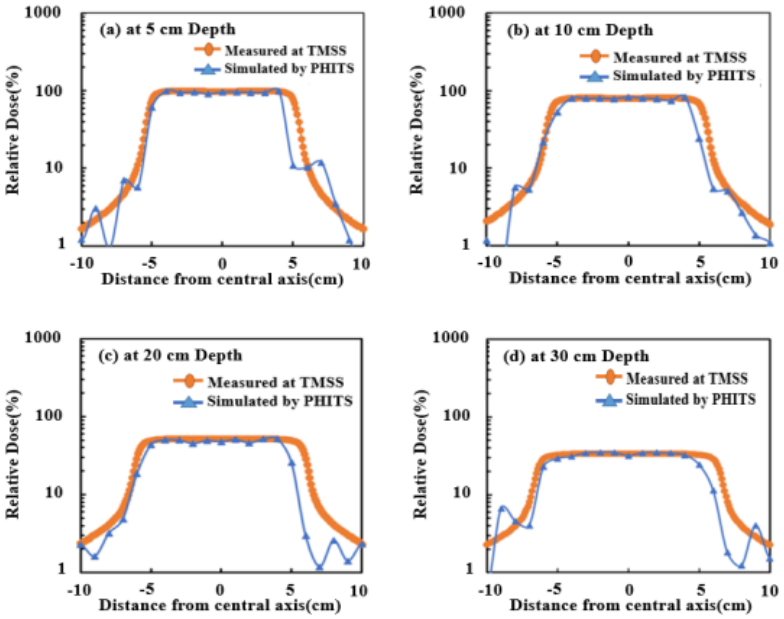

Fig. 6: Simulated and measured cross-line profiles for the 15 MV beam at (a) 5 cm depth, (b) 10 cm depth, (c) 20 cm depth and (d) 30 cm depth respectively.

Table-2 presents a summary of the findings, including the flatness and symmetry parameters obtained from the complete set of beam profiles. All values are well within the clinical tolerance limits recommended by AAPM TG-40 [23] (typically ±3% for symmetry and ≤5% for flatness). For both energy flatness increases with depth, indicating broader dose distribution due to scatter contribution. Symmetry slightly decreases with depth, showing a small lateral imbalance in dose uniformity at deeper depths. Lateral imbalance at deeper depths arises from increased photon scatter and loss of beam uniformity as the beam spreads laterally in the phantom. Small shifts and kinks are enhanced by low dose levels and statistical uncertainty in Monte Carlo calculations. Minor geometric simplifications in the LINAC head can also contribute to these effects.

Table 2: Beam flatness and symmetry analysis at various depths for a 10×10 cm² field.

Depth (cm)	10 MV		15 MV	
	Flatness (%)	Symmetry (%)	Flatness (%)	Symmetry (%)
5.0	2.53	0.93	2.43	0.99
10.0	2.67	0.90	2.70	0.94
20.0	3.83	0.82	3.82	0.84
30.0	4.11	0.77	4.20	0.76

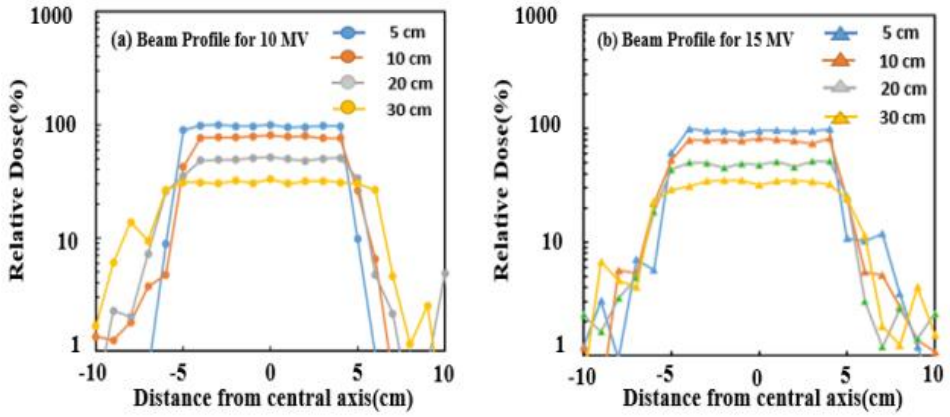

Fig. 7: Beam profile curves for (a)10 MV beam energy and (b)15 MV beam energy simulated by PHITS

The combined beam profiles results at depths of 5 cm, 10 cm, 20 cm and 30 cm are shown in Fig. 7(a) and Fig. 7(b) for 10 MV beam energy and 15 MV beam energy, respectively. For comparison, the results at 5 cm depth have been considered as 100% dose. The corresponding off-central axis dose profiles Fig. 7(a) and Fig. 7(b) exhibit uniform dose distribution within the central 80% field region and steep fall off near the penumbra, confirming good beam collimation. The 15 MV beam shows slightly higher flatness values than 10 MV, consistent with its greater penetration and scatter.

Increasing flatness with depth suggests enhanced scatter at higher penetration. Both 10 MV and 15 MV beams demonstrate consistent uniformity suitable for radiotherapy applications. This study shows that the PHITS Monte Carlo code can accurately model and validate a clinical LINAC beam.

4. Conclusion

The PHITS Monte Carlo code has been effectively utilized to model a Varian VitalBeam LINAC and validate the quality of its 10 MV and 15 MV photon beams. The simulated PDD curves and beam profiles showed excellent agreement with measured clinical data, and all derived beam parameters (d_{max}, flatness, symmetry) were within accepted clinical tolerances.

This work establishes PHITS as a reliable and accurate tool for independent beam data verification and dosimetric audit in radiotherapy. It provides a strong foundation for future applications, such as modeling more complex treatments using multi-leaf collimators (MLCs), integrating patient-specific computed tomography (CT) anatomies for personalized dose calculation, and performing independent audits for advanced treatment techniques like IMRT and VMAT, thereby enhancing the overall safety and efficacy of radiotherapy.

5. References

1. National Cancer Institute. What is cancer? Available from: https://www.cancer. gov/about-cancer/understanding/what-is-cancer.
2. Brown JS, Amend SR, Austin RH, Gatenby RA, Hammarlund, Emma U, Pienta KJ. Updating the definition of cancer, Mol. Cancer Res., **21**, 1142-1147 (2023).
3. Baskar R, Lee KA, Yeo R, Yeoh KW. Cancer and radiation therapy: current advances and future directions, Int. J. Med. Sci., **9**, 193-199 (2012).
4. Uddin MF, Begum M, Ahmed M, Atiquzzaman M, Osman H, Tamam N, Sulieman A, Akter S, Khandaker MU. Radiation safety and shielding evaluation of newly installed medical LINAC facility in Bangladesh, J. Rad. Res. Appl. Sci., **17**, 100844 (2024).
5. Fardela R, Candra ES, Milvita D, Mardiansyah D, Ridwan R, Diyona F, Mousa A. Assessment of LINAC Source Radiation Dose around Healthy Organs Using Treatment Planning System Calculation, J. Mul.dis. Appl. Nat. Sci., **5**(2), 398-407 (2025).
6. Makrani DS, Hasanzadeh H, Pourfallah TA, Ghasemi A, Jadidi M, Babapour H. Determination of primary electron beam parameters in a Siemens Primus Linac using Monte Carlo simulation, Archi. Adv. in Bio-sci., **6**, 75-79 (2015).
7. Aljamal M, Zakaria A. Monte Carlo modeling of a Siemens Primus 6 MV photon beam linear accelerator. Australian Journal of Basic and Applied Sciences, Aust. J. Basic & Appl. Sci., **7**, 340-346, (2013)
8. Ibitoye ZA, Adedokun MB, Orotoye TA, Udo GB. Design and evaluation of structural shielding of a typical radiotherapy facility using EGSnrc monte carlo code, J. Med. Phy., **47**, 27-33 (2022).
9. Spezi E, Lewis G. An overview of Monte Carlo treatment planning for radiotherapy, Radia. Pro. Dosi., **131**, 123-129 (2008).
10. Sato T, Iwamoto Y, Hashimoto S, Ogawa T, Furuta T, Abe SI, Kai T, Tsai PE, Matsuda N, Iwase H, Shigyo N. Features of particle and heavy ion transport code system (PHITS) version 3.02, J.Nuc. Sci. Tech., **55**, 684-690 (2018).
11. Mackie, TR, and Battista JJ. A macroscopic Monte Carlo method for electron beam dose calculations: a proposal. the use of computers in radiation therapy. Proceedings of the eight ICCR, Toronto, Canada (1984).
12. Mesbahi A, Mehnati P, and Keshtkar A. A comparative Monte Carlo study on 6MV photon beam characteristics of Varian 21EX and Elekta SL-25 linacs, Iran. J. Radiat. Res., **5**, 23-30 (2007).
13. Fiak M, Fathi A, Inchaouh J, Khouaja A, Benider A, Krim M, Harakat N, Housni Z, Bouhssa ML, Mouadil M, Elabssaoui Y. Monte Carlo Simulation of a 18 MV Medical Linac Photon Beam Using GATE/GEANT4, Mos. Uni. Phy. Bull., **76**, 15-21 (2021).
14. Bilalodin B, Haryadi A, Haryanto B. Simulation of Neutron Contamination From Medical Linac Using Particle And Heavy Ions Transport Code System (PHITS),Indo. J. Appl. Phy., **12,** 258-265(2022).
15. Rahman M, Shamsuzzaman M, Sarker M, Jobber A, Mia M, Bairagi AK, Ahmed M, Reza S, Malik SR, Bhuiyan MM, Khan AH. Dosimetric characterization of medical linear accelerator Photon and Electron beams for the treatment accuracy of cancer patients, W. J. Adv. Eng. Tech.Sci., **3**, 41-59 (2021).
16. Kutcher GJ, Coia L, Gillin M, Hanson WF, Leibel S, Morton RJ, Palta JR, Purdy JA, Reinstein LE, Svensson GK, Weller M. Comprehensive QA for radiation oncology: report of AAPM radiation therapy committee task group 40., **21**, 581-618 (1994).
17. Mayles P, Nahum A, Rosenwald JC. Handbook of radiotherapy physics: theory and practice. CRC Press; (2007).

18. Yani S, Dirgayussa IG, Rhani MF, Soh RC, Haryanto F, Arif I. Monte Carlo study on electron contamination and output factors of small field dosimetry in 6 MV photon beam, Smart Sci., **4**, 87-94 (2016).

19. Dowlatabadi H, Mowlavi AA, Ghorbani M, Mohammadi S, Knaup C. Study of photoneutron production for the 18 mv photon beam of the siemens medical linac by monte carlosimulation, J. Biomed. Phys. Eng., **10** 679-690 (2020).

20. Dawn, S, Pal R, Bakshi, AK, Kinhikar RA, Joshi K, Jamema SV, Haneefa A, Selvam TP, Deshpande, DD and Datta D, Evaluation of in-field neutron production for medical LINACs with and without flattening filter for various beam parameters-Experiment and Monte Carlo simulation. Radiat. Meas., **118**, 98-107 (2018).

21. Nath R, Epp ER, Laughlin JS, Swanson WP, Bond VP. "Neutrons from high-energy x-ray medical accelerators: an estimate of risk to the radiotherapy patient." J. Medi. Phys, **11(3)**: 231-241. (1984)

22. British Institute of Radiology. Central Axis Depth Dose Data for Use in Radiotherapy. The British Journal of Radiology-25. (1996.)

23. Kutcher GJ, Coia L, Gillin M, Hanson WF, Leibel S, Morton RJ, Palta JR, Purdy JA, Reinstein LE, Svensson GK, Weller M. Comprehensive QA for radiation oncology: report of AAPM radiation therapy committee task group 40, **21**, 581-618 (1994)

Atherosclerotic Risk Profiling via Carotid Intima-Media Thickness: Comparative Insights from Radioiodine-Treated Thyroid Carcinoma and Hyperthyroidism

A. Naznin[1], F. Akter[2], M.R. Majumder[2], F. Yasmin[2], S. Sharmin[3], H.A. Rahman[4] and Z. Jabin[5]

[1.]*Senior Medical Officer, Institute of Nuclear Medicine and Allied Sciences (INMAS), Suhrawardy.*
[2.]*Senior Medical Officer,* [3.]*Principal Medical Officer*
[4]*Director & Chief Medical Officer, Institute of Nuclear Medicine and Allied Sciences (INMAS), Mitford, Dhaka.*
[5.]*Director & Chief Medical Officer, Institute of Nuclear Medicine and Allied Sciences (INMAS), Suhrawardy, Dhaka.*

Abstract

Therapeutic radiation exposure is an important component of management in different thyroid disorders. Head and neck irradiation is a known risk factor for carotid artery atherosclerosis. This study is therefore, designed to evaluate carotid intima medial thickness (CIMT) of radioiodine treated thyroid carcinoma and hyperthyroidism patients, as a means of predicting cardiovascular risk. The study was conducted at the Institute of Nuclear Medicine & Allied Sciences (INMAS), Mitford, Dhaka from July 2024 to January 2025. Three categories of patients were selected. First group included patients with history of receiving radioiodine therapy after total thyroidectomy for differentiated thyroid carcinoma (DTC). Second group comprised of patients treated with radioiodine due to hyperthyroidism, and the third was age matched control group with no known thyroid disorder. Relevant biochemical parameters including thyroid hormone profile were documented, and ultrasound of neck region was done taking note of mean carotid IMT and presence of any plaque. Study subjects were 80 in number, subdivided into thyroid carcinoma (30), hyperthyroidism (30) and control (20) groups. CIMT was significantly higher in hyperthyroidism group ($p = 0.001$). There was also significantly more incidence of carotid plaque formation ($p = 0.000$). But interestingly, there was no statistically significant increase of CIMT or plaque formation in thyroid carcinoma patients compared to control group ($p = 0.695$). This study emphasizes the importance of vascular risk stratification in radioiodine treated hyperthyroidism patients. It is also observed that post therapy DTC patients are not subject to accelerated or abnormal atherosclerosis as evidenced by their CIMT.

Keywords: Carotid Intima Medial Thickness, Radioiodine therapy, Thyroid carcinoma, Thyrotoxicosis.

Introduction

Vascular damage secondary to therapeutic radiation exposure is a known phenomenon [1-3]. Head and neck irradiation for any malignancy has been reported to cause acute thrombosis, vessel rupture, wall thickening and rapidly advancing atherosclerosis of carotid arteries leading to significant extracranial stenosis [4, 5]. Nuclear medicine therapies, unlike conventional radiotherapy, delivers a safer, tissue specific radiation exposure through recognized treatment protocols. The most familiar of all nuclear medicine treatment options is perhaps the radioiodine therapy. Administration of radioiodine is not only a cornerstone in the management of differentiated thyroid carcinoma (DTC), but also a well-established therapeutic choice for hyperthyroidism [6]. Beta radiation from Iodine-131 penetrates the tissue resulting in cell death. However, this beta radiation may also raise concern regarding potential risk of metabolic and vascular damage to adjacent carotid vessels.

The carotid intima-media thickness (IMT) is a frequently used biomarker for assessing atherosclerosis. Moreover, it can be easily and noninvasively measured through B-mode ultrasound [7, 8]. There are multiple studies in the literature utilizing CIMT to predict global atherosclerotic change in various systemic diseases, but the findings are variable in thyroid disorders [9-12]. The objective of this study was therefore, to assess carotid intima-media thickness and detect the presence of carotid plaque in radioiodine treated thyroid cancer and hyperthyroidism patients by neck ultrasound, and to compare these vascular parameters with those observed in age- and sex-matched controls.

*Corresponding author: afroza.naznin@yahoo.com

Patients and Methods

This observational study was conducted at the Institute of Nuclear Medicine & Allied Sciences (INMAS), Mitford, Dhaka from July 2024 to January 2025. Three categories of patients were selected from the regular patient pool of the institute. First group included patients with history of receiving radioiodine therapy after total thyroidectomy for differentiated thyroid carcinoma. Second group comprised of patients treated with radioiodine due to hyperthyroidism, and the third was age matched control group with no known thyroid disorder. Patients with atherosclerotic risk factors like obesity, smoking habit and co-morbidities e.g. diabetes, hypertension and dyslipidemia were excluded. Besides, patients of first and second groups had history of single radioiodine therapy, and were in follow-up for at least one year. Proper history was taken with documentation of relevant biochemical parameters including latest thyroid hormone profile to ensure that the patients are either biochemically euthyroid or within the recommended serum TSH range at the time of study.

After explaining the procedure and taking verbal consent, ultrasound of neck region was done taking note of mean carotid IMT and presence of any plaque. Linear array transducer of 2-14 MHz frequency was used from a Samsung V8 ultrasound system. Carotid IMT was measured on the far wall of common carotid artery, 10 mm proximal to the bifurcation and in a plaque free region. The distance

between two parallel echogenic lines (lumen-intima and media-adventitia interfaces) were registered, three times on each side and the average was calculated (Figure 1).

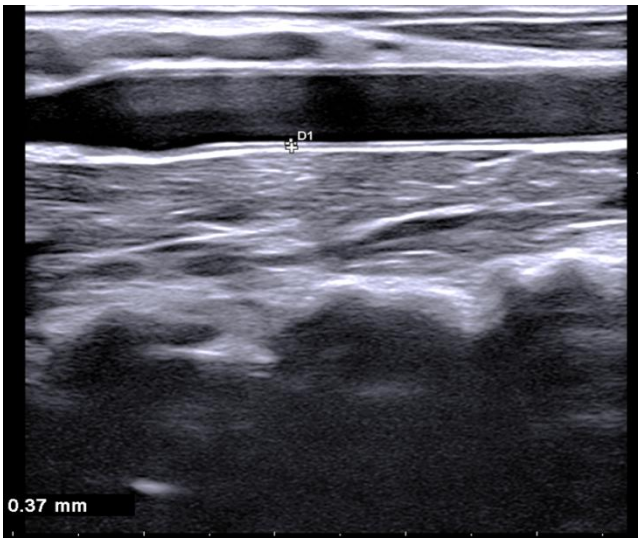

Fig. 1: Representative sonographic image of CIMT measurement. Distance between two echogenic lines is measured in a plaque free region, about 10 mm proximal to the bifurcation.

Plaques were defined as lesions arising from arterial wall measuring ≥ 1.5 mm in length, impinging into the lumen by minimum 0.5 mm or half of the adjacent IMT value [13]. The findings were recorded in tabulated datasheets. Finally statistical tests were done using Microsoft Excel and SPSS. Independent samples test and chi square test were done to assess statistical significance.

Result

Study subjects were 80 in number, subdivided into thyroid carcinoma [30], hyperthyroidism [30] and control [20] groups. Their age ranged between 19 – 80 years (mean ± SD 40.5 ± 13.4 years) with female preponderance (86.3%). Table 1 shows group wise age and gender distribution with no statistically significant difference with the controls.

Table 1: Age and gender distribution of Ca thyroid, hyperthyroidism & control groups

Groups	Mean age ± SD (years)		Gender		
			Female	Male	
Ca thyroid	35.9 ± 7.7	p > 0.2	27	3	p > 0.4
Hyperthyroidism	45.4 ± 12.4		24	6	
Control	40.0 ± 18.5		18	2	

The sample population showed increasing CIMT with age irrespective of group (Figure 2). However, in group wise comparison, the hyperthyroidism group revealed significantly higher CIMT as well as incidence of carotid plaque formation. But interestingly, there was no statistically significant increase of CIMT or plaque formation in thyroid carcinoma patients compared to control group (Table 2).

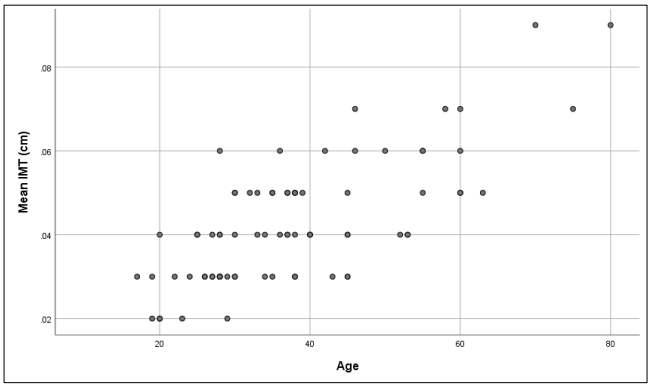

Fig. 2: Scatter diagram showing good positive correlation of age with mean carotid IMT (Pearson correlation coefficient 0.738).

Table 2: Groupwise mean CIMT and presence of carotid plaque

Groups	Mean CIMT (mm)± SD	Plaque	No plaque	
Control	0.43 ±0.18 (p = 0.695)	2	18	
Hyperthyroidism	0.65 ±0.22 (p = 0.001)	13	17	p = 0.000
Ca thyroid	0.45±0.10	1	29	

Discussion

Atherosclerosis is a progressive pathological condition, characterized by chronic inflammatory process leading to accumulation of lipids [14]. It is the commonest cause of coronary and carotid artery disease. Nowadays, imaging modalities like carotid ultrasound has been popular as an easy mean to assess CIMT and presence of plaque for cardiovascular risk prediction [15]. Few studies have explored this option for systemic disease patients having higher atherosclerotic risk, e.g. chronic kidney disease patients subjected to hemodialysis, ankylosing spondylitis etc. [9, 10]. Various authors have also evaluated carotid wall thickness in thyroid disorder patients. A German study involving more than 2000 participants observed a positive linear relationship between thyroid hormone level and the CIMT [16]. On the other hand, no association could be detected between subclinical thyroid disorders and CIMT or atherosclerotic plaque [17]. However, the study population of the aforementioned works were not selected based on history of radioiodine therapy.

Endothelial cells of blood vessels are susceptible to radiation in multiple ways. Chronic effects can manifest over the course of months to years; and exert detrimental changes in coronary, pulmonary, hepatic, and peripheral arteries, as well as cerebral vasculature [1]. This is why study subjects of case groups in the present study were selected with an interval of at least one year after

radioiodine administration. But irrespective of treatment history, the sample population showed a positive linear relationship between increasing age and carotid IMT (Figure 1), which concurs with multiple previous study findings [8, 18-20].

There is scarcity of literature featuring comparative assessment of CIMT and atherosclerotic plaque between different types of radioiodine treated patients. A 2008 study evaluated 106 DTC patients for metabolic and cardiovascular risks, and found no significant difference with the controls [21]. This is similar to the present work (Table 2). Another group of authors measured CIMT of 36 patients who underwent radioiodine administration for nodular goitre and Grave's disease [6]. They documented consistent significant increase of CIMT only in nodular goitre patients. The current study observed overall higher mean CIMT in the patients of hyperthyroidism group, but did not categorize the finding according to underlying pathology e.g. Grave's disease or toxic nodular goitre (Table 2). Besides, the aforementioned study followed up the subjects up to 12 months post therapy; whereas the present study participants had radioiodine therapy more than one year ago. This inclusion criterion was set based on the observation that patients subjected to conventional head-neck radiotherapy usually shows significant increase of IMT after a long post-treatment interval, even 5-10 years [b22, 23].

There are multiple limitations of the current study. First, it was not optimally designed as a prospective study would have been better for risk assessment. Second, the sample size was too small to reach any definite consensus. Third, other metabolic and cardiovascular parameters for atherosclerotic risk profiling could not be evaluated. A large prospective multicentric project might be planned to mitigate these drawbacks.

Conclusion

This study observes higher CIMT in radioiodine treated hyperthyroidism patients, emphasizing the importance of vascular risk stratification in this group. It is also noted that despite relatively large radionuclide dosage, post therapy DTC patients are not subject to accelerated or abnormal atherosclerosis as evidenced by their CIMT. This once again highlights the relative safety of nuclear medicine therapies in comparison to conventional irradiation.

References

1. Venkatesulu BP, Mahadevan LS, Aliru ML, Yang X, Bodd MH, Singh PK, Yusuf SW, Abe JI, Krishnan S. Radiation-induced endothelial vascular injury: a review of possible mechanisms. JACC: Basic to Translational Science. 2018 Aug;3(4):563-72.
2. Kameni LE, Januszyk M, Berry CE, Downer Jr MA, Parker JB, Morgan AG, Valencia C, Griffin M, Li DJ, Liang NE, Momeni A. A review of radiation-induced vascular injury and clinical impact. Annals of Plastic Surgery. 2024 Feb 1;92(2):181-5.
3. Venkatesulu BP, Sanders KL, Hsieh CE, Kim BK, Krishnan S. Biomarkers of radiation- induced vascular injury. Cancer Reports. 2019 Apr;2(2):e1152.
4. Fernández-Alvarez V, López F, Suárez C, Strojan P, Eisbruch A, Silver CE, Mendenhall WM, Langendijk JA, Rinaldo A, Lee AW, Beitler JJ. Radiation-induced carotid artery lesions. Strahlentherapie und onkologie. 2018 Aug;194(8):699-710.
5. Gujral DM, Chahal N, Senior R, Harrington KJ, Nutting CM. Radiation-induced carotid artery atherosclerosis. Radiotherapy and Oncology. 2014 Jan 1;110(1):31-8.
6. Sürücü E, Bekiş R, Şengöz T, Demir Y, Çelik AO, Orbay Ö, Birlik B, Ozdoğan Ö, İğci E, Durak H. The effect of radioiodine on the intima media thickness of the carotid artery. Molecular imaging and radionuclide therapy. 2013 Dec 10;22(3):85.
7. Simon A, Megnien JL, Chironi G. The value of carotid intima-media thickness for predicting cardiovascular risk. Arteriosclerosis, thrombosis, and vascular biology. 2010 Feb 1;30(2):182-5.
8. Nezu T, Hosomi N, Aoki S, Matsumoto M. Carotid intima-media thickness for atherosclerosis. Journal of atherosclerosis and thrombosis. 2016 Jan 6;23(1):18-31.
9. Gupta N, Saigal R, Goyal L, Agrawal A, Bhargava R, Agrawal A. Carotid intima media thickness as a marker of atherosclerosis in ankylosing spondylitis. International Journal of Rheumatology. 2014;2014(1):839135.
10. Abbasi MR, Abbaszadeh SH, Rokni-Yazdi H, Lessan-Pezeshki M, Khatami MR, Mahdavi-Mazdeh M, Ahmadi F, Seifi S, Gatmiri SM. Carotid intima-media thickness as a marker of atherosclerosis in hemodialysis patients. Indian Journal of Nephrology. 2016 Mar 1;26(2):97-101.
11. Şanal B, Işık İ, Korkmaz M, Kucur C, Can F, Kilit TP, Kahraman C, Kaçar E, Koçak A. Effect of radioactive iodine therapy on carotid intima media thickness in patients with hyperthyroidism. Annals of nuclear medicine. 2016 Jan;30(1):75-80.
12. La Cour JL, Andersen UB, Sørensen CH, Nygaard B, Jensen LT. Radioiodine therapy does not change the atherosclerotic burden of the carotid arteries. Thyroid. 2016 Jul 1;26(7):965-71.
13. Park TH. Evaluation of carotid plaque using ultrasound imaging. Journal of Cardiovascular Ultrasound. 2016 Jun 22;24(2):91.
14. Vaya J. The association between biomarkers in the blood and carotid plaque composition-focusing on oxidized lipids, oxysterols and plaque status. Biochemical pharmacology. 2013 Jul 1;86(1):15-8.
15. del Sol AI, Moons KG, Hollander M, Hofman A, Koudstaal PJ, Grobbee DE, Breteler MM, Witteman JC, Bots ML. Is carotid intima-media thickness useful in cardiovascular disease risk assessment? The Rotterdam Study. Stroke. 2001 Jul;32(7):1532-8.
16. Vo□lzke H, Robinson DM, Schminke U, Lu□demann J, Rettig R, B. Felix S, Kessler C, John U, Meng W. Thyroid function and carotid wall thickness. The Journal of Clinical Endocrinology & Metabolism. 2004 May 1;89(5):2145-9.

17. Delitala AP, Filigheddu F, Orrù M, AlGhatrif M, Steri M, Pilia MG, Scuteri A, Lobina M, Piras MG, Delitala G, Lakatta EG. No evidence of association between subclinical thyroid disorders and common carotid intima medial thickness or atherosclerotic plaque. Nutrition, Metabolism and Cardiovascular Diseases. 2015 Dec 1;25(12):1104-10.

18. Davis PH, Dawson JD, Riley WA, Lauer RM. Carotid intimal-medial thickness is related to cardiovascular risk factors measured from childhood through middle age: The Muscatine Study. Circulation. 2001 Dec 4;104(23):2815-9.

19. van den Munckhof IC, Jones H, Hopman MT, de Graaf J, Nyakayiru J, van Dijk B, Eijsvogels TM, Thijssen DH. Relation between age and carotid artery intima- medial thickness: a systematic review. Clinical cardiology. 2018 May;41(5):698-704.

20. Paul J, Shaw K, Dasgupta S, Ghosh MK. Measurement of intima media thickness of carotid artery by B-mode ultrasound in healthy people of India and Bangladesh, and relation of age and sex with carotid artery intima media thickness: An observational study. Journal of cardiovascular disease research. 2012 Apr 1;3(2):128-31.

21. Giusti M, Mortara L, Degrandi R, Cecoli F, Mussap M, Rodriguez G, Ferone D, Minuto F. Metabolic and cardiovascular risk in patients with a history of differentiated thyroid carcinoma: A case-controlled cohort study. Thyroid research. 2008 Sep 29;1(1):2.

22. Dorresteijn LD, Kappelle AC, Scholz NM, Munneke M, Scholma JT, Balm AJ, Bartelink H, Boogerd W. Increased carotid wall thickening after radiotherapy on the neck. European journal of cancer. 2005 May 1;41(7):1026-30.

23. Muzaffar K, Collins SL, Labropoulos N, Baker WH. A prospective study of the effects of irradiation on the carotid artery. The Laryngoscope. 2000 Nov;110(11):1811-4.

Comprehensive Profiling of Trace/Toxic Elements in Raw Cow's Milk commonly available in different areas of Bangladesh: Occurrence, Distribution and Health Risk Assessment

E. Akter[1], SK. Kalimullah[1], S. Akter[2]*, Y.N. Jolly[2], J. Kabir[2], S. Hossain[2], K.M. Mamun[2], M.J. Abedin[3] and M.A. Rouf[1]

[1.]*Gono Bishwabidyalay*

[2.]*Atmospheric and Environmental Chemistry Laboratory (AECL), Chemistry Division, Atomic Energy Centre, Dhaka (AECD)*

[3.]*Accelerator Facilities Division, Atomic Energy Centre, Dhaka (AECD)*

Abstract

The cow's milk offers essential nutrients that support bone strength, metabolic functions, and overall health in both children and adults. However, contamination with heavy metals poses potential health risks. This study investigated the concentrations of 14 metals (Ca, Cr, Mn, Fe, Co, Ni, Cu, Zn, As, Se, Rb, Sr, Hg, Pb) in cow's milk collected from 15 districts of Bangladesh using Energy Dispersive X-ray Fluorescence (EDXRF) at the Atomic Energy Centre, Dhaka. Analysis of 30 raw cow'smilk samples revealed that Ca, Fe, Zn, Se, Sr, and Hg were present in most samples, while Cr, Mn, Co, Ni, Cu, As, and Rb were detected at trace levels. Concentrations varied by location, reflecting geological and environmental differences. Daily Intake Metals(DIM),Health Risk Index (HRI) and Hazard Index (HI) were calculated, with HRI values below 1.0, indicating negligible non-carcinogenic risk, in line with WHO/US EPA guidelines that recommend HRI (or THQ) values below 1 to indicate acceptable risk. These findings provide baseline data for monitoring milk safety and ensuring public health.

Keywords: Milk, Heavy metals, Energy Dispersive X-ray Fluorescence (EDXRF), Health risk assessment, Trace elements, Calcium, Food safety.

1 Introduction

Milk is recognized worldwide as a complete food for both children and adult due to its well-balanced nutrient composition [1]. It is particularly important for infant, children, and pregnant women for providing key nutrients (carbohydrate, protein, fat, minerals etc.) to develop bone and physical growth. Certain trace elements Calcium (Ca), Iron (Fe), Manganese (Mn), Copper (Cu), Zinc (Zn), Cobalt (Co), and Selenium (Se) are essential for metabolic and enzymatic functions. However, excessive intake can lead to toxic effects. Moreover, presence of some non-essential elements such as lead (Pb), Mercury (Hg), Arsenic (As), And Chromium (Cr) is toxic even at low concentration and have no biological role [2].Despite several essential nutrients, Bioactive compound, enzymes presence, milk can be a path way to transfer environmental contaminants including trace and toxic metals from environment to human body [3]. Bioactive compounds and enzymes are present in milk, but it can also act as a pathway for transferring environmental contaminants, including toxic metals, to humans.

In developing countries like Bangladesh, where milk consumption is increasing steadily, contamination by toxic elements has become a major public health concern. Several studies have reported elevated concentrations of heavy metals in raw milk due to environmental pollution, contaminated feed, poor water quality, and unhygienic handling during collection and distribution [4]. Regional variations in contamination levels often reflect differences in agricultural practices, industrial activities, and environmental management systems across the country. For instance, areas near industrial zones and highways tend to show higher contamination levels due to vehicular emissions and industrial effluents [5].

Despite the growing awareness of food safety, comprehensive data on toxic element concentrations in raw milk from various regions of Bangladesh remain limited. Understanding these contamination patterns is crucial for evaluating public exposure and ensuring compliance with international safety standards, such as those established by the World Health Organization (WHO) and the Codex Alimentarius [6]. Furthermore, identifying the potential sources of contamination can aid in formulating preventive strategies to minimize heavy metal accumulation in milk and other dairy products.

Therefore, the present study aims to analyze the concentration and distribution of toxic elements in raw milk samples collected from different regions of Bangladesh. The findings are expected to contribute to a better understanding of the safety status of milk in the country and provide evidence-based recommendations for policymakers, producers, and consumers to ensure safer dairy practices and protect public health

2 Materials and methods

2.1 Study area and sample collection

A total of 30 raw cow milk samples were collected from 15 districts representing diverse geographical and agricultural regions of Bangladesh Figure 1. The cow milk samples were identified into two categories: Domestic Milk (DM) and Commercial/Farm Milk (FM**)**. From each district, one

*Corresponding author: shirinakhter43@yahoo.com

sample was obtained from a dairy farm and another from a domestic source within the same locality, ensuring comparable environmental and management conditions Table 1. Each sample, approximately 250 mL in volume, was collected in pre-cleaned plastic bottles to prevent external contamination [7]. All samples were immediately stored in ice boxes at 4°C and transported to the laboratory for analysis. All milk samples were oven-dried at approximately 70°C overnight and further heated until a constant weight was obtained. The dried samples were then finely ground using a carbide mortar and pestle, transferred to labeled plastic vials, and stored in desiccators until irradiation [8].

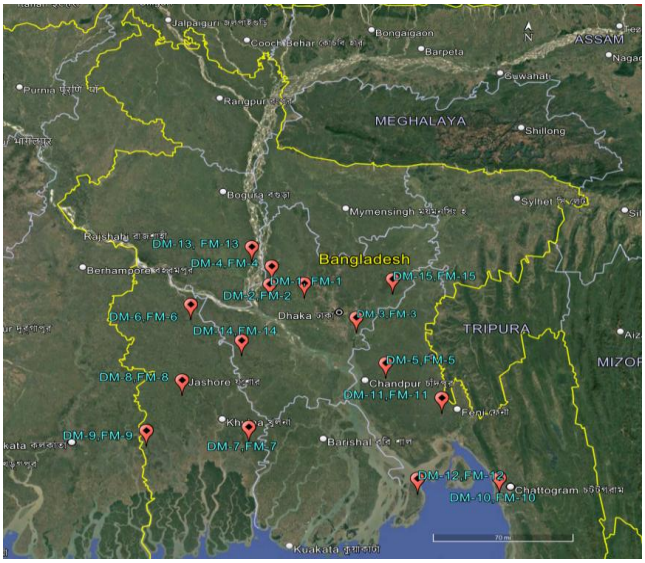

Fig. 1: Sampling Location of all domestic and commercial Cow's milk samples collected from various regions of Bangladesh.

Table 1: Identification of all domestic and commercial Cow's milk samples

LAB ID	Farm Type	Sample ID	Sampling Location	Sample Type
5651 Milk	Domestic Milk (DM)	DM-1	Manikganj	Liquid
5652 Milk	Commercial/ Firm Milk (FM)	FM-1		
5653 Milk	Domestic Milk (DM)	DM-2	Dhaka	Liquid
5654 Milk	Commercial/ Firm Milk (FM)	FM-2		
5655 Milk	Domestic Milk (DM)	DM-3	Narayanganj	Liquid
5656 Milk	Commercial/ Firm Milk (FM)	FM-3		
5657 Milk	Domestic Milk (DM)	DM-4	Tangail	Liquid
5658 Milk	Commercial/ Firm Milk (FM)	FM-4		
5659 Milk	Domestic Milk (DM)	DM-5	Chandpur	Liquid
5660 Milk	Commercial/ Firm Milk (FM)	FM-5		
5661 Milk	Domestic Milk (DM)	DM-6	Jhenaidah	Liquid
5662 Milk	Commercial/ Firm Milk (FM)	FM-6		
5786 Milk	Domestic Milk (DM)	DM-7	Khulna	Liquid
5787 Milk	Commercial/ Firm Milk (FM)	FM-7		
5788 Milk	Domestic Milk (DM)	DM-8	Jessore	Liquid
5789 Milk	Commercial/ Firm Milk (FM)	FM-8		
5790 Milk	Domestic Milk (DM)	DM-9	Satkhira	Liquid
5791 Milk	Commercial/ Firm Milk (FM)	FM-9		
5792 Milk	Domestic Milk (DM)	DM-10	Chittagong	Liquid
5793 Milk	Commercial/ Firm Milk (FM)	FM-10		
5794 Milk	Domestic Milk (DM)	DM-11	Feni	Liquid
5795 Milk	Commercial/ Firm Milk (FM)	FM-11		
5796Milk	Domestic Milk (DM)	DM-12	Noakhali	Liquid
5797 Milk	Commercial/ Firm Milk (FM)	FM-12		
5798 Milk	Domestic Milk (DM)	DM-13	Sirajganj	Liquid
5799 Milk	Commercial/ Firm Milk (FM)	FM-13		
5800 Milk	Domestic Milk (DM)	DM-14	Faridpur	Liquid
5801 Milk	Commercial/ Firm Milk (FM)	FM-14		
5802 Milk	Domestic Milk (DM)	DM-15	Narsingdi	Liquid
5803 Milk	Commercial/ Firm Milk (FM)	FM-15		

* DM= Domestic Milk, FM= Firm Milk

2.2 Sample preparation

2.2.1 Drying, heating and Grinding

All liquid milk samples, each with a particular identification number were first dried in water bath at 100 ºC temperature. Leave the sample for 8 days in water bath. A small amount of acetone mixed with the dried sample and wash out the oil part. To remove residual fat, the dried samples were defatted using analytical-grade acetone, followed by solvent evaporation and redrying at 70 °C. Then the sample leave on the water bath for the evaporation of excess acetone from the sample and finally in an oven at around 70ºC for overnight until a constant weight were obtained [9]. Samples were evaporated using a controlled hot plate/water bath at approximately 95 °C to remove moisture, followed by oven drying at 70 °C to constant weight. After heating in the oven, the samples need to be grinded. It takes 10 to 15 minutes to have fine grain size. For several reasons, grinding is required for sample preparation for Energy Dispersive X-ray Fluorescence (EDXRF) analysis.

2.2.2 Weighting and Pelleting

Pelleting is a sample preparation technique used in Energy Dispersive X-ray Fluorescence (EDXRF) to prepare solid samples for analysis. The sample is compressed into a pellet, which is then analyzed by the EDXRF instrument. For each milk sample, 0.1 gm of material was pressed into a 7 mm diameter pellet using a SPECAC hydraulic pellet maker, applying a pressure of 3 tons.A pressure of 3 tons was applied during pellet formation.The pellet is then analyzed using the EDXRF instrument.[10] Pelleting is frequently used for solid samples, such as powders or loose granules, that are difficult to analyze using other sample preparation methods. The technique produces a more uniform sample matrix, which can improve the analysis's accuracy and precision. Pelleting can also mitigate the effects of surface roughness or porosity, which can affect the intensity of the sample's X-ray fluorescence 3 tons of pressure need to give to milk sample.

2.2.3 Instrumentation

In the laboratory, heavy metal analysis was performed using Energy Dispersive X-ray Fluorescence (EDXRF) spectroscopy (Model: ARL QUANT'X EDXRF Analyzer, Thermo Scientific, Switzerland) equipped with a 1 mm collimator and operated through WinTrace software. Excitation settings were controlled using Thermo Scientific WinTrace™ software. The X-ray tube voltage was set between 20–50 kV, and the measurement time was fixed at 300 s per sample to ensure reliable elemental analysis [11].

2.3 Construction of Calibration Curve for Method Validation

Elemental concentrations were determined using the EDXRF technique, following the direct comparison approach described by Islam and Jolly (2007) [12]. In this method, calibration curves are constructed using standards that share a similar matrix with the samples, ensuring comparable sensitivity and minimizing matrix effects. To establish the calibration curves, three laboratory-prepared cellulose-based multi-element standards (Cellu-1, Cellu-2, and Cellu-3) were utilized [13]. These standards were selected based on the sensitivity of K- and L-series X-ray lines as a function of atomic number for accurate elemental analysis in milk samples. The accuracy of the constructed calibration curves was verified by analyzing a groundwater sample and confirming its results under the same calibration conditions Table 2.

Table 2: Accuracy and precision of the analytical technique (Cellu -2)

Elements	Elemental Concentrations (mg/kg)				
	Concentrations1	Concentrations 2	Mean	Stdev	LOD
Cr	4.490	4.520	4.505	0.021	0.064
Ni	1.250	1.230	1.240	0.014	0.042
Cu	19.970	20.350	20.160	0.269	0.806
As	0.120	0.115	0.118	0.004	0.011
Cd	9.350	9.220	9.285	0.092	0.276
Pb	3.220	3.190	3.205	0.021	0.064

*LOD= Limit of Detection, Stdev=Standard Deviation

2.3 Calculation of Health Risk Index (HRI)

Health Risk Index (HRI) is calculated on the basis of Daily Intakeof Metals (DIM). The daily intake of metals is determined by both the content of metals in food and the amount of food consumed. Furthermore, human body weight has been shown to influence contaminant tolerance [14]. The following equation Cui et al. was used to calculate the daily intake of metals (DIM) of the selected heavy metals in analyzed milk [15].

DIM (mg/kg-BW/day) = (C metal × D food intake) /B average weight…… (1)

Where: C (mg/kg) denotes concentration of heavy metal in the milk, D food intake denotes the average daily intake (mg/person/day) and Bis average body weight of an adult 70 kg and for Child 30 kg. Through food (milk) consumed and oral reference dose (Rf_D) suggested [16]. Rf_D is estimated as per day exposure of metal to human body that has no hazardous effect during life time. Oral reference dose for Cr, Ni, Cu, Pb, Cd, Mn and Zn were 1.5, 0.02, 0.04, 0.004, 0.001, 0.033 and 0.30 (mg/kg body weight/day) respectively; 10-60 (mg/kg body weight/day) for Fe[17]; 0.002 (mg/kg body weight/day) for Hg. The US EPA reference dose (RfD) for inorganic arsenic is 0.0003 mg/kg/day.The reference dose (Rf_D) for inorganic arsenic is 0.0003 (mg/kg body weight/day) base on hyper pigmentation, keratosis and possible vascular complications in human. Health Risk Index (HRI) for Cr, Ni, Cu, Pb, Cd, As, Hg, Mn, Zn and Fe by consumption of milk was calculated by following which is expressed by the equation

$$HRI = DIM/Rf_D \quad \text{----------} \quad (2)$$

According to Food and Nutritional Board (2004), an index more than 1 is consideredunsafe for human health.

Table 3: Concentration of heavy metals in different types of Domestically produced milksamples.

Elements	Elemental concentrations (μg /ml) in different types of Domestically produced milk samples													
	Ca	Cr	Mn	Fe	Co	Ni	Cu	Zn	As	Se	Rb	Sr	Hg	Pb
DM-1	0.128	<0.0001	<0.002	0.004	<0.0001	0.004	<0.001	0.002	<0.0003	0.004	0.003	0.001	0.003	0.002
DM-2	0.106	0.001	0.002	0.003	<0.0001	<0.0002	0.002	0.002	<0.0003	0.002	0.002	0.001	<0.0004	<0.0003
DM-3	0.158	<0.0001	<0.002	0.004	0.002	<0.0002	<0.001	0.003	<0.0003	0.003	0.002	0.001	0.001	<0.0003
DM-4	0.127	<0.0001	0.003	0.003	0.001	<0.0002	<0.001	0.003	0.002	0.004	0.002	0.001	<0.0004	<0.0003
DM-5	0.143	<0.0001	<0.002	0.009	<0.0001	0.002	<0.001	0.002	0.001	0.003	0.004	0.002	<0.0004	<0.0003
DM-6	0.137	0.001	<0.002	0.002	0.002	<0.0002	0.001	0.005	<0.0003	0.002	0.002	0.001	0.001	0.001
DM-7	0.124	<0.0001	<0.002	0.002	<0.0001	<0.0002	<0.001	0.003	<0.0003	0.001	0.001	0.001	<0.0004	0.001
DM-8	0.179	<0.0001	0.003	0.004	<0.0001	<0.0002	0.003	0.003	0.004	0.002	0.001	0.001	<0.0004	0.001
DM-9	0.163	0.001	0.003	0.002	0.002	0.003	<0.001	0.002	<0.0003	0.002	0.001	0.001	0.001	0.002
DM-10	0.102	<0.0001	<0.002	0.003	<0.0001	<0.0002	0.002	0.006	<0.0003	0.003	0.001	0.001	<0.0004	<0.0003
DM-11	0.09	<0.0001	<0.002	0.008	0.002	<0.0002	<0.001	0.002	0.003	0.003	0.002	0.001	<0.0004	<0.0003
DM-12	0.129	0.002	0.003	0.003	<0.0001	<0.0002	0.002	0.002	<0.0003	0.003	0.001	0.002	0.002	0.001
DM-13	0.113	<0.0001	0.004	0.002	0.002	0.002	<0.001	0.007	<0.0003	0.002	0.002	0.001	<0.0004	<0.0003
DM-14	0.124	<0.0001	<0.002	0.003	<0.0001	<0.0002	0.003	0.008	0.002	0.004	0.001	0.002	0.003	<0.0003
DM-15	0.172	0.001	<0.002	0.004	0.001	<0.0002	0.004	0.002	<0.0003	0.001	0.002	0.001	0.001	0.002
MIN	0.09	0.001	0.002	0.002	0.001	0.002	0.001	0.002	0.001	0.001	0.001	0.001	0.001	0.001
MAX	0.179	0.002	0.004	0.009	0.002	0.004	0.004	0.008	0.004	0.004	0.004	0.002	0.003	0.002
MEAN	0.1330	0.0012	0.0030	0.0037	0.0017	0.0028	0.0024	0.0035	0.0024	0.0026	0.0018	0.0012	0.0017	0.0014
STDEV	0.0260	0.0004	0.0006	0.0021	0.0005	0.0010	0.0010	0.0020	0.0011	0.0010	0.0009	0.0004	0.0010	0.0005
WHO	N/A	0.050	0.400	0.500	N/A	0.070	2.000	5.000	0.010	N/A	N/A	N/A	0.004	0.020
BDSW	N/A	0.050	0.100	0.030	0.050	0.100	1.000	N/A	0.050	N/A	N/A	N/A	0.001	0.050

*WHO- World Health Organization *BDSW-Bangladesh Standard of water Quality

Table 4: Concentration of heavy metals in different types of Commercially produced milk samples

Elements	Elemental concentrations (μg /ml) in different types of Commercially produced milk samples													
	Ca	Cr	Mn	Fe	Co	Ni	Cu	Zn	As	Se	Rb	Sr	Hg	Pb
FM-1	0.158	<0.0001	<0.002	0.003	<0.0001	<0.0002	<0.001	0.002	<0.0003	0.004	0.001	0.002	<0.0004	0.001
FM-2	0.179	<0.0001	0.002	0.002	<0.0001	<0.0002	<0.001	0.002	0.003	0.001	0.003	0.001	<0.0004	0.001
FM-3	0.128	0.001	<0.002	0.005	<0.0001	0.004	<0.001	0.002	<0.0003	0.001	0.003	0.001	0.003	0.001
FM-4	0.148	0.002	0.003	0.003	<0.0001	0.004	0.005	0.002	0.001	0.003	0.002	0.004	<0.0004	0.002
FM-5	0.131	<0.0001	<0.002	0.002	<0.0001	<0.0002	<0.001	0.003	<0.0003	0.001	0.002	0.001	0.001	0.001
FM-6	0.189	0.001	0.005	0.003	<0.0001	0.003	0.003	0.007	<0.0003	0.001	0.003	0.002	<0.0004	0.002
FM-7	0.156	<0.0001	0.002	0.002	0.001	0.002	<0.001	0.002	0.001	0.003	0.001	0.001	0.001	0.001
FM-8	0.097	0.001	<0.002	0.003	<0.0001	0.003	<0.001	0.003	<0.0003	0.001	0.001	0.001	<0.0004	0.002
FM-9	0.086	<0.0001	<0.002	0.002	0.001	<0.0002	0.001	0.002	0.002	0.002	0.001	0.001	<0.0004	<0.0003
FM-10	0.075	0.001	<0.002	0.002	0.001	<0.0002	0.001	0.006	<0.0003	0.001	0.001	0.001	0.001	0.002
FM-11	0.145	<0.0001	0.003	0.004	<0.0001	<0.0002	<0.001	0.002	0.001	0.002	0.001	0.001	<0.0004	<0.0003
FM-12	0.108	<0.0001	<0.002	0.003	<0.0001	<0.0002	<0.001	0.002	<0.0003	0.003	0.001	0.001	<0.0004	0.004
FM-13	0.115	<0.0001	<0.002	0.003	<0.0001	<0.0002	<0.001	0.006	0.001	0.003	0.002	0.001	0.002	0.002
FM-14	0.124	<0.0001	<0.002	0.003	<0.0001	0.003	0.003	0.002	<0.0003	0.001	0.003	0.002	<0.0004	<0.0003
FM-15	0.128	0.002	0.002	0.003	0.001	0.002	0.003	0.001	<0.0003	0.002	0.002	0.001	0.001	<0.0003
Min	0.075	0.001	0.002	0.002	0.001	0.002	0.001	0.001	0.001	0.001	0.001	0.001	0.001	0.001
Max	0.189	0.002	0.005	0.005	0.001	0.004	0.005	0.007	0.003	0.004	0.003	0.004	0.003	0.004
Mean	0.1311	0.0013	0.0028	0.0029	0.0010	0.0030	0.0027	0.0029	0.0015	0.0019	0.0018	0.0014	0.0015	0.0017
STDEV	0.0324	0.0005	0.0012	0.0008	0.0000	0.0008	0.0015	0.0018	0.0008	0.0010	0.0009	0.0008	0.0008	0.0009
WHO	N/A	0.050	0.400	N/A	N/A	0.070	2.000	N/A	0.010	0.055	N/A	N/A	0.004	0.010
BDSW	N/A	0.050	0.100	0.030	0.050	0.100	1.000	5.000	0.050	N/A	N/A	N/A	0.001	0.050

*WHO- World Health Organization *BDSW-Bangladesh Standard of water Quality,

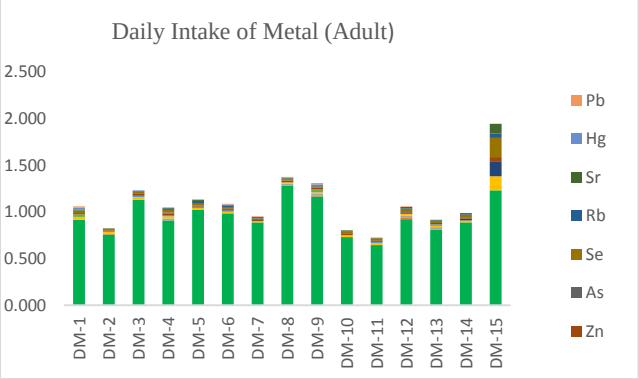

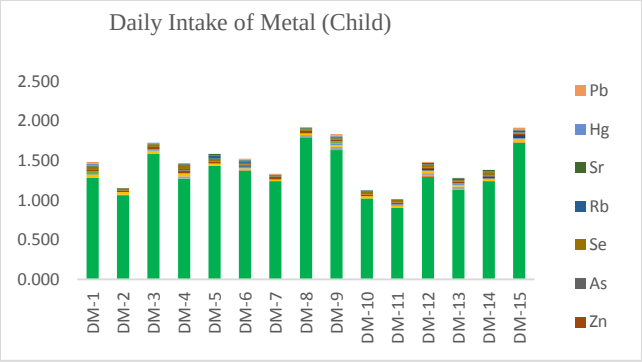

Fig. 2: Daily Intake of metals (Adult &Child) in different types of Domestically produced milk samples.

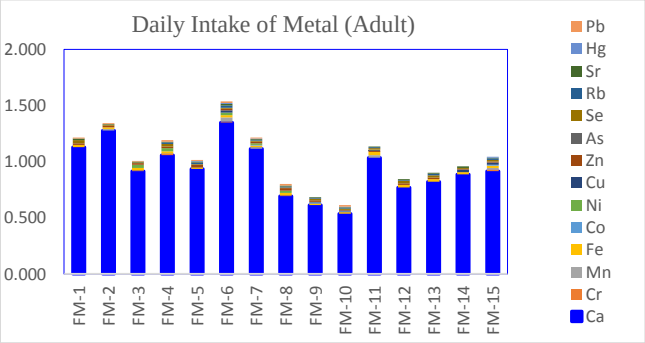

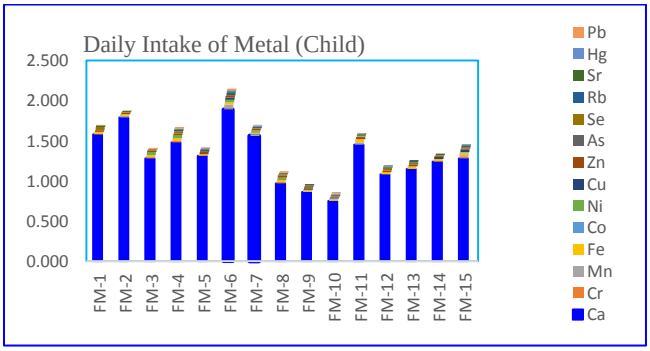

Fig. 3: Daily Intake of metals (Adult & Child) in different types of Commercially produced milk samples.

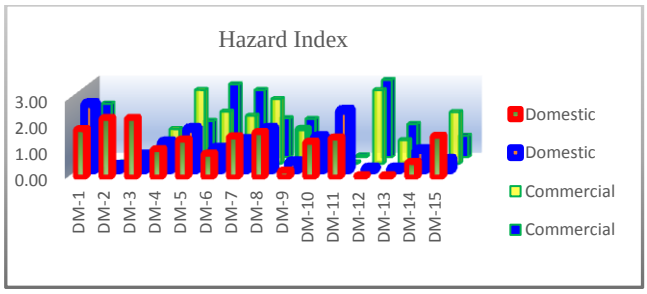

Fig. 4: Hazard Index (HI) for both adults and children in various types of domestically and commercially produced cow's milk samples.

3 Results and discussion

3.1 Elemental Concentrations in Cow's Milk Samples

Energy Dispersive X-ray Fluorescence (EDXRF) spectroscopy was used to quantify the elemental concentrations of calcium (Ca), chromium (Cr), manganese (Mn), iron (Fe), cobalt (Co), nickel (Ni), copper (Cu), zinc (Zn), arsenic (As), selenium (Se), rubidium (Rb), strontium (Sr), mercury (Hg), and lead (Pb) in thirty milk samples collected from fifteen districts of Bangladesh. Of these, fifteen samples represented domestically produced milk, and fifteen represented commercially produced milk.

The analysis revealed that Ca, Fe, Zn, Se, Sr, and Hg were present in the majority of the samples, whereas Cr, Mn, Co, Ni, Cu, As, Rb, and Pb were detected in only a few samples, often near or below their respective limit of detection (LOD) [18]. The LODs (mg kg^{-1}) were: Cr < 0.064, Ni <0.042, Cu < 0.81, As < 0.011, Cd< 0.28, and Pb < 0.064. These limit of detection confirm the high analytical sensitivity of the EDXRF method for multi-elemental quantification.

Chromium

Chromium plays vital role to maintain the metabolic systems of the human body; however, it can be poisonous at very low levels [19]. Cr is detected in 30% of the samples, ranging from 0.001-0.002 mg/L for both Domestic and Commercial milk. The level of Cr in milk is much lower than the permissible limit of 0.05 mg/L established by WHO. According to Muhib [20] the highest concentrations of Cr present in branded milk and dairy cow milk in Bangladesh were recorded at 0.672±0.010 mg/L and 0.373±0.008 mg/L respectively(BDSW) Table 3,4, which are higher than the result of the present study. The max daily intake level is calculated for Adult and Child 0.014 and 0.02 mg/ day for both domestic and commercial milk, which is lower or equal to the established adequate daily intake 0.02-0.03 mg/day [21].

Lead

Lead (Pb) is known to be very harmful and non-beneficial for human health. Lead can primarily affect human nervous and vascular systems [22]. Pb poisoning can lead to various adverse effects including lethargy, anemia, kidney and brain damage, as well as death [23]. unborn children can be affected through the mother as lead has ability to pass the placental barrier [24]. Excess amount of lead exposure has

the potential to be lethal [25]. In the present study, Pb is detected in 50% and 40% of commercial and domestic milk samples respectively which ranges 0.001-0.002 mg/L.Lead detection in 40–50% of samples is now clearly highlighted as concerning even if below limits.

Pb concentrations in milk collected from different places in Egypt which ranged from 1.850 mg/L to 4.404 mg/L reported by Malhat et al.[26]. These concentrations were higher than the concentrations reported in this study. Also, in previous in studies, Pb conc. in milk of farm and brought from store was relatively higher from current study. In Figure 2,3 the DIM for Pb ranged from 0.007 to 0.014 mg/L in the domestic and commercially sold milk both for adult and child.

The presence of arsenic represents a potential health hazard, especially for infants and young children who consume milk as a dietary main food. Previous studies have reported variable arsenic concentrations in milk depending on geographic location and environmental contamination levels [27]. However, arsenic was detected only in two samples of domestic and one in commercial milk ranges 0.001-0.002 mg/L. The concentration of the As is 10 times lower than the WHO permissible limit of 0.01 ppm [28]. In other study, Bangladesh Standard of water Quality (BDSW)showed As concentration in farm and store milk is around similar value of WHO permissible limit reported by Olowoyo et al.[29].The DIM (0.007–0.014 mg/day) both for adult and child was much less than the recommended RDA of 0.3 g/kg/day in the present study.

Mercury

Mercury (Hg) is considered as one of the most hazardous environmental contaminants, which is highly toxic heavy metal with no known biological function in humans. It can enter the food chain through industrial emissions, contaminated water, and agricultural inputs, eventually accumulating in animal tissues and milk. Organic form of mercury as methylmercury exposure can lead to severe health effects, including neurological, renal, and developmental disorders [30].

Mercury (Hg) levels in milk are generally low compared to other environmental components; however, even trace amounts can pose health risks due to mercury's high toxicity and bioaccumulative nature. Reported Hg concentrations in milk vary widely depending on environmental and industrial conditions, ranging from 0.001 mg/L to 0.05 mg/L in most studies Bangladesh Standard of water Quality (BDSW)[31]. According to international guidelines, the permissible limit of mercury in milk is typically around 0.02 mg/L as established by various food safety authorities. In total 10 Cow's milk samples, Hg was detected at relatively low concentration ranged from 0.001-0.003 mg/L for both domestic and commercial site which were below this permissible limit, indicating that the milk samples analyzed were within safe consumption levels. The Daily Intake of Metals (DIM) value of Hg in domestic samples ranged from 0.007-0.021 mg/day for adult and 0.010-0.030 mg/day for child.Similarly, the Daily Intake of Metals (DIM) value for Hg in commercial samples ranged from 0.001–0.007 mg/day for adults and 0.010–0.015 mg/day for children.

Iron, Zinc, Selenium, and Strontium

Iron (Fe), Zinc (Zn), Selenium (Se) and Strontium (Sr) are the essential elements in milk were detected in raw cow's milk in all geographic locations both from domestic and commercial samples in this study.

The concentration of Fe in the analyzed milk samples ranged from 0.002-0.004 in both domestic and commercial milk. The values of Fe in all the milk samples in the current study were lower than the values reported by Olowoyo et al.[29] which ranged from 0.04- 0.2 mg/L. The concentrations of the heavy metals in all milk samples were lower than the WHO recommended permissible limit of 0.5 mg/kg[32]. Daily intake of metal for Fe ranged from (0.02–0.04 mg/day) which is below the RDA of 8 mg/day [33].

Selenium (Se) is an essential trace element that usually plays a crucial role in human and animal health. It is a key component of several selenoproteins and enzymes, including glutathione peroxidase, which protect cells against oxidative damage and support immune and thyroid function. Sufficient amount of selenium intake is necessary for maintaining normal metabolism and antioxidant defense mechanisms [34]. The present study showed Se ranges from 0.001-0.004 mg/L in milk. Also, the DIM value ranges from 0.007 – 0.0204 mg/day for adult and child ranges 0.010-0.040 in domestic cow's milk showed lower value than RDA which is 0.055 mg/day according to the World Health Organization (WHO) and the U.S. National Academies of Sciences, Engineering, and Medicine (NASEM)[35].

Zn is also an essential element and detected in milk of all geographic locations. Zn ranged from 0.001 to 0.003 mg/L and DIM ranges from 0.0071- 0.03 mg/day in both domestic and Commercial milk. This value is much lower than the permissible limit established by WHO which is 5 mg/day.

Ca and Sr behave similarly and can substitute in bone mineral matrix, but concentration is subjected to variation depending on region, feed, soil Sr content, and possibly seasonal effect. In our study, Ca DIM ranges 0.643-1.279 mg/day for adult and child ranges 0.900-1.790 mg/day respectively [36]. At the same way, commercially produced cows' milk for adult 0.536-1.350 mg/day and child ranges from 0.750-1.890 mg/day for this both daily intake consume.

Sr concentration ranged 0.001-0.002 mg/L in milk and DIM value is 0.007- 0.102for adult and child ranges 0.010-0.020 for both milks. This value is also low in reported value in the other studies [37]. There is no link between regional and geographical distribution of metal content in milk samples.

3.2 Comparison Between Domestic and Commercial Cow's Milk

A comparative assessment between domestic and commercial cow's milk indicated that the Ca concentration was higher in commercially produced milk than in domestically produced milk. This variation may be

attributed to the use of mineral fortified feed, supplementary diets, or differences in processing methods in commercial dairy farms. Meanwhile, other macro and microelements [38] such as Fe, Zn, and Se showed similar trends in both groups, suggesting that environmental and feed-related influences are more significant than processing differences for these elements.

3.3 Spatial Distribution of Elements

The elemental distribution was non-uniform across the studied districts, reflecting the diverse geological and environmental characteristics of the sampling areas. Regional variations in soil mineralogy, groundwater composition, and forage type likely contribute to this heterogeneity [39]. Such findings are consistent with the geochemical dependence of milk composition reported in similar environmental monitoring studies.

The irregularity in trace-element concentration emphasizes the need for region-specific monitoring, particularly in areas exposed to potential anthropogenic inputs such as industrial emissions or agricultural runoff.

3.4 Health Risk and Hazard Assessment

The Health Risk Index (HRI) for all analyzed metals was below 1, indicating no significant non-carcinogenic risk to human consumers. Likewise, the external hazard index (H_{ex}) values were all lower than the recommended threshold, confirming that the samples do not pose radiological or heavy-metal–related hazards. None of the analyzed elements exceeded the maximum permissible limits established by international food safety authorities such as the FAO/WHO and Codex Alimentarius [40].

The low HRI values suggest that milk from both domestic and commercial sources in Bangladesh is safe for regular consumption with respect to heavy-metal exposure [41] Figure 4. The Hazard Index (HI) for both adults and children varied across the different types of domestically and commercially produced cow's milk samples. In domestic milk, Samples 2 and 3 for adults, as well as Samples 1 and 11 for children, exhibited HI values slightly higher than 1. In commercial milk samples, Samples 5, 6, 8, 12, and 15 showed HI values greater than 1 for adults, while Samples 1, 6, 7, and 12 exceeded the threshold value of 1 for children.

3.4 Carcinogenic and Toxic Metal Evaluation

Carcinogenic and toxic metals including As, Cr, Pb, Hg, and Ni were either below the detection limits or present in negligible amounts. Their concentrations were well within the acceptable dietary limits, implying no carcinogenic or toxicological risk associated with milk intake from the studied regions [42]. The minimal contamination may be due to the limited industrialization of the sampling sites and relatively low use of chemical fertilizers and pesticides in local dairy farming systems.

4 Conclusions

This study analyzed Ca, Cr, Mn, Fe, Co, Ni, Cu, Zn, As, Se, Rb, Sr, Hg, and Pb in 30 milk samples (15 domestic and 15 commercial) collected from 15 districts of Bangladesh using EDXRF. Ca, Fe, Zn, Se, Sr, and Hg were detected in most samples, while Cr, Mn, Co, Ni, Cu, As, and Rb appeared only in a few. Commercial milk contained higher Ca levels than domestic milk. The LODs for key elements were: Cr < 0.064, Ni < 0.042, Cu < 0.81, As < 0.011, Cd < 0.28, and Pb < 0.064 μg/mL.

Elemental concentrations varied across regions due to geological differences. All health risk indices were below 1, and no sample exceeded permissible heavy metal limits. In domestic raw milk samples, HI values slightly above 1 were observed for Samples 2 and 3 (adults) and Samples 1 and 11 (children). In commercial milk, Samples 5, 6, 8, 12, and 15 (adults) and Samples 1, 6, 7, and 12 (children) exceeded HI >1. Carcinogenic metals (As, Cr, Pb, Hg, Ni) remained below detection limits, indicating no carcinogenic or toxicological risk. Overall, all milk samples were considered safe for consumption.

Acknowledgement

The authors highly acknowledged the assistance of the staff members of the Atmospheric and Environmental Chemistry Laboratory, Chemistry Division, Atomic Energy Centre, Dhaka.

References

1. Y.W. Park, M. Juárez, M. Ramos, G.F.W. Haenlein, Physico-chemical characteristics of goat and sheep milk, Small Rumin. Res., 68(1–2), 88–113 (2007).
2. R.M. Tripathi, R. Raghunath, V.N. Sastry, T.M. Krishnamoorthy, Daily intake of heavy metals by infants through milk and milk products, Sci. Total Environ., 227(2–3), 229–235 (1999).
3. P. Licata, D. Trombetta, M. Cristani, F. Giofrè, D. Martino, M. Calò, F. Naccari, Levels of toxic and essential metals in bovine milk from dairy farms in Sicily, Environ. Int., 30(1), 1–6 (2004).
4. R. Khatun, S. Jahan, M.A. Hossain, Comparative analysis of trace metals in cow milk from Bangladesh, J. Environ. Chem. Ecotoxicol., 14(3), 45–52 (2022).
5. M.S. Rahman, N. Akhter, M.J. Uddin, Toxic metals in food and human health impacts: A review, Int. J. Environ. Res. Public Health, 17(9), 3364 (2020).
6. FAO/WHO, Joint FAO/WHO food standards programme: Codex committee on contaminants in foods, Fifth Session, The Hague, Netherlands (2011).
7. Y.J. Cui, Y.G. Zhu, R.H. Zhai, D.Y. Chen, Y.Z. Huang, Y. Qiu, J.Z. Liang, Toxic metals in soils and bioavailability, Environ. Int., 30, 785–791 (2004).
8. S. Akter, S.M.A. Islam, M.O. Rahman, K.M. Mamun, M.J. Kabir, M.S. Rahman, B.A. Begum, M.J. Abedin, S.I. Tushar, Y.N. Jolly, Toxic elements accumulation in vegetables near a fertilizer factory, OA J. Biomed. Eng. Biosci., March 2019, DOI:10.32474/OAJBEB.2019.03.000159.
9. Y.N. Jolly, S. Iqbal, M.S. Rahman, J. Kabir, S. Akter, I. Ahmad, EDXRF detection of heavy metals in Bangladesh cows' milk, Heliyon, 3(9), e00403 (2017).

10. S. Akter, Y.N. Jolly, S. Rahman, J. Kabir, J. Abedin, Elemental analysis procedure using EDXRF 'Epsilon5' system, IOSR-JESTFT, 9(7-II), 11–14 (2015).
11. A. Al Mahmud, T. Hamid, S. Hossain, Y.N. Jolly, S. Akter, J. Kabir, K.M. Mamun, et al., Multi-elemental analysis and trace metal risk evaluation in Bay of Bengal sediments using EDXRF, Next Res., 100941 (2025).
12. A. Islam, Y.N. Jolly, J. Bang. Acad. Sci., 31(2), 16 (2007).
13. M. Ali, S.K. Biswas, S. Akhter, A.H. Khan, Multielement analysis of water residue by PIXE, Anal. Chem., 322, 755–760 (1985).
14. V. Zhitkovich, Chromium in drinking water: sources, metabolism, cancer risks, Chem. Res. Toxicol., 24, 1617–1629 (2011).
15. National Academies of Sciences, Engineering, Medicine, Health and behavior: biological and societal influences, National Academies Press (2001).
16. M.N. Priya, S. Ritu, U.S. Antu, S. Fahmida, M. Hossain, M. Morshed, Heavy metals in raw milk of Bangladesh, Glob. Mainstream J. Health Med. Hosp. Manag., 1(2), 1–13 (2022).
17. L. Friberg, G.F. Nordberg, B. Voûte, Handbook on the Toxicology of Metals, Elsevier, North Holland (1994).
18. S. Akter, S.M. Fahad, S.S. Ashrafi, M.J. Abedin, Y.N. Jolly, J.M. Kabir, M.S. Rahman, B.A. Begum, K.M. Mamun, M.H. Ali, Elemental analysis of leafy vegetables using PIXE in saline Bangladesh region, Biol. Trace Elem. Res., (2021), DOI:10.1007/s12011-021-02866-0.
19. G.M.M.A. Hasan, M.H. Kabir, M.A.S. Miah, Heavy metals in raw and pasteurized milk in Bangladesh, Food Res., 6(1), 233–237 (2022).
20. M.I. Muhib, M.A.Z. Chowdhury, N.J. Easha, M. Rahman, M. Shammi, Z. Fardous, M.L. Bari, M. Kurasaki, Heavy metals in Dhaka cow milk, Int. J. Food Contam., 3, 16 (2016).
21. A. Chamannejadian, G. Sayyad, A. Moezzi, A. Jahangiri, Estimated daily intake of Cd and Pb via rice, Iran J. Environ. Health Sci. Eng., 10(1), 5 (2013).
22. A. Ismail, M. Riaz, S. Akhtar, T. Ismail, Z. Ahmad, M.S. Hashmi, Estimated daily intake and health risk of metals via milk, Food Addit. Contam., B, 8, 260–265 (2015).
23. A. Ara, J.A. Usmani, Lead toxicity: a review, Interdiscip. Toxicol., 8, 55–64 (2015).
24. V. Ríšová, Maternal–child pathway of lead exposure, Interdiscip. Toxicol., 12, 1–6 (2019).
25. V. Potula, W. Kaye, Menopause, lifestyle, and lead levels in former smelter workers, Am. J. Ind. Med., 49, 143–152 (2006).
26. F. Malhat, H. Abdallah, I. Hegazy, Dissipation of chlorantraniliprole in tomatoes, Bull. Environ. Contam. Toxicol., 88, 349–351 (2012).
27. M.T. Islam, M.M. Rahman, S. Akter, Toxic metal contamination in raw and processed milk: Bangladesh case study, Environ. Monit. Assess., 193(7), 456 (2021).
28. C. Griffiths, H. Klemick, M. Massey, C. Moore, S. Newbold, D. Simpson, P. Walsh, W. Wheeler, EPA valuation of water quality improvements, Rev. Environ. Econ. Policy, 6(1), 130–146 (2012).
29. J.O. Olowoyo, M.L. Mutemula, O.O. Agboola, L.L. Mugivhisa, O.O. Olatunji, O.M. Oladeji, Trace metals in fresh milk and health risks, Toxicol. Rep., 12, 361–368 (2024).
30. WHO, Guidelines for drinking-water quality, Vol. 1, World Health Organization (2004).
31. P. Trumbo, A.A. Yates, S. Schlicker, M. Poos, Dietary Reference Intakes for A, K, trace elements, J. Am. Diet. Assoc., 101(3), 294–301 (2001).
32. WHO, Trace elements in human nutrition and health, WHO, Geneva (1996).
33. B. Wan, R. Wang, Y. Sun, J. Cao, H. Wang, J. Guo, D. Chen, Osteogenic microenvironments with Sr–Ca phosphates, Front. Bioeng. Biotechnol., 8, 591467 (2020).
34. C. Reilly, The Nutritional Trace Metals, Blackwell Publishing (2004).
35. Institute of Medicine, Dietary Reference Intakes for Vitamin C, E, Selenium, Carotenoids, Natl. Acad. Press, Washington DC (2000).
36. R. Huque, Y.N. Jolly, T.R. Choudhury, M.K. Munshi, M.S. Hussain, A. Khatun, B.K. Roy, M. Islam, M.A. Hossain, A. Hossain, Elemental and microbial status of raw and pasteurized milk, Int. Food Res. J., 25, 1682–1690 (2018).
37. M.N.E. Alam, A.K.M.A. Ullah, M.M. Hosen, S. Akon, Q. Nahar, F. Jolly, S.B. Quraishi, Macro-micro elements and health risk in branded milks of Dhaka, 2023, DOI:10.21203/rs.3.rs-2942538/v1.
38. FAO, Milk and dairy products in human nutrition, FAO Publ., Rome (2019).
39. J. Sultana, Y.N. Jolly, Md.G. Muktadir, J. Kabir, S. Akter, S. Hossain, K.M. Mamun, K.J. Fatema, Assessment of groundwater quality of a tannery industrial estate in Dhaka, Int. J. Energy Water Resour., published online April 2025, DOI:10.1007/s42108-025-00365-9.
40. M.N.E. Alam, A.K.M.A. Ullah, M.M. Hosen, et al., Essential and trace metals in branded milks in Dhaka, Biometals, 37, 859–875 (2024).
41. M.A. Haque, M.S. Rahman, M.M. Hasan, Heavy metal contamination in Bangladeshi milk and dairy products: A review, Bangladesh J. Anim. Sci., 47(2), 67–75 (2018).
42. M.R. Habib, S. Mahanta, Y.N. Jolly, J.M. Moore, Alleviating heavy metal toxicity in milk and water using high-voltage cold plasma, Biomolecules, 12(7), 913 (2022).

Quantification of Effective Dose in Clinical ^{18}F-FDG Whole Body PET-CT using ICRP 128 Guidelines

S. Das[1*], K.R. Ahmed[1], A.K. Sarker[1], A. Naznin[1], J. Sultana[1], M.R.-Ul-Haque[1], I. Tabassum[1] and Z. Jabin[1]

[1]*Institute of Nuclear Medicine and Allied Sciences (INMAS), Suhrawardy, BAEC, Dhaka- 1207*

Abstract

This retrospective study quantified the effective dose from clinical ^{18}F-FDG whole-body PET-CT scans in 45 adult patients. The effective dose from the computed tomography (CT) component was estimated using dose length product (DLP)-based conversion factors, while the dose of PET component was calculated using ICRP Publication 128 dose coefficients. A strong positive statistical correlation was observed between patient body weight and total effective dose ($r = 0.88$; $R^2 = 0.76$), identifying body weight as the primary factor of radiation exposure. Female patients received a higher mean effective dose (28.5 mSv) compared to males (22.0 mSv), likely due to differences in body composition and organ sensitivity. The mean total effective dose was 25.26 ± 7.25 mSv, with the CT component contributing approximately 85.6% of the total effective dose. These findings highlight the importance of weight-based and sex-specific protocol optimization in PET-CT imaging for enhanced radiation protection.

Keywords: nuclear medicine, PET-CT, effective dose, radiation protection, ICRP 128.

Introduction

The combination of functionality from positron emission tomography (PET) and complete structural anatomy from computed tomography (CT) in a single molecular imaging technique has established PET-CT as a reliable tool in oncology and nuclear medicine. According to the International Commission on Radiological Protection (ICRP), nuclear medicine techniques should be optimized to ensure that radiation exposure is minimized while maintaining accurate imaging, which involves applying the "As Low As Reasonably Achievable (ALARA)" principle through the use of modern equipment, watchful daily practice, trained personnel, reliable quality control systems, and the regular use of diagnostic reference levels to guide those optimizations [1]. Performing dosimetry, including the calculation of organ absorbed doses and effective doses is one of the major assessments that should be done periodically in PET-CT procedures. This is because PET-CT involves the use of radiopharmaceuticals (18F-FDG for the whole body) and the use of X-rays in the CT part; both are the source of ionizing radiation. The radiation exposure of a patient undergoing PET-CT imaging is highly variable, and depends on the imaging protocol, injected activity, scan length, scan duration (minute per bed), and patient-specific factors like body habits and physiology.

Though the benefits of PET-CT are conclusive, the associated exposure of patients to ionizing radiation is a growing concern due to the expanding use of PET-CT in both adults and children for the past few decades. The effective dose to patients from a PET-CT procedure depends on a few parameters like administered activity, patients' size, and other scanning parameters, with the CT component contributing up to 73–80% of the total effective dose according to a previous study [2]. Previous articles showed that CT acquisition parameters are crucial for minimizing radiation burden without compromising diagnostic quality. Previously published 18F-FDG PET-CT demonstrates that the total effective radiation dose is both significant and highly variable, averaging 15.1 ± 4.8 mSv for a whole-body PET-CT scan, with the CT component being the major source of this exposure [3]. By evaluating PET-CT dosimetry, another study determined that the CT scan is the dominant dose contributor (78.2%), necessitating the optimization of CT protocols [4]. Hence, dose assessment in the PET-CT facility of nuclear medicine should be routinely done to ensure overall workflow efficiency and to enhance the safety and reliability of patient care.

This quantitative study assessed the effective dose of 45 adult patients during standard clinical PET-CT tests, aiming to identify the primary radiation exposure source. It calculated and compared effective doses from radiopharmaceutical (18F-FDG) biodistribution (EDPET) and the X-ray component of the CT scan (EDCT), supporting advancements in clinical dosimetry and nuclear medicine protocols.

Materials and Methods

This retrospective study included 45 adult patients who underwent whole body ^{18}F-FDG PET-CT scan at our nuclear medicine institute. Demographic and physiological data including age, sex, height, weight and fasting blood glucose (FBS) were recorded from the patients' clinical history files. All patients fasted at least 6 hours before FDG administration and FBS levels were within the acceptable clinical range (<11 mmol/L) at the time of imaging.

2.1 Imaging Protocol

All the patients are scanned through 128- slice Simens Biograph mCT PET-CT scanner having 4 x 4 x 20 mm lutetium oxyorthosilicate (LSO) detector crystal for higher image quality. The detector delivers sensitivity up to 23.1 cps/kBq[3]. A non-contrast CT and a contrast enhanced CT was performed before PET scan. PET scan was taken at a speed of 1.1 minute per bed. The CT scan parameters were set according to standard diagnostic protocols that involve

*Corresponding author: physudip43@gmail.com

$CTDI_{vol}$-based dose management. The tube voltage was set to 120 kV, reference tube current was 180 mA with automatic exposure control (AEC) system, 3 mm slice thickness was set with acquisition matrix of 128 × 0.6 mm.

2.2 Dose calculation

The Dose length product (DLP) is calculated automatically in the imaging software (syngo.via) according to this formula-

$$DLP = CTDI_{vol} \times l \quad (1)$$

Where, $CTDI_{vol}$ is the volume CT dose index and l is the scan length.

The effective dose from the CT component was calculated using the following equation

$$ED_{CT} = DLP \times k \quad (2)$$

Where, k is the conversion factor ($mSv.mGy^{-1}.cm^{-1}$) for whole body CT scan which is gender optimized according to previous study [5].

The effective dose from the PET component was calculated using this following equation according to ICRP 128

$$ED_{PET} = A \times Dose\ Coefficient \quad (3)$$

Where, ED_{PET} is the effective dose for PET component in (mSv), A is the administrated activity in the unit of (MBq) and Dose coefficient is a constant in the unit of (mSv/MBq) according to ICRP publication 128 [6].

Total effective dose E is the sum of the effective dose for PET and CT component

$$E_{Total} = ED_{CT} + ED_{PET} \quad (4)$$

Finally, calculating the contribution of CT component to total effective dose is calculated using the equation,

$$ED_{CT}(\%) = \frac{ED_{CT}}{ED_{CT}+ED_{PET}} \times 100\% \quad (5)$$

3. Results

This study consists of 45 adult patients (female: 23; male: 22) referred for routine clinical ^{18}F-FDG PET-CT scan. The general demographic data (e.g., age, height, weight) is presented in Table 1. The male and female patients have an age of 47.23 ± 15.13 and 48.91 ± 12.82 which means both groups are in similar age category. The height and weight of male group is 1.63 ± .06 m and 61.73 ± 12.15 kg, and for female group is 1.50 ± .05 m and 61 ± 11.14 kg respectively. Female group has higher weights where both groups have a similar height range indicating higher BMI of female group (female: 26.94 ± 5.27 kg.m^2 vs male: 23.11 ± 4.11 kg.m^2). The fasting blood glucose (FBS) of the 45 patients in this study is 6.24 ± 1.15 mmol/L (4.4-10.2 mmol/L) which is appropriate according to protocol guideline (<11 mmol/L) [7]. The injected radiopharmaceutical activity is 184.7 ± 34.9 per patient with a low dose protocol for higher sensitivity LSO type detector. The injected activity per kg of this study is 3.03 ± 0.24 MBq/kg, which is much below the standard protocol 3.7 MBq/kg [8].

Table 1: Demographics and injected ^{18}F-FDG activity

	Age	Height (m)	Weight (Kg)	FBS (mg/dL)	Injected Activity (MBq)
Mean ± SD	48.45 ± 13.79	1.57 ± 0.08	60.7 ± 10.8	6.24 ± 1.15	184.7 ± 34.9
Min	24	1.40	39	4.4	96.94
Max	75	1.75	82	10.2	254.41
Median	49.5	1.55	60	6.1	186.3

Firstly, for statistical analysis, we have performed Shapiro-Wilk (S-W) test for this smaller sample size (N=45) to evaluate that the data that was normally distributed or not. The demographic data (e.g., Age, height, etc.) and the dosimetry data (e.g., DLP, ED) both are checked for normality by S-W test, which confirms that majority of the variables in the dataset are normally distributed ($p > 0.05$) except FBS which is randomly distributed because of patient specific parameters. As the data is in normal distribution, it is feasible to proceed with subsequent parametric tests such as Pearson correlation.

The correlation analysis was performed on patient demographics and radiation exposure related factors (effective dose) which identified patient weight as the primary determinant of effective dose. Patient weight showed a highly significant and very strong positive correlation with both the administered radiopharmaceutical activity (MBq) ($r = 0.921$, $p < 0.01$) and the CT radiation burden as quantified by the Total Dose-Length Product (DLP) (mGy.cm) ($r = 0.927$, $p < 0.01$). This strong dependence confirms the foundational clinical protocol of mass-based dosing employed for both the nuclear medicine radiopharmaceutical component and the associated computed tomography components. Consequently, strong inter-correlations were observed among all calculated effective dose measures, reflecting their common primary dependency on administered activity/CT factors influenced by weight (e.g., Total Effective Dose, E_{Total}) and Effective Dose from CT (ED_{CT}), $r = 0.999$, $p < 0.01$).In contrast, neither Age nor Height demonstrated a statistically significant linear relationship with any of the primary radiation dose parameters investigated within this study sample (N=45), indicating that they are not primary independent variables dictating overall radiation exposure in this clinical setting.

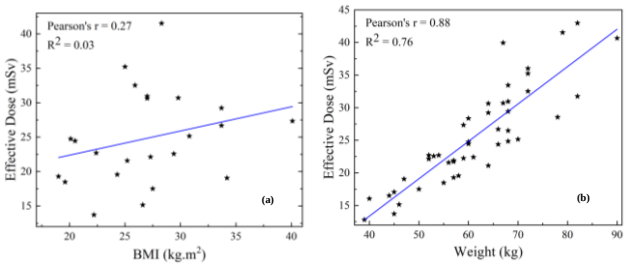

Fig. 1: Correlation between effective dose and (a) body mass index (BMI), (b) weight of patients

Fig. 1 shows the relationship between effective radiation dose and two distinct anthropometric parameters (body

weight and BMI). Specifically, the data shows a robust linear dependence between patient body weight (kg) and effective dose (mSv), quantified by a Pearson correlation coefficient of r = 0.88 and a coefficient of determination, R^2 = 0.76. This high R^2 value means that 76% of the value of effective dose is statistically dependent on variations in body weight of the patients. On the other hand, the correlation between Body Mass Index (BMI) and effective dose is considerably weaker (r= 0.27; $R^{2=}$ 0.03). These statistical outcomes highlight patient body weight as a major determinant for predicting and optimizing individual radiation dose protocols, advocating for its primary consideration in developing precise, mass-dependent dose modulation algorithms to ensure radiation protection guidelines.

The final computed effective dose of the patients of this study is 25.26 ± 7.25 mSv, which is close to previously mentioned values of effective doses in these previously reported articles (20 ± 5.20 mSv [9], 21.64 ± 5.20 mSv [10]). Also, the CT component contributes up to 85.6% of total effective dose in this study which is slightly higher than some previously reported values [11], [12], [13]. Higher percentage value is for low weight based FDG protocol is used for radiopharmaceutical administration.

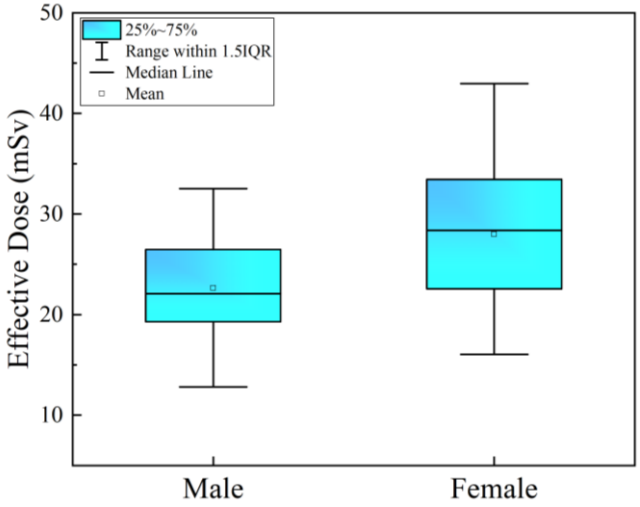

Fig. 2: Comparison of effective dose (mSv) between male and female groups

The analysis of gender-based dosimetry data is summarized in the box plot (**Figure 2**). A statistically significant divergence in the distribution of the effective radiation dose (mSv) between male and female patients is seen. Particularly, the effective dose for the female group is higher than the male group (Male: 28.5 mSv vs Female: 22.0 mSv). Also, the dose distribution reveals that the interquartile range (IQR) that represents the central 50% of the data, is not only translated to higher dose values for females (22.5 mSv to 33.5 mSv) but also shows a wider spread compared to the male group (19.5 mSv to 26.5 mSv). This quantitative difference in absorbed dose suggests that standard imaging protocols, even when adjusted for gross size metrics like weight (as established in the previous analysis), may still result in an elevated effective dose for female patients, likely due to differences in average body weight, tissue composition, or the presence of highly radiosensitive organs within the scan field of view. The BMI of the female patients are higher than the male patients in this study (23.12 ± 4.1 kg/m^2 for male and 26.94 ± 5.2 kg/m^2 for female group) which is very common for South-Asian region [14]. These findings underline a critical need for the development and implementation of advanced sex-specific dose optimization strategies to mitigate unwarranted radiation exposure and enhance personalized radiological protection.

4. Discussion

The present study demonstrates that patient body weight is the most significant determinant of effective radiation dose in clinical ^{18} F-FDG PET-CT imaging, consistent with previously reported findings in the literature. The observed strong correlation between body weight and effective dose reflects the routine use of mass-based radiopharmaceutical administration and automatic exposure control mechanisms in CT acquisition.

The CT component accounted for approximately 85.6% of the total effective dose, which is slightly higher than values reported in earlier studies (typically 73–80%). This increased contribution may be attributed to the adoption of a low weight-adjusted FDG protocol in the PET component, thereby proportionally increasing the relative contribution of CT exposure. Similar trends have been reported in recent international studies where CT remains the dominant contributor to total PET-CT dose despite advancements in PET detector sensitivity.

A statistically significant difference in effective dose was observed between male and female patients, with females receiving higher average doses. This finding is consistent with international dosimetry reports and may be explained by differences in body composition, fat distribution, and the presence of radiosensitive organs within the scanned field of view. These results highlight the limitations of using body weight alone as a surrogate for dose optimization and suggest the potential benefit of incorporating sex-specific correction factors into PET-CT protocols.

From a clinical perspective, these findings underscore the importance of individualized dose optimization strategies that consider both patient body weight and sex. Implementing such precision-based protocols could reduce unnecessary radiation exposure while maintaining diagnostic image quality, in alignment with the ALARA principle and international radiation protection recommendations.

5. Conclusion

This study confirms that the CT component is the dominant source of radiation exposure in clinical ^{18} F-FDG whole-body PET-CT imaging. Patient body weight was identified as the most significant factor influencing total effective dose, whereas BMI, age, and height showed limited predictive value. A significant gender-based difference in

effective dose was observed, emphasizing the need for sex-specific dose optimization strategies. These findings support the transition from conventional protocol-based imaging toward precision-driven, patient-specific dose management approaches to enhance radiation safety in nuclear medicine practice.

References

1. B. Aubert et al., "ICRP Publication 105. Radiological Protection in Medicine," Dec. (2024).
2. B. Adeleye and N. Chetty, "Radiation dose from 18F-FDG PET/CT procedures: Influence of specific CT model and protocols," Radioprotection, vol. 53, Nov. (2018)
3. J. M. Martí-Climent et al., "Effective dose estimation for oncological and neurological PET/CT procedures," EJNMMI Res, vol. 7, no. 1, (2017)
4. F. G. Paiva, P. do Carmo Santana, and A. P. Mourão, "Evaluation of patient effective dose in a PET/CT test," Applied Radiation and Isotopes, vol. 145, pp. 137–141, Mar. (2019)
5. Y. Inoue, K. Nagahara, Y. Tanaka, H. Miyatake, H. Hata, and T. Hara, "Methods of CT Dose Estimation in Whole-Body ^{18}F-FDG PET/CT," Journal of Nuclear Medicine, vol. 56, no. 5, pp. 695–700, May (2015)
6. S. Mattsson et al., "ICRP Publication 128: Radiation Dose to Patients from Radiopharmaceuticals: a Compendium of Current Information Related to Frequently Used Substances," Ann ICRP, vol. 44, no. 2_suppl, pp. 7–321, Jul. (2015)
7. J. P. Pijl, A. W. J. M. Glaudemans, O. Gheysens, R. H. J. A. Slart, and T. C. Kwee, "Importance of Blood Glucose Management Before 18F-FDG PET/CT in 322 Patients with Bacteremia of Unknown Origin," Journal of Nuclear Medicine, vol. 64, no. 8, pp. 1287–1294, (2023)
8. R. Vali et al., "SNMMI procedure standard/EANM practice guideline on pediatric ^{18}F-FDG PET/CT for oncology 1.0," Society of Nuclear Medicine Inc. Jan. 01, (2021)
9. J. M. Martí-Climent et al., "Effective dose estimation for oncological and neurological PET/CT procedures," EJNMMI Res, vol. 7, no. 1, (2017)
10. Y. Li, L. Jiang, H. Wang, H. Cai, Y. Xiang, and L. Li, "Effective radiation dose of 18F-FDG PET/CT: How much does diagnostic CT contribute?" Radiat. Prot. Dosimetry, vol. 187, no. 2, p. 183, (2019)
11. O. Mahgoub et al., "Evaluation of Patient radiation exposure from brain PET/CT protocol at a PET/CT center in Almana hospital," Radiation Physics and Chemistry, vol. 235, p. 112853, (2025)
12. A. Sulieman et al., "Estimating the patient's effective doses and setting a diagnostic reference level for PET/CT procedures," Radiation Physics and Chemistry, vol. 232, p. 112644, (2025)
13. M. Malekhedayat et al., "Use of diagnostic vs low-dose computed tomography in positron emission tomography-CT examinations," Eur. Radiol., vol. 35, no. 9, pp. 5468–5477, Sep. (2025)
14. F. B. Hossain, G. Adhikary, A. B. Chowdhury, and M. S. R. Shawon, "Association between body mass index (BMI) and hypertension in south Asian population: Evidence from nationally representative surveys," Clin. Hypertens. Dec. 15, (2019)

Measurement of natural radioactivity and radiation hazard in soil, sediment, and water near nuclear power plant in Bangladesh

S. Paul[a], M.A. Haydar[a], K. Fatema[a], M.B. Shohag[b], A. Sen and K. Uddin

[a]*Health Physics and Radioactive Waste Management Unit (HPRWMU), Institute of Nuclear Science and Technology (INST), Atomic Energy Research Establishment (AERE), Bangladesh Atomic Energy Commission (BAEC)*
[b]*Center for Research Reactor, Atomic Energy Research Establishment (AERE), Bangladesh Atomic Energy Commission (BAEC)*
[c]*Department of Physics, Jagannath University, Dhaka 1100, Bangladesh*

Abstract

This study presents the natural radioactivity levels in soil, sediment and water samples collected from the Padma River near the ongoing nuclear power project in Rooppur, Bangladesh. A High-Resolution Germanium detector is used to analyze the processed samples. The average activity concentrations of ^{226}Ra, ^{232}Th, and ^{40}K in soil samples are found to be 43.53±6.83 Bq.kg^{-1}, 63.57±8.19 Bq.kg^{-1}, and 690.14±84.48 Bq.kg^{-1}, respectively. The same for the sediment samples (20 cm deep in the water) are 34.51±5.43 Bq.kg^{-1}, 50.03±6.52 Bq.kg^{-1} and 502.08±67.26 Bq.kg^{-1}, respectively. For water samples, the average activity concentrations of ^{226}Ra and ^{232}Th are observed as 1.13±0.57 Bql^{-1} and 0.91±0.27 Bql^{-1}, respectively. The average absorbed dose rate for soil and sediment samples is found to be 87.49 nGyh^{-1} and 67.24 nGyh^{-1}, respectively. The estimated outdoor annual effective dose for soil and sediment samples is found to be 0.11 mSv y^{-1} and 0.08 mSv y^{-1}, respectively. The values of radium equivalent activity in almost all the samples were less than 370 Bq.kg^{-1}. The external hazard index for soil and sediment samples varied between 0.47 to 0.53 and 0.29 to 0.59, respectively. Results of the study could serve as a baseline radiometric data for monitoring initiative in the study area.

***Keywords**:* Activity Concentration, External hazard index (Hex), HPGe detector, Natural radioactivity.

1 Introduction

Natural radionuclides found in nature shows the level of radioactivity which is termed as background radiation. Soil, sediments, ground and underground water contains various types of radionuclides in different concentrations. The natural radioactivity and the associated external exposure due to gamma radiation are different in each region in the world [1-4]. Human beings cannot avoid the exposure of this radiation. Widely spread natural radionuclides present in the environment come from the family of primordial radionuclides; Uranium (^{238}U), Thorium (^{232}Th), Actinium (^{235}Ac) and Potassium (^{40}K) [5]. A significant amount of man-made radionuclides, ^{137}Cs and ^{90}Sr, may also be present in the environment. Usually the concentrations of radionuclides within the earth environment are not harmful to humans. The background radiation can be high due to the pollution of environment with radioactive materials or the installation and handling of radioactive materials in any region. In Bangladesh, a nuclear power plant (NPP) is under construction on the bank of the mighty river Padma. A large amount of radioactive materials will be handled in the plant. Therefore, there is a potential for increased concentrations of radioactive materials in the vicinity of the power plant.

The present study aims to survey the baseline radiation to the adjacent area, especially the bank of Padma River where the power plant of 2400 MW capacity (1200 MW each) is going to be operated. The soil, sediments and water samples around the project area are collected, processed in a laboratory and tested using the high-resolution germanium detector (HPGe). In this study, the concentration level of ^{226}Ra, ^{232}Th, and ^{40}K in soil, sediments and water samples collected beside the ongoing project in Pabna, Bangladesh. The data will provide useful information in the monitoring of contamination near the NPP. Spatial and temporal variations of radioelements can help to determine root cause of a corresponding increase or decrease of a certain health characteristics and lead to improved policy.

2 Materials and Methods

2.1 Study Area

The survey area is selected to provide a baseline data against which any accidental release of radioactive material from the plant. Rooppur is under the district of Pabna, Bangladesh. It is located at 24.1500°N 89.0667°E. Rooppur is on the east side of the river Padma, a very important river passing through Bangladesh. Fig. 1 shows the study area where the sampling places are marked by green dots with number 1 to 6. Ongoing Rooppur Nuclear Power Plant (RNPP) is just beside the dot-4.

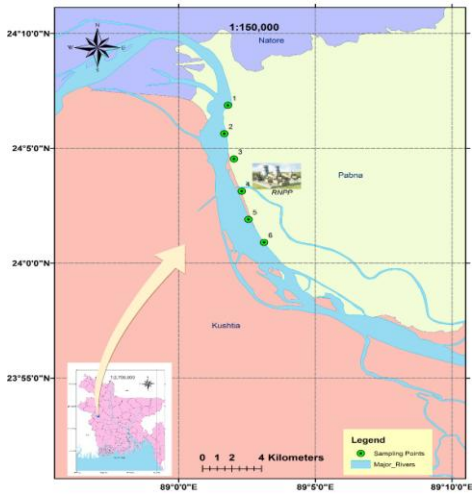

Fig. 1: **S**ampling area (using ArcGIS Software) at the bank of Padma River near Rooppur, Pabna, Bangladesh.

*Corresponding author: shampa52@yahoo.com

2.2 Sampling Location

A total of 18 samples (6-soil, 6-sediment, and 6-water) were collected from the bank of Padma River near the plant. It is approximately 200 km northwest of the city Dhaka, the capital of Bangladesh. The samples were collected during the whole day on 26-27 April 2019. The sampling area of Padma River is in between 24°6' 52" N to 24°00' 33" N and 89°01' 48" E to 89°01' 01" E.

2.3 Sample Collection and Preparation

Soil, sediment, and water samples were collected from almost equidistance location with a distance of about 2 km from one sample to another sample. The soil samples were collected from the bank of the river and the sediment samples were collected about 20 cm deep in the water. About 1.0 to 1.5 kg soil and sediment samples and 2.0 liters water sample were collected from each sampling location. Soil and sediment samples were packed separately in plastic bag and water samples were collected in plastic containers. All the samples were marked with identification parameters such as sample name, sample no, location, date, etc. Finally, all the samples were transported to the laboratory of the Health Physics and Radioactive Waste Management Unit (HPRWMU), Bangladesh Atomic Energy Commission (BAEC), Savar, Dhaka for processing and characterization.

2.3.1 Processing of the Solid Samples

The samples were dried in the sun for several days on the roof. The samples were then cleaned for stones, grass-roots, vegetation, etc. and crushed into fine powder by using a grinder and collected after passing through 400 μm mesh screen. The homogenized samples were then dried in an oven at about 100°C for about 24 hours. The homogenized samples were then transferred to sealable cylindrical plastic containers of 7cm height and 5.5cm in diameter and the weights of the samples were recorded using an electrical balance. The sample filled plastic containers were sealed tightly with a cap and wrapped with thick vinyl tape around their necks. All the containers were marked individually with identification parameters e.g., name and location of the samples, date of preparation and net weight. Then all the prepared samples were stored for about 30 days to assume secular equilibrium between ^{226}Ra and ^{232}Th series and their daughter progenies.

2.3.2 Processing of the Liquid Samples

Cylindrical type beakers (1.5-liter capacity) were used to measure the volume of the water samples. At first, the beaker was cleaned with deionized water and dried. After measuring the volume of water samples (1000ml), samples were transferred to sealable Marinelli beakers of 15 cm height and 12.5 cm diameter. Acidic water is specious for conservation. Before preserving we have mixed 3ml concentrated HNO_3 with every 1000 ml water samples so that the aquatic organism living in the water will die. The pH value of the water maintained to 2 or less.

The weights of the samples were recorded using an electrical balance. The sample filled Marinelli beakers were sealed tightly with a cap and wrapped with thick vinyl tape around their necks. And the containers were marked with identification parameters. All the prepared samples were stored for about 30 days for achieving secular equilibrium between gaseous and nongaseous decay products of naturally occurring radionuclide series.

2.4 Measurement

The detection and measurement of radionuclides in the samples were carried out by gamma spectrometry system using a vertical coaxial cylindrical high purity germanium (HPGe) detector of 172 cm^3 active volume and 20% relative efficiency. The p-type HPGe detector was supplied by CANBERRA (Model GC2018). The detector was coupled to a 16 k-channel computer analyser. The analysis was carried out using Genie 2000 software, which matched various gamma energy peaks to a library of possible radionuclides. All the solid samples were counted for 10ks and liquids were 20ks. Prior to the measurement of samples, the environmental gamma background at the laboratory site was determined with an identical empty plastic container used in the sample measurement. The energy range selected for the corresponding radionuclides were 295 KeV (18.42%) and 352 KeV (35.6%) of ^{214}Pb and 609 KeV (45.49%), 1120 KeV (14.92%) and 1764 KeV (15.3%)of ^{214}Bi for ^{226}Ra, 583 KeV (85%) and 2614 KeV of ^{208}Tl, 911 KeV (25.8%) and 969 KeV of ^{228}Ac for ^{232}Th, 1460 KeV (10.66%) for ^{40}K and 661.66 KeV for ^{137}Cs (85.10%) [5].

2.4.1 Calibration of the Detector

In order to determine the detector efficiency for solid and liquid matrix, standard sources were made for different geometry. Using ^{152}Eu of known activity with Al_2O_3 matrix in plastic pot standard source, the counting efficiency curve of the HPGe detector for solid matrix is calibrated (as shown in Fig.2).

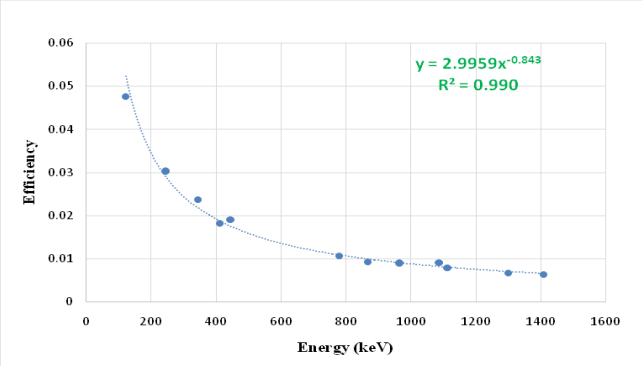

Fig. 2: Efficiency curve of the HPGe detector of 20% relative efficiency for the solid matrix.

The counting efficiency for radionuclides presents in the water samples was determined using a calibration standard prepared by mixing a known activity of ^{152}Eu with 1 L of deionized water in a Marinelli beaker. An efficiency calibration curve was subsequently generated, as illustrated in Fig. 3

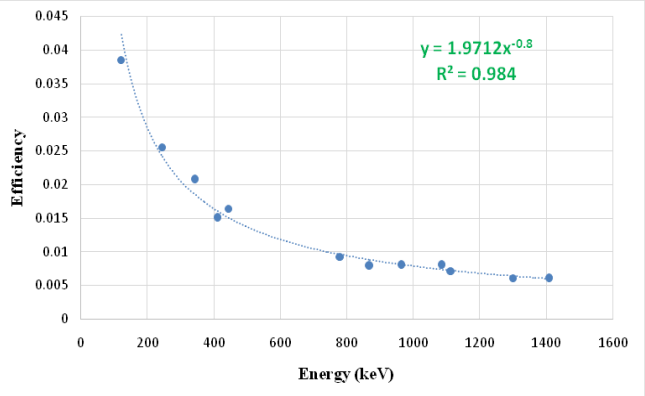

Fig. 3: Efficiency curve of the HPGe detector of 20% relative efficiency for the liquid samples.

2.4.2 Activity Calculation

The net amount of the sample is obtained by subtracting a linear background distribution of the pulse height spectra from the corresponding peak energy area. From the sample net counts, activity of the samples were calculated [6] using the equation (1).

$$A = \frac{CPS}{E_\gamma \times I_\gamma \times W} \quad (1)$$

Where, A = Activity concentrations of the sample in Bq.kg-1 or BqL^{-1}.

cps= The net counts per second

E = The counting efficiency of the gamma energy

I = Absolute intensity of the gamma ray and

W = Net weight of the sample (in kilogram or litre).

The combined uncertainty of the activity concentration [7] was estimated using the following equation (2)s

$$\frac{\Delta A}{A} = \sqrt{\left(\frac{\Delta N}{N}\right)^2 + \left(\frac{\Delta I_\gamma}{I}\right)^2 + \left(\frac{\Delta t}{t}\right)^2 + \left(\frac{\Delta m}{m}\right)^2 + \left(\frac{\Delta E_\gamma}{E}\right)^2} \quad (2)$$

where, $\Delta A/A$ is the combined standard uncertainty of the sample measurement and ΔN, ΔI_γ, Δt, Δm, and ΔE_γ are the uncertainties of the net count rate, gamma-ray intensity, counting time, sample weight and efficiency, respectively.

In this study, the minimum detectable activity (MDA) for the gamma-ray measuring system was computed by the equation (3) [8-11]:

$$\text{MDA } (\text{Bq.kg}^{-1} \text{ or } Bq.L^{-1}) = \frac{C_F \times \sqrt{B}}{E_\gamma \times I_\gamma \times t \times w} \quad (3)$$

where, CF is the statistical coverage factor (=1.64) for 95% confidence level; B is the background counts over the region of interest for each radionuclide; t, the measuring time in seconds. None of the analyzed samples contains detectable amount of artificial radionuclides (here, ^{137}Cs). The average values of minimum detectable activities (MDAs) of ^{226}Ra, ^{232}Th, ^{40}K, and ^{137}Cs in the determined solid samples are 1.01, 1.78, 19.13 and 0.18 $Bq.kg^{-1}$, respectively whereas for water samples MDAs for ^{226}Ra, ^{228}Ra, ^{228}Th, ^{40}K, and ^{137}Cs are 0.22, 0.64, 0.09, 5.28 and 0.06 $Bq.l^{-1}$, respectively.

2.4.3 Absorbed Dose Rate

The external outdoor absorbed gamma dose rates due to terrestrial gamma rays from the nuclides ^{226}Ra, ^{232}Th, and ^{40}K at 1m above the ground level has been calculated as [12]:

$$D\ (nGyh^{-1}) = 0.462\ A_{Ra} + 0.604\ A_{Th} + 0.042\ A_K \quad (4)$$

Where, A_{Ra}, A_{Th}, and A_K are the specific activities of ^{226}Ra, ^{232}Th and ^{40}K respectively in $Bq.kg^{-1}$.

2.4.4 Outdoor Annual Effective Dose

The absorbed dose rate was converted into an annual effective dose equivalent by using a conversion factor of 0.7 $SvGy^{-1}$ recommended by the UNSCEAR 2000 and 0.2 for the outdoor occupancy factor by considering that the people on the average, spent 20% of their time in outdoors[13]. The effective dose due to natural activity in the soil and sediment samples has been calculated by:

$$E(mSvyr^{-1}) = D \times 24 \times 365.25 \times 0.2 \times 0.7 \times 10^{-6} \quad (5)$$

2.4.5 Radium Equivalent Activity

The radionuclide ^{226}Ra, ^{232}Th, and ^{40}K are not homogeneously distributed in sediment and soil. The inhomogeneous distribution from naturally occurring radionuclide is due to disequilibrium between ^{226}Ra and its decay products. For uniformity in exposure estimates, the radionuclide concentrations are defined in terms of 'Radium equivalent activity' (Ra_{eq}) in $Bq.kg^{-1}$. This allows comparison of the specific activity of materials containing different amounts of ^{226}Ra, ^{232}Th, and ^{40}K according to Beretka and Mathew [14] as follows:

$$Ra_{eq}\ (Bq.kg^{-1}) = A_{Ra} + 1.43\ A_{Th} + 0.077\ A_K \quad (6)$$

2.4.6 External Hazard Index

The external hazard index (H_{ex}) is the indoor radiation dose rate due to the external exposure to gamma radiation in constructive materials of dwelling which has been calculated by [15].

$$H_{ex} = \frac{A_{Ra}}{370} + \frac{A_{Th}}{259} + \frac{A_K}{4810} \quad (7)$$

3 Results and Discussions

The results of the present study on the three types of samples are summarized in following sections.

3.1 Radioactivity in the Soil Samples

Activity concentration values of the radionuclides ^{226}Ra, ^{232}Th and ^{40}K in the soil samples have been determined by equation (1) and the combined uncertainty was calculated using equation (2). The graphical representation of activity concentration has been shown in Fig 3.

3.2 Activity Concentrations of Radionuclides ^{226}Ra, ^{232}Th and ^{40}K in Soil Samples

In the soil samples, the activity concentrations of ^{226}Ra were found to be in the range of 38.48±7.03 Bq.kg-1to 48.63±6.59 $Bq.kg^{-1}$, with an average value of 43.54±6.83 $Bq.kg^{-1}$. The result found in the present study was slightly higher than the worldwide average value of 35 $Bq.kg^{-1}$ [1].

The activity concentrations of ^{232}Th were found to be in the range of 53.78±7.39 Bq.kg^{-1} to 68.42±9.21 Bq.kg^{-1}, with an average value of 63.57±8.19 Bq.kg^{-1} which was higher than the worldwide average value of 30 Bq.kg^{-1}. The activity concentration of ^{40}K in the soil samples was observed to be comparatively higher than that of both ^{226}Ra and ^{232}Th in the investigated area. It's value ranged from 589.01±77.10 Bq.kg^{-1} to 775.16±94.31 Bq.kg^{-1}, with an average value of 690.25±84.48 Bq.kg^{-1}. This value was significantly higher than the worldwide average value of 400 Bq.kg^{-1}. The average activity concentration of the radionuclides in the soil samples was in this order ^{40}K>^{232}Th>^{226}Ra.

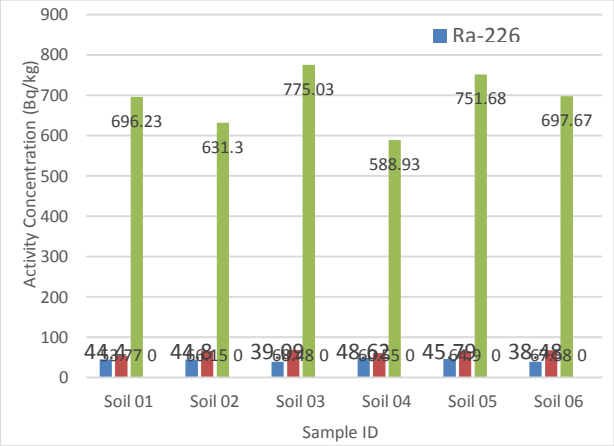

Fig. 4: Distribution of ^{226}Ra, ^{232}Th and ^{40}K in soil samples.

3.3 Radioactivity in the Sediment Samples

Activity concentration values of the radionuclides ^{226}Ra, ^{232}Th and ^{40}K in the sediment samples have been determined by equation (1) and the combined uncertainty was calculated by equation (2). The graphical representation has been shown in Fig 4.

3.4 Activity Concentrations of Radionuclides ^{238}U, ^{232}Th and ^{40}K in Sediment Samples

The activity concentrations of ^{226}Ra were found to be in the range of 23.32±4.70 Bq.kg^{-1} to 60.72±6.44 Bq.kg^{-1}, with an average value of 34.51±5.43 Bq.kg^{-1}. The result found in the present study was slightly lower than the worldwide average value of 35 Bq.kg^{-1}[1]. The activity concentrations of ^{232}Th were found to be in the range of 27.56±5.34 Bq.kg^{-1} to 89.73±7.87 Bq.kg^{-1}, with an average value of 50.03±6.52 Bq.kg^{-1} which was higher than the worldwide average value of 30 Bq.kg^{-1}. The activity concentration of ^{40}K was observed to be comparatively higher than that of both ^{226}Ra and ^{232}Th in all soil samples of the investigated area. Its value ranged from 380.51±62.58 Bq.kg^{-1} to 610.96±79.10 Bq.kg^{-1}, with an average value of 502.08±67.26 Bq.kg^{-1}. This value was higher than the worldwide average value of 400 Bq.kg^{-1}. The average activity concentration of the radionuclides in the sediment samples was in this order ^{40}K>^{232}Th>^{226}Ra. Besides, the average radioactivity concentration of ^{226}Ra (^{238}U), ^{232}Th, and ^{40}K in soil and sediment samples of our study is compared to those of previously published works [4], [16]–[20] in Table 1.

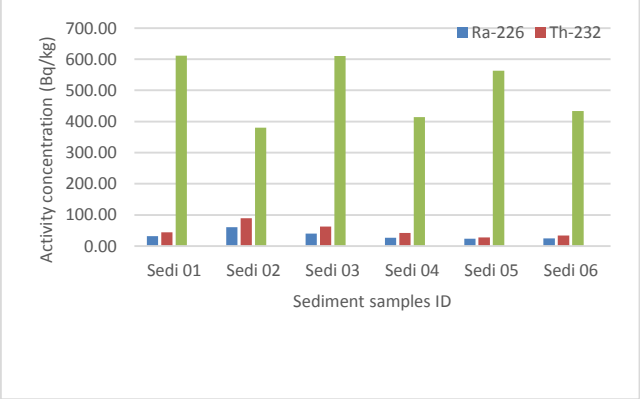

Fig. 5: Distribution of ^{226}Ra, ^{232}Th and ^{40}K in sediment samples.

Table 1: Comparison of average radioactivity concentration of ^{226}Ra (^{238}U), ^{232}Th, and ^{40}K in soil and sediment samples (Present study) with the other literature values studied elsewhere in the world

Sample Type	Location	Activity Concentration			References
		^{226}Ra	^{232}Th	^{40}K	
Soil samples	Nigeria	7.41 ± 0.44	16.27 ± 0.84	196.11 ± 9.08	[16]
	South Africa (phosphate rock storage facility)	31.73 ±12.89	31.56 ± 16.16	138.07 ± 72.90	[17]
	Iraq	34.80	18.80	289.20	[4]
	Malnichera Tea Garden in Sylhet District of Bangladesh	55.25 ±4.68	125.27± 5.81	497.91±43.83	[18]
	Tanzania	-	36±3	564± 10	[19]
	Panipat, India	-	29.89 ± 0.61	291.06 ± 0.57	[20]
	Potenga sea beach, Bangladesh	65.90 ± 5.74	83.17 ± 4.83	946.9 ± 5.9	[21]
	RNPP Site, Pabna, Bangladesh	30.85	40.88	390.10	[22]
	Around Padma River Rooppur, Bangladesh	43.54±6.83	63.57±8.1	690.25±84.48	Present Study
	RNPP site, Padma River	44.59 ± 4.58	67.64 ± 7.93	782.68±108.11	[23]

Sample Type	Location	Activity Concentration			References
		^{226}Ra	^{232}Th	^{40}K	
Sediment samples	Turkey	72.42	79.58	812.37	[24]
	India, Ponnaiyar river	6.43 ± 2.71	52.76 ± 5.40	395.67 ± 27.93	[25]
	Jessore, Bangladesh	43±11	48 ± 14	503 ± 143	[12]
	Around Padma River Rooppur, Bangladesh	34.51±5.43	50.03±6.52	502.08±67.26	Present study

The activity concentrations of ^{226}Ra, ^{232}Th, and ^{40}K measured in the present study around the Padma River, Rooppur, are higher than those reported for soils from Nigeria, Iraq, and some regions of India, but comparable to other locations in Bangladesh. For sediment samples, the values are consistent with reports from Bangladesh and India, lower than those from Turkey, and higher than those from the Ponnaiyar River, India. These variations are mainly attributed to differences in local geology, alluvial sediment deposition, mineralogical composition, and land-use practices. Overall, the measured activity concentrations fall within normal regional and global background levels.

3.5 Radioactivity in the Water Samples

Activity concentration values of the radionuclides ^{226}Ra, ^{232}Th and ^{40}K in the water samples have been determined by equation (1) and the combined uncertainty was calculated by equation (2). The graphical representations have been shown in Fig. 6.

3.6 Activity Concentrations of Radionuclides ^{226}Ra, ^{232}Th and ^{40}K in Water Samples

The activity concentrations of ^{226}Ra and ^{232}Th were found to be in the range of <MDA to 1.39±0.31 Bq.l^{-1} and <MDA to 1.44±0.30 Bq.l^{-1}, with an average of 1.13±0.57 Bq.l^{-1} and 0.91±0.27 Bq.l^{-1}, respectively. Besides, the activity concentration ^{40}K was lower than the minimum detectable activity of counting system and <MDA. Moreover, comparison of average radioactivity concentration of the identified radionuclides in surface water samples (Present study) with the other literature values [19], [26]–[32] for surface water studied elsewhere in the world is shown in Table 2.

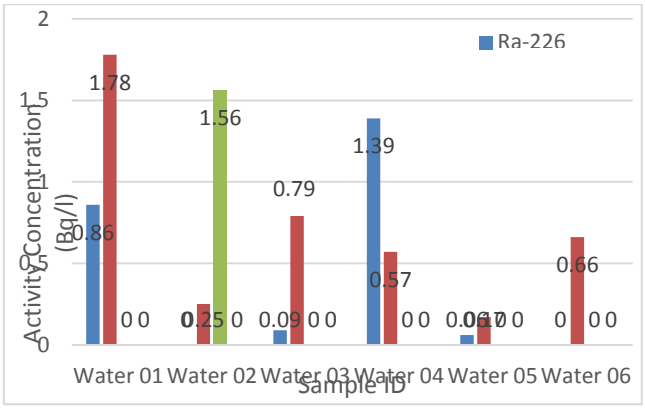

Fig. 6: Distribution of ^{226}Ra, ^{232}Th and ^{40}K in water samples.

Table 2: Comparison of average radioactivity concentration of ^{226}Ra, ^{232}Th, and ^{40}K in surface water samples (Present study) with the other literature values for surface water studied elsewhere in the world

Site	Activity levels (Bq.l^{-1})			References
	^{226}Ra	^{232}Th	^{40}K	
Padma River, Adjacent to RNPP Site, Bangladesh	(<MDA-1.39)	(<MDA-1.44)	<MDA	Present Study
Habigonj District, Bangladesh	(1.45 - 13.1)	(0.0 - 14.02)	-	[26]
Rooppur RNPP Site, Bangladesh	(0.11- 0.21)	(0.13 - 0.30)	-	[27]
Karnafully River, Chittagong, Bangladesh	(1.72 - 3.20)	(3.01- 0.76)	-	[28]
Ghana	0.0137	0.0012	-	[29]
Nigeria	12	12	97	[30]
Nduluma River in Arusha, Tanjania	2.35	1.85	10.1	[19]
Northwestern areas of Pakistan	0.0039	0.002	0.19	[31]
Al-Hurrah city, Iraq	2.31	0.98	22.29	[32]

The activity concentrations in surface water from the Padma River near the RNPP site were below the MDA and are lower than most values reported in Bangladesh and other countries. The lower levels are mainly due to high river dilution, sedimentation processes, and the absence of significant anthropogenic inputs. Overall, the results indicate normal background radioactivity in the study area.

3.7 Radiological Hazard Assessment

In order to assess the health effects, the radiological hazards such as radium equivalent activity Ra_{eq} (Bq/kg), external hazard index (H_{ex}), absorbed dose rate D (nGy.h^{-1}), and outdoor annual effective dose E (mSv yr^{-1}) were calculated from the activity concentration of ^{226}Ra, ^{232}Th, and ^{40}K. Radium equivalent activity Ra_{eq} (Bq/kg), external hazard index (H_{ex}), absorbed dose rate D (nGy.h^{-1}), and outdoor annual effective dose E (mSv yr^{-1}) were calculated by equation (3), (4), (5), and (6) respectively.

3.8 Radiological Hazard Assessment for Soil Samples

Table 3 shows the radium equivalent activity Ra_{eq} (Bq.kg^{-1}), external hazard index (H_{ex}), absorbed dose rate D (nGy.h^{-1}), and outdoor annual effective dose E (mSv yr^{-1}) of soil samples. The radium equivalent activity Ra_{eq} (Bq.kg^{-1}) were found to be varied from 174.90 Bq.kg^{-1} to 196.69 Bq.kg^{-1} with an average value of 187.58 Bq.kg^{-1}, which was lower than the worldwide average value 370 Bq.kg^{-1} [1]. The external hazard index (H_{ex}) was found to be varied from 0.47 to 0.53 with an average value of 0.51, which was lower than the worldwide average value of 1.00. Absorbed dose rate D (nGy.h^{-1}) were found to be varied from 82.23 nGy.h^{-1} to 91.97 nGy.h^{-1} with an average value of 87.49 nGy.h^{-1}, which was higher than the worldwide average value 55.00 nGy.h^{-1}. Outdoor annual effective dose E (mSv yr^{-1}) were found to be varied from 0.10 mSv yr^{-1} to 0.11 mSv yr^{-1} with an average value of 0.11 mSv yr^{-1}, which was higher than the worldwide average value 0.07 mSv yr^{-1}.

Table 3: Radium equivalent activity Ra_{eq} (Bq.kg^{-1}), external hazard index (H_{ex}), absorbed dose rate D (nGy.h^{-1}), and outdoor annual effective dose E (mSv yr^{-1}) of soil samples

Sample ID	Sampling Location		Radium equivalent activity Ra_{eq} (Bq.kg^{-1})	External hazard index (H_{eq})	Absorbed dose rate D (nGy.h^{-1})	Outdoor annual effective dose E (mSv yr^{-1})
	Longitude	Latitude				
Soil 01	89.03000 E	24.11444 N	174.90	0.47	82.23	0.10
Soil 02	89.02777 E	24.09388 N	188.00	0.51	87.17	0.11
Soil 03	89.03361 E	24.07555 N	196.69	0.53	91.97	0.11
Soil 04	89.03833 E	24.05222 N	180.55	0.49	83.77	0.10
Soil 05	89.04250 E	24.03166 N	196.48	0.53	91.93	0.11
Soil 06	89.01694 E	24.00916 N	188.84	0.51	87.90	0.11
Minimum			174.90	0.47	82.23	0.10
Maximum			196.69	0.53	91.97	0.11
Average			187.58	0.51	87.50	0.11
World Avg [1]			370	1	55	0.07

3.9 Radiological Hazard Assessment for Sediment Samples

Table 7 shows the radium equivalent activity Ra_{eq} (Bq.kg^{-1}), external hazard index (H_{ex}), absorbed dose rate D (nGy.h^{-1}), and outdoor annual effective dose E (mSv yr^{-1}) of sediment samples. The radium equivalent activity Ra_{eq} (Bq.kg^{-1}) were found to be varied from 106.12 Bq.kg^{-1} to 218.28 Bq.kg^{-1} with an average value of 144.69 Bq.kg^{-1}, which is lower than the worldwide average value 370.0 Bq.kg^{-1} [1]. The external hazard index (H_{ex}) was found to be varied from 0.29 to 0.59 with an average value of 0.39, which is also lower than the worldwide average value of 1.0. Absorbed dose rate D (nGy.h^{-1}) were found to be varied from 50.10 nGy.h^{-1} to 98.21 nGy.h^{-1}with an average value of 67.24 nGy.h^{-1}, which is slightly higher than the worldwide average value 55.0 nGy.h^{-1}. Outdoor annual effective dose E (mSv yr^{-1}) were found to be varied from 0.06 mSv yr^{-1} to 0.12 mSv yr^{-1} with an average value of 0.08 mSv yr^{-1}, which was higher than the worldwide average value 0.07 mSv yr^{-1}.

Table 4: Radium equivalent activity Ra_{eq} ($Bq.kg^{-1}$), external hazard index (H_{ex}), absorbed dose rate D ($nGy.h^{-1}$), and outdoor annual effective dose E ($mSv\ yr^{-1}$) of sediment samples

Sample ID	Sampling Location		Radium equivalent activity Ra_{eq} ($Bq.kg^{-1}$)	External hazard index (H_{eq})	Absorbed dose rate D ($nGy.h^{-1}$)	Outdoor annual effective dose E ($mSv\ yr^{-1}$)
	Longitude	Latitude				
Sediment 01	89.03000 E	24.11444 N	141.37	0.38	66.76	0.08
Sediment 02	89.02777 E	24.09388 N	218.28	0.59	98.21	0.12
Sediment 03	89.03361 E	24.07555 N	176.69	0.48	81.98	0.10
Sediment 04	89.03833 E	24.05222 N	119.10	0.32	55.30	0.07
Sediment 05	89.04250 E	24.03166 N	106.12	0.29	51.09	0.06
Sediment 06	89.01694 E	24.00916 N	106.58	0.29	50.10	0.06
Minimum			106.12	0.29	50.10	0.06
Maximum			218.28	0.59	98.21	0.12
Average			144.69	0.39	67.24	0.08
World Avg [1]			370.0	1.0	55.0	0.07

Fig. 6 shows the radiological hazard indices for soil and sediment samples. All the measured values were found below the world average values.

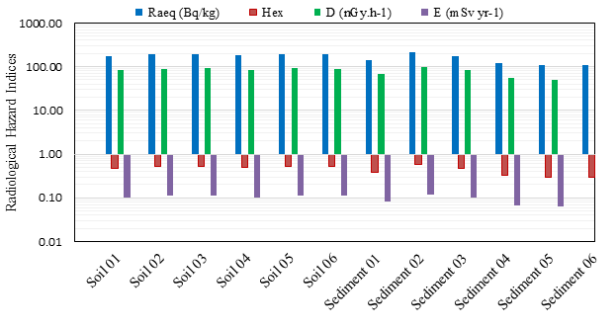

Fig. 7: Radiological hazard indices for soil and sediment samples.

4 Conclusion

The measurement showed that there were no artificially occurring radionuclides in the collected samples from the Padma River near ongoing nuclear power project in Rooppur, Pabna, Bangladesh. The calculated values of external hazard index (Hex) of all samples collected from the adjacent area of the Padma River are less than unity, which indicates that the radiological hazard is insignificant in that area. The research has another merit due to its site selection as there is a huge nuclear establishment is going to be constructed. So, the research outcomes can be used as a baseline data of the area and reference for most extensive studies of the subject in future.

5. References

[1] U. Nations Scientific Committee on the Effects of Atomic Radiation, SOURCES AND EFFECTS OF IONIZING RADIATION United Nations Scientific Committee on the Effects of Atomic Radiation, UNSCEAR 2000 Report to the General Assembly, with Scientific Annexes, I.

[2] F. B. Masok, P. L. Masiteng, R. D. Mavunda, P. P. Maleka, and H. Winkler, Measurement of radioactivity concentration in soil samples around phosphate rock storage facility in Richards Bay, South Africa, J. Radiat. Res. Appl. Sci., 11(1), 29-36 (2018).

[3] A. F. M. M. Rahman *et al.*, Assessment of Radiological Dose around a 3-MW TRIGA Mark-II Research Reactor, Int. Lett. Chem. Phys. Astron., 15(2), 183-200 (2013).

[4] A. H. Taqi, L. A. A. Al-Ani, and A. M. Ali, Assessment of the natural radioactivity levels in Kirkuk oil field, J. Radiat. Res. Appl. Sci., 9(3), 337-344 (2016).

[5] C. E. Roessler, Z. A. Smith, W. E. Bolch, and R. J. Prince, Uranium and radium-226 in Florida phosphate materials, Health Phys., 37(3), 269-277 (1979).

[6] M. A. M. Uosif and A. El-taher, Radiological assessment of Abu-Tartur phosphate, Western Desert Egypt, Radiat. Prot. Dosimetry, 130(2), 228-235 (2008).

[7] A. Nahar, K. Asaduzzaman, M. M. Islam, M. M. Rahman, and M. Begum, Assessment of natural radioactivity in rice and their associated population dose estimation, https://doi.org/10.1080/10420150.2018.1542696, 173 (11-12), 1105-1114 (2018).

[8] K. Asaduzzaman *et al.*, Assessment of Natural Radioactivity Levels and Potential Radiological Risks of Common Building Materials Used in Bangladeshi Dwellings, PLoS One, 10 (10), (2015).

[9] M. U. Khandaker *et al.*, Radiation dose to the Malaysian populace via the consumption of bottled mineral water, Radiat. Phys. Chem., 140, 173-179 (2017).

[10] M. U. Khandaker *et al.*, Evaluation of radionuclides transfer from soil-to-edible flora and estimation of radiological dose to the Malaysian populace, Chemosphere, 154, 528–536 (2016).

[11] M. U. Khandaker, P. J. Jojo, H. A. Kassim, and Y. M. Amin, Radiometric analysis of construction materials using HPGe gamma-ray spectrometry, *Radiat.* Prot. Dosimetry, 152(1–3), 33-37 (2012).

[12] K. A. Kabir, S. M. A. Islam, and M. M. Rahman, Distribution of Radionuclides in Surface Soil and Bottom Sediment in the District of Jessore, Bangladesh and Evaluation of Radiation Hazard, J. Bangladesh Acad. Sci., 33(1), 117-130 (2009).

[13] K. Debertin and R. G. Helmer, "Gamma- and x-ray spectrometry with semiconductor detectors," p. 399, 1988.

[14] J. Beretka and P. J. Mathew, Natural radioactivity of Australian building materials, industrial wastes and by-products, Health Phys., 48(1), 87-95 (1985).

[15] L. Xinwei and Z. Xiaolan, Measurement of natural radioactivity in sand samples collected from the Baoji Weihe Sands Park, China, Environ. Geol. 2006 507, 50(7), 977-982 (2006).

[16] M. T. Kolo, M. U. Khandaker, and H. K. Shuaibu, Natural radioactivity in soils around mega coal-fired cement factory in Nigeria and its implications on human health and environment, Arab. J. Geosci. 2019 1215, 12(15), 1-11 (2019).

[17] F. B. Masok, P. L. Masiteng, R. D. Mavunda, P. P. Maleka, and H. Winkler, Measurement of radioactivity concentration in soil samples around phosphate rock storage facility in Richards Bay, South Africa, J. Radiat. Res. Appl. Sci., 11(1), 29-36 (2018).

[18] A. Miah, M. M. H. Miah, M. Kamal, M. I. Chowdhury, and M. Rahmatullah, Natural Radioactivity and Associated Dose Rates in Soil Samples of Malnichera Tea Garden in Sylhet District of Bangladesh, J. Nucl. Part. Phys., 2(6), 147-152 (2013).

[19] N. K. Mohammed and M. S. Mazunga, Natural radioactivity in soil and water from likuyu village in the neighborhood of Mkuju uranium deposit, Int. J. Anal. Chem., (2013).

[20] Amanjeet, A. Kumar, S. Kumar, J. Singh, P. Singh, and B. S. Bajwa, Assessment of natural radioactivity levels and associated dose rates in soil samples from historical city Panipat, India, J. Radiat. Res. Appl. Sci., 10(3), 283-288 (2017).

[21] S. Yasmin *et al.*, The presence of radioactive materials in soil, sand and sediment samples of Potenga sea beach area, Chittagong, Bangladesh: Geological characteristics and environmental implication, Results Phys., 8, 1268-1274 (2018).

[22] J. Ferdous, A. Begum, and A. Islam, Radioactivity of soil at proposed Rooppur Nuclear Power Plant site in Bangladesh, Int. J. Radiat. Res., 13(2), 135-142 (2015).

[23] M. A. Haydar *et al.*, The status of NORMs in natural environment adjacent to the Rooppur nuclear power plant of Bangladesh, Nucl. Eng. Technol., 53(12), 4114-4121 (2021).

[24] G. Apaydin *et al.*, Assessment of natural radioactivity and radiological risk of sediment samples in Karacaören II dam Lake, Isparta/Turkey, 28-35 (2019).

[25] V. Ramasamy, G. Suresh, V. Meenakshisundaram, and V. Ponnusamy, Horizontal and vertical characterization of radionuclides and minerals in river sediments, Appl. Radiat. Isot., 69(1), 184-195 (2011).

[26] K. Nazmus Sakib, Determination of Natural and Artificial Radionuclides in Water Samples of Habigonj District, Bangladesh, 40, (2015).

[27] A. S. MOLLAH and S. R. CHAKRABORTY, Radioactivity and Radiation Levels in and around the Proposed Nuclear Power Plant Site at Rooppur, Japanese J. Heal. Phys., 44(4), 408-413 (2009).

[28] M. A. Samad *et al.*, A Study on the Radioactivity Level in Raw Materials, Final Products and Wastes of the Phosphate Fertilizer Industries in Bangladesh, J. Environ. Prot. (Irvine,. Calif)., 3(10), 1393-1402 (2012).

[29] D. O. Kpeglo *et al.*, Radiological exposure assessment from soil, underground and surface water in communities along the coast of a shallow water offshore oilfield in Ghana, Radiat. Prot. Dosimetry, 163(3), 341-352 (2015).

[30] E. O. Agbalagba and R. A. Onoja, Evaluation of natural radioactivity in soil, sediment and water samples of Niger Delta (Biseni) flood plain lakes, Nigeria, J. Environ. Radioact., 102(7), 667-671 (2011).

[31] K. Khan, P. Akhter, S. D. Orfi, G. M. Malik, and M. Tufail, Natural radioactivity levels in river, stream and drinking water of the northwestern areas of Pakistan, J. Radioanal. Nucl. Chem. 2003 2562, 256(2), 289-292 (2003).

[32] A. S. Alaboodi, N. A. Kadhim, A. A. Abojassim, and A. Baqir Hassan, Radiological hazards due to natural radioactivity and radon concentrations in water samples at Al-Hurrah city, Iraq, Int. J. Radiat. Res., 18(1), 1-11 (2020).

Risk Stratification of Thyroid Nodules Based on ACR-TIRADS on Ultrasound

S.M.N. Uddin[1], J. Das[2], A. Pervin[1], M.N. Nowsher[3], M. Kamruzzaman[4] and A.K. Paul[5]

[1.]*Medical officer, Institute of Nuclear Medicine and Allied Sciences, Khulna.*
[2.]*Director and Assoc. Prof, Institute of Nuclear Medicine and Allied Sciences, Khulna.*
[3.]*Asst. Prof, Department of Pathology, Khulna Medical College*
[4]*Former head of dept. and Prof., Otolaryngology, Khulna Medical College Hospital.*
[5.]*Former Chairman and Prof, Bangladesh Atomic Energy Commission.*

Abstract

The role of ACR-TIRADS on differentiating benign and malignant thyroid nodules is evolving since 2017. The aim of this study was to find out the risk of malignancy in different TIRADS score. This prospective study was conducted in INMAS, Khulna with 93 patients from January 2021 to December 2021. Based on composition, echogenicity, shape, margin and echogenic foci, nodules were categorized TR1(0), TR2(2), TR3(3), TR4(4-6), TR5(≥7). FNAC or histopathology were done according to clinician's findings and compared with TIRADS scoring. Risk of malignancy was assessed by positive predictive value under bivariate analysis. Among 93 cases, risk of malignancy was 0% in TR1and TR2, 39% in TR3, 88% in TR4 and 100% in TR5 nodules. Solid composition (77%), hypoechoic or very hypoechoic echogenicity (87%) and punctate echogenic foci(100%) were the most common malignant features. In TR3 group we found wide range of variation among which 54% were Adenomatous goiter, 4% were Hurthle cell adenoma, 4% were Follicular adenoma, 32% were Papillary thyroid carcinoma (PTC), 3% were Follicular carcinoma and 3% were Medullary carcinoma. Among TR3, 33% malignant nodules and among TR4, 50% malignant nodules were below the size of FNA recommendation. ACR-TIRADS is an excellent indicator for evaluating the cancer risk of thyroid nodules, determining further management and reducing unnecessary biopsies.

Keywords: American College of Radiology Thyroid Imaging Reporting and Data System (ACR TI-RADS), thyroid nodules, malignancy.

Introduction

Thyroid nodule is defined as a region of parenchyma sonographically distinct from the remainder of the thyroidtissue (1). The prevalence of thyroid nodule is high, about one third of the adult population (33-68%) has thyroid nodule detected on high resolution ultrasound (HRUS) (2). Most of these nodules are benign, however less than 10% are malignant (3).

HRUS is the most important diagnostic tool for detecting thyroid nodules (2). Thyroid Imaging Reporting and Data System (TIRADS) introduced by The American College of Radiology (ACR), is an ultrasound based risk stratification system for thyroid nodules. The TIRADS classification is point scale that categorizes the HRUS of thyroid nodules from low to high suspicion based on the number and combination of the predictors of the malignancy (4). In ACR TI-RADS the nodules are evaluated in five sonographic categories: composition, echogenicity, shape, margin and echogenic foci. When assessing a nodule, one feature from each of the first four categories and all the features that apply from the final category are selected. The points are summed to place the nodule in one of five ascending risk level: TR1 to TR5.The nodules having higher risk levels have lower size thresholds for FNA and follow-up with ultrasound (5).Unlike other risk stratification system, ACR-TIRADS provides unambiguous management recommendation (Biopsy, follow-up, no action) for all thyroid nodules. It reduces the number of unnecessary biopsies by 19.9% to 46.5% compared with other RSSs (6, 10). The objective of our study was to determine the efficacy of ACR-TIRADS in estimating the risk of malignancy in thyroid nodules.

*Corresponding author: smnazimuddin.nu@gmail.com

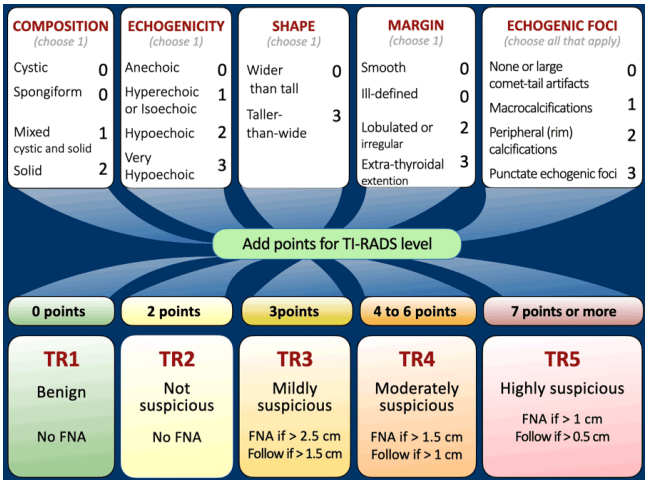

Fig 1: Chart showing five categories on the basis of the ACR Thyroid Imaging, Reporting and Data System (TI-RADS) lexicon, TR levels, and criteria for fine-needle aspiration or follow-up ultrasound (5).

Patients and Method

This was a prospective study conducted in Institute of Nuclear Medicine and Allied Sciences, Khulna from January 2021 to December 2021. The study population was 93, who presented with neck swelling and had one or more than one nodule in thyroid with/without lymph node involvements. All nodules were scanned by EsoateMyLab8 machine with a high frequency linear transducer (4-14 MHz) and classified into five categories on their accumulated points from TR1 toTR5 according to ACR-TIRADS.All these 93 cases went through FNA/histopathology and the finding were compared with HRUS findings.

COMPOSITION	ECHOGENICITY	SHAPE	MARGIN	ECHOGENIC FOCI
Spongiform: Composed predominantly (>50%) of small cystic spaces. Do not add further points for other categories. *Mixed cystic and solid:* Assign points for predominant solid component. Assign 2 points if composition cannot be determined because of calcification.	*Anechoic:* Applies to cystic or almost completely cystic nodules. *Hyperechoic/isoechoic/hypoechoic:* Compared to adjacent parenchyma. *Very hypoechoic:* More hypoechoic than strap muscles. Assign 1 point if echogenicity cannot be determined.	*Taller-than-wide:* Should be assessed on a transverse image with measurements parallel to sound beam for height and perpendicular to sound beam for width. This can usually be assessed by visual inspection.	*Lobulated:* Protrusions into adjacent tissue. *Irregular:* Jagged, spiculated, or sharp angles. *Extrathyroidal extension:* Obvious invasion = malignancy. Assign 0 points if margin cannot be determined.	*Large comet-tail artifacts:* V-shaped, >1 mm, in cystic components. *Macrocalcifications:* Cause acoustic shadowing. *Peripheral:* Complete or incomplete along margin. *Punctate echogenic foci:* May have small comet-tail artifacts.

*Refer to discussion of papillary microcarcinomas for 5-9 mm TR5 nodules.

Fig 2: Explanatory notes for describing the thyroid nodules. (5)

The descriptive analysis in this study comprised frequencies accompanied by percentage. Bivariate analysis employed chi-square test to identify significant associations between histopathology/FNA and the explanatory variables, with a predetermined significance level of 5% for a two-tailed p-value within a 95% confidence interval. The present study used software SPSS V25 for data analysis.

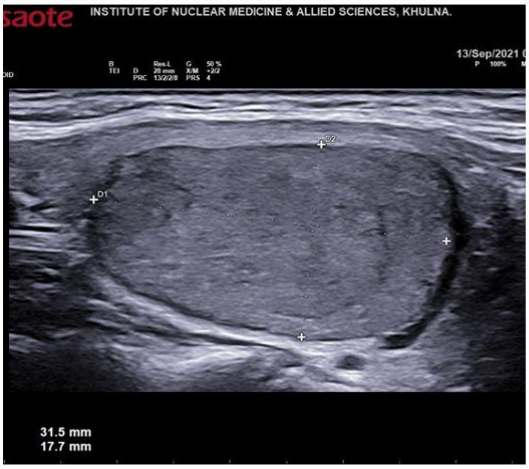

Composition: Solid - 2
Echogenicity: Isoechoic - 1
Shape: Wider-than-tall - 0
Margin: Smooth - 0
Echogenic foci: None - 0
Size: 3.1s cm
Total points: 3
ACR TI-RADS: TR3

Histopathology:
Follicular Adenoma

Fig 3: A

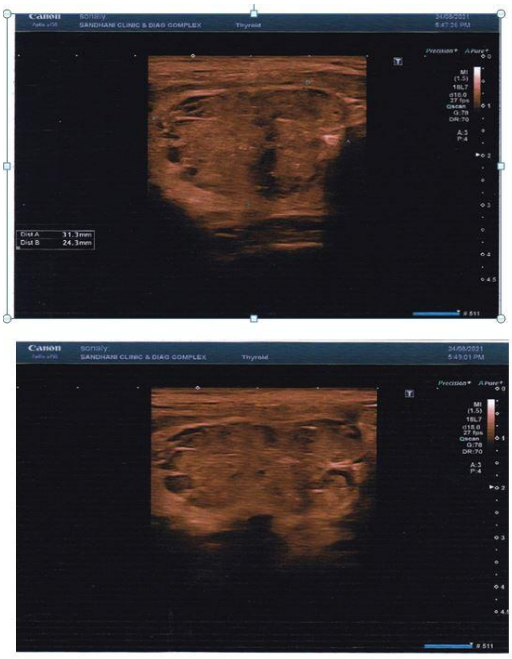

Composition: Solid - 2
Echogenicity: Hypoechoic - 2
Shape: Wider-than-tall - 0
Margin: Irregular- 2
Echogenic foci: None- 0
Size: 3.1 cm
Total points: 6
ACR TI-RADS: TR4

FNAC:
Consistent with papillary carcinoma

Histopathology:
Papillary carcinoma

Fig 3: B

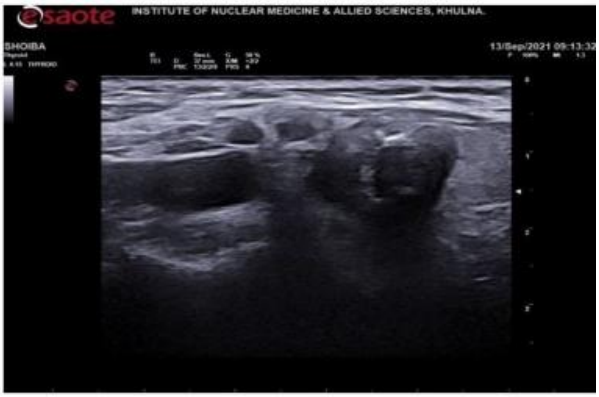

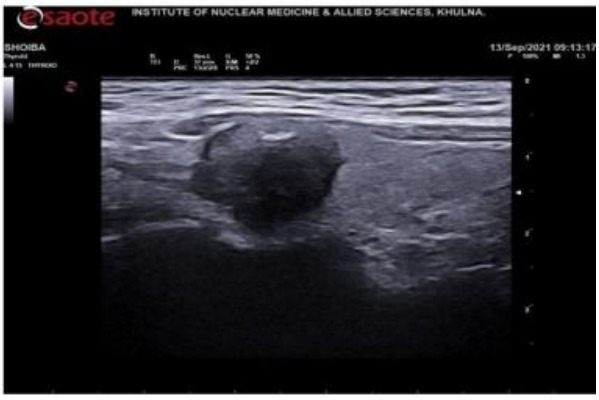

Composition: Solid – 2
Echogenicity: Hypoechoic – 2
Shape: Wider than taller – 0
Margin: Smooth – 0
Echogenic Foci:
Macrocalcification – 1
Size: 1.8cm
Total points: 5
ACR TIRADS: TR4
FNAC:
Lymphocytic Thyroiditis
Review FNAC:
Cellular follicular lesion-follicular variant of Papillary thyroid Carcinoma.
Histopathology:
Papillary carcinoma

Fig 3: C

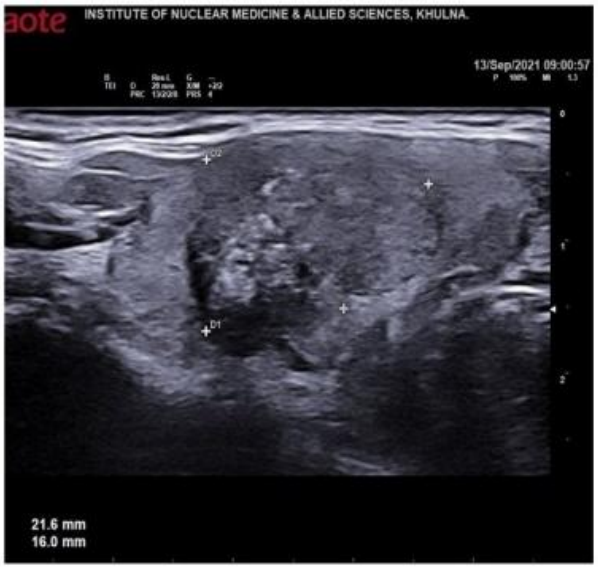

Composition: Solid - 2
Echogenicity: Hypoechoic - 2
Shape: Wider-than-tall - 0
Margin: Lobulated - 2
Echogenic foci: Punctate Echogenic foci - 3
Size: 2.1 cm
Total points: 9
ACR TI-RADS: TR5

FNAC:
Medullary carcinoma

Fig 3: D

Fig 3: A, B, C, D showing some nodules with their point distribution and TIRADS level according to ACR TIRADS along with their histopathology findings.

Result

Among 93 patients, 80 patients (86%) were female and 13 patients (14%) were male with their age ranged from 25 years to 45 years. The majority of the nodules (66 cases, 71%) were malignant and 27 cases (29%) had benign nodules. Among 27 benign nodules, 7 nodules were ACR-TIRADS 1 and 2, 17 nodules were TR3 and 3 nodules were TR4.

Table 1: Ultrasound findings with risk of malignancy

Characteristics	Histopathology/FNA			Risk of malignancy (%)	p-value
	Benign	Malignant	Total		
Total	27	66	93		
Composition					0.002
Cystic or almost entirely cystic	0	0	0		
Spongiform	0	0	0		
Mixed solid and cystic	8	3	11	27.27	
Solid or almost entirely solid	19	63	82	76.83	
Echogenicity					<0.001
Hyperechoice	1	2	3	66.67	
Isoechoice	19	16	35	45.71	
Hypoechoice	7	48	55	87.27	
Very hypoechoice	0	0	0		
Shape					0.176
Wider than tall	27	60	87	68.97	
Taller than wide	0	6	6	100.00	
Margin					0.021
Ill defined	16	20	36	55.56	
Smooth	11	35	46	76.08	
Lobulated or irregular	0	9	9	100.00	
Extra thyroidal extension	0	2	2	100.00	
Echogenic foci					<0.001
None	26	39	65	60.00	
Macrocalcifications	1	5	6	83.33	
Peripheral calcifications	0	0	0		
Punctate echogenic foci	0	22	22	100.00	
ACR-TIRADS					<0.001
TR1	0	0	0		
TR2	7	0	7	0.00	
TR3	17	11	28	39.29	
TR4	3	23	26	88.46	
TR5	0	32	32	100.00	

On nodule composition, 11 nodules were mixed cystic-solid and 82 nodules were solid or almost entirely solid. Among mixed cystic-solid nodules, 27.3% and among solid nodules 76.8% were malignant. P value is 0.002, which determines solid composition as an indicator for increased risk of malignancy statistically.

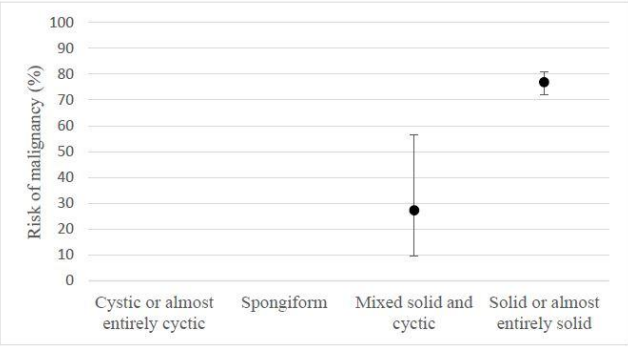

Graph 1: Risk of malignancy according to nodule composition

Regarding echogenicity, risk of malignancy was 45.7% in isoechoic nodules and 87.3% in case of hypoechoic nodules. So, hypoechoic echogenicity is a significant risk factor for malignancy (P-value: 0.001).

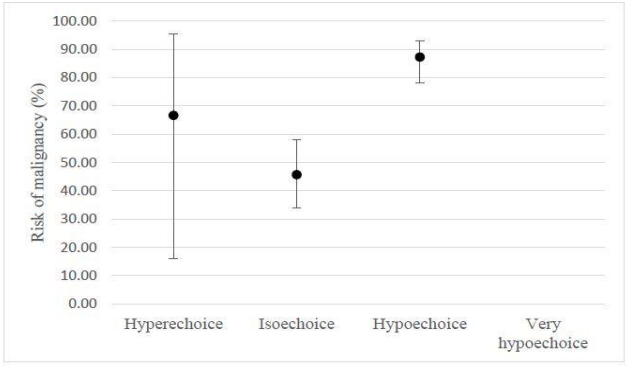

Graph 2: Risk of malignancy according to echogenicity of nodules

About shape, Taller than wider nodule showed high risk of malignancy (100%), whereas wider than taller nodule showed 68.97% risk of malignancy. As for nodular margin study, Lobulated or irregular margin and extrathyriodal extension had very high cancer risk (100%).

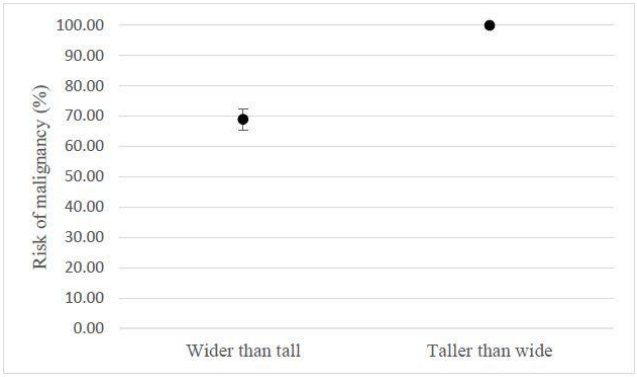

Graph 3: Risk of malignancy according to shape of nodules

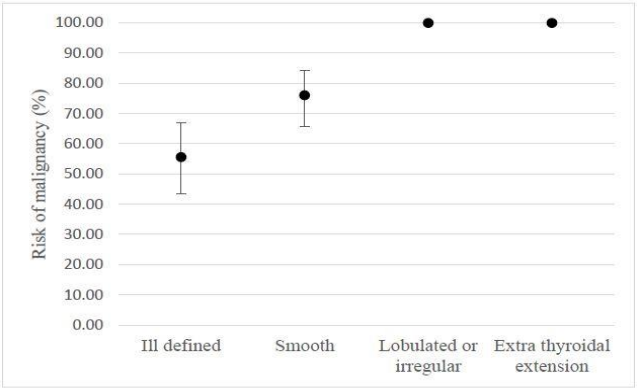

Graph 4: Risk of malignancy according to margin of nodules

In term of echogenic foci, punctate echogenic foci had a higher malignancy risk (100%) with statistically significant difference (P<0.001), compared with macrocalcification and peripheral calcification.

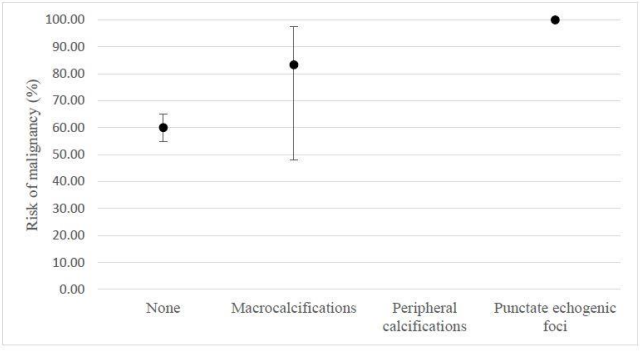

Graph 5: Risk of malignancy according to presence of echogenic foci in nodules

In this study, there were no risk of malignancy (0.00%) of thyroid nodules in TR1 and TR2. Among 28 TR3 nodules, 11 cases were malignant, which showed about 39.3% risks of malignancies. TR3 nodules showed most heterogenous distribution of pathology, among which 15 nodules were benign, 1 nodule was hurthle cell adenoma, 1 was follicular adenoma, 9 cases were papillary carcinoma and 1 case was follicular carcinoma. Among TR4 nodules, 23 nodules were malignant, which showed about 88.46% risk of malignancy. In this study, most of the nodules (32cases) were ACR-TIRADS 5, where the risk of malignancy was 100% with statistically significant difference (P<0.001).

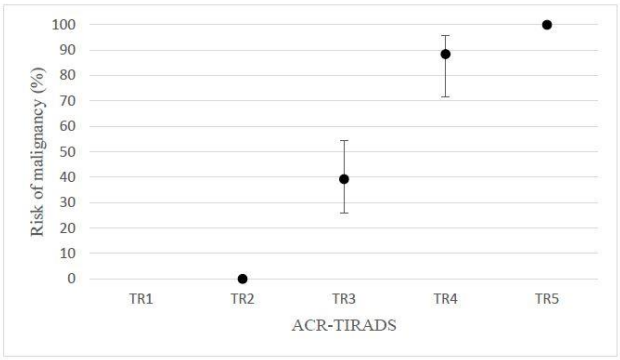

Graph 6: Risk of malignancy with respect to ACR TIRADS level (TR1-TR5) of nodules

Table 2: Heterogenous distribution of pathology in TR3 nodules

	Histopathology/FNA						Total
	Hurthle cell adenoma	NG	Follicular adenoma	PC	Medullary carcinoma of thyroid	Follicular carcinoma	
TR3	1	15	1	9	1	1	28

Discussion

High-resolution ultrasound often detects thyroid nodules in upto 70% of adults (2).Our study showed an increased risk of malignancy with higher TIRADS score as described in ACR-TIRADS lexicon. Therefore, this study aims to assess the risk of malignancy in thyroid nodule based on ultrasound based ACR-TIRADS by comparing it with the pathological results from the FNA/Biopsy.

Solid composition (88%) with hypoechoic echogenicity (59%), were the most abundant group in our study with 77% and 87% risk of malignancy respectively. Similar study was done by Mohanty J et al, who showed 66% were solid nodules with 36% risk of malignancy among which hypoechoic and very hypoechoic showed 47% and 100% risk of malignancy respectively (8). On similar study, Middleton et al reported risk of malignancy was 12% in solid hypoechoic and 47% in solid very hypoechoic nodules. In our study we had 46% risk of malignancy in isoechoic nodules, whereas Mohanty J et al and Middleton et al showed 11% and 9% risk of malignancy (8, 9). As a referral center for management of differentiated thyroid carcinoma, no cystic or spongiform nodules were included in our study group.

Most of the nodules were wider than taller (87 Cases, 93.5%) with 69% risk of malignancy (60 Cases). Only 6 nodules (6.5%) were taller than wider in our study and all of them were malignant with 100% risk of malignancies. On similar study, Mohanty et al showed 21% risk of malignancy in wider than taller nodules and 66.6% risk of malignancy in taller than wider nodules (8). As most of the malignant nodules were wider than taller in shape, which may be the cause of high malignancy risk in this group. At the time the nodules were analyzed, the potential significance of the taller-than-wide shape was not well established, and this feature was not evaluated by the study of Middleton et al (9).

In this study, only 9.7% nodules had lobulated or irregular margin and 2.2% nodule had extrathyroidal extension. Both these features had 100% risk of malignancy in our study, whereas Mohanty J et al reported, risk of malignancy was 38% in lobulated or irregular margin and 100% in nodules with extrathyroidal extension (8). In his study, Middleton et al mentioned solid smooth nodules had a risk of malignancy of 12.9%, and solid lobulated or irregular nodules had a risk level of 44.7%. The increased risk of malignancy for lobulated or irregular margins also occurred with mixed solid and cystic nodules (9). Tessler et al, in his white paper of ACR-TIRADS mentioned nodules with extrathyroidal extension are always malignant until proven otherwise and we had the same findings (5).

Among all scoring features of ACR-TIRADS, echogenic foci are the most important ones. In this study 7% nodules had macrocalcification with 83% risk of malignancy and 24% nodules had punctate echogenic foci with 100% risk of malignancy. In our study population there was no nodule with peripheral rim calcification. In similar study Middleton et al showed the risk of malignancy associated with macrocalcification, peripheral calcification and punctate echogenic foci in solid nodule was 11.9%, 26.1% and 35.4% respectively (9), whereas Mohanty j et al reported 14% in macrocalcification and 50% in both peripheral calcification and punctate echogenic foci (8).

Size of the nodule is also important, as ACR-TIRADS recommends FNA of a nodule according to the size of the nodules and also related to prognosis (9). ACR-TIRADS does not recommend FNA of a nodule under 1.0cm, whereas in our study we found a TR4 malignant nodule which was less than 1.0cm in highest transverse diameter. Similarly, FNA is not recommended for TR3 nodule below 2.5cm, where in our study we got one. So, this FNA recommendation according to size can become a pitfall of ACR-TIRADS according to our study.

In this study, among 93 nodules, 7 nodules were TR2, 28 were TR3, 26 were TR4 and 32 were TR5. All TR2 nodules were benign, whereas 11 TR3, 23 TR4 and all TR5 nodules were malignant. So, the aggregated risk of malignancy for TR3, TR4 and TR5 nodules were 39.29%, 88.46% and 100% respectively, where Middleton et al showed 0.3%, 1.5%, 4.8%, 9.1%and 35.0% aggregated risk level for TR1, TR2, TR3, TR4 and TR5 nodules respectively (9). In white paper of ACR TIRADS by Tessler et al, the risk was <2% for TR1 and TR2, 2-5% for TR3, 5-20% for TR4 and >20% for TR5 nodules (5), where Mohanty J et al reported 0% for TR1, TR2, TR3, 30% for TR4 and 56% risk of malignancy for TR5 nodules (8). As previously mentioned, this study was performed in a referral center for management of differentiated thyroid carcinoma with a small study population in a single institute and most of the nodules included weremalignant, which may have increased the risk of malignancy for different categories in our study.

Conclusion

In this study, ACR TIRADS acts as an excellent diagnostic tool for differentiating benign and malignant thyroid nodules. The risk of malignancy is high with higher TIRADS level especially for TR4 and TR5 nodules.Size threshold for FNA in ACR TI-RADS should be reconsidered, as in this study we found several malignant nodules with below threshold size for FNAC according to their TIRADS level.

References

1. Cooper, D.S., Doherty, G.M., Haugen, B.R., Kloos, R.T., Lee, S.L., Mandel, S.J., Mazzaferri, E.L., McIver, B., Pacini, F., Schlumberger, M. and Sherman, S.I., 2009. Revised American Thyroid Association management guidelines for patients with thyroid nodules and differentiated thyroid cancer: the American Thyroid Association (ATA) guidelines taskforce on thyroid nodules and differentiated thyroid cancer. *Thyroid*, *19*(11), pp.1167-1214.https://doi.org/10.1089/thy.2009.0110
2. Guth, S., Theune, U., Aberle, J., Galach, A. and Bamberger, C.M., 2009. Very high prevalence of thyroid nodules detected by high frequency (13 MHz) ultrasound examination. *European journal of clinical investigation*, *39*(8), pp.699-706.https://doi.org/10.1111/j.1365-2362.2009.02162.x
3. Papini, E., Guglielmi, R., Bianchini, A., Crescenzi, A., Taccogna, S., Nardi, F., Panunzi, C., Rinaldi, R., Toscano, V. and Pacella, C.M., 2002. Risk of malignancy in nonpalpable thyroid nodul8es: predictive value of ultrasound and color-Doppler features. *The Journal of Clinical Endocrinology & Metabolism*, *87*(5), pp.1941-1946.https://doi.org/10.1210/jcem.87.5.8504
4. Horvath, E., Majlis, S., Rossi, R., Franco, C., Niedmann, J.P., Castro, A. and Dominguez, M., 2009. An ultrasonogram reporting system for thyroid nodules stratifying cancer risk for clinical management. *The Journal of Clinical Endocrinology & Metabolism*, *94*(5), pp.1748-1751.https://doi.org/10.1210/jc.2008-1724
5. Tessler, F.N., Middleton, W.D., Grant, E.G., Hoang, J.K., Berland, L.L., Teefey, S.A., Cronan, J.J., Beland, M.D., Desser, T.S., Frates, M.C. and Hammers, L.W., 2017. ACR thyroid imaging, reporting and data system (TI-RADS): white paper of the ACR TI-RADS committee. *Journal of the American college of radiology*, *14*(5), pp.587-595.https://doi.org/10.1016/j.jacr.2017.01.046
6. Hoang, J.K., Middleton, W.D. and Tessler, F.N., 2021. Update on ACR TI-RADS: successes, challenges, and future directions, from the AJR special series on radiology reporting and data systems. *American Journal of Roentgenology*, *216*(3), pp.570-578.https://doi.org/10.2214/AJR.20.24608
7. Chainamnan, W., 2023. Accuracy of ACR-TIRADS in assessment and diagnosis of thyroid nodules in patients underwent thyroid surgery in Taksin Hospital. Chulalongkorn Medical Journal, 67(3).DOI : 10.14456/clmj.2023.25.

8. Mohanty, J. and Mishra, P., 2019. Role of ACR-TIRADS in risk stratification of thyroid nodules.http://dx.doi.org/10.18203/2320-6012.ijrms20191076.

9. Middleton, W.D., Teefey, S.A., Reading, C.C., Langer, J.E., Beland, M.D., Szabunio, M.M. and Desser, T.S., 2017. Multiinstitutional analysis of thyroid nodule risk stratification using the American College of Radiology Thyroid Imaging Reporting and Data System. *American Journal of Roentgenology*, *208*(6), pp.1331-1341.https://doi.org/10.2214/AJR.16.17613

10. Grani, G., Lamartina, L., Ascoli, V., Bosco, D., Biffoni, M., Giacomelli, L., Maranghi, M., Falcone, R., Ramundo, V., Cantisani, V. and Filetti, S., 2019. Reducing the number of unnecessary thyroid biopsies while improving diagnostic accuracy: toward the "right" TIRADS. *The Journal of Clinical Endocrinology & Metabolism*, *104*(1), pp.95-102.https://doi.org/10.1210/jc.2018-01674

11. Leoncini, A., Curti, M., Ruinelli, L. and Trimboli, P., 2024. Meaning of ACR-TIRADS recommendation in favor of follow-up rather than FNAC in thyroid nodules. *Updates in Surgery*, pp.1-6https://doi.org/10.1007/s13304-024-01886-4.

Diagnostic Pitfalls in Pediatric Ultrasound: Mesenteric Cyst Mimicking Ovarian Pathology

F.T. Zohra[1], P. Podder[1], M.S. Khan[2], I. Ashrafi[2], R.A. Sharmin[3] and T. Sultana[4]

[1.] *Senior Medical Officer, Institute of Nuclear Medical Physics (INMP), AERE, Savar, Dhaka*
[2.] *Consultant, Ibn Sina Medical College & Hospital, Kollayanpur, Dhaka*
[3.] *Senior Medical Officer, Institute of Nuclear Medicine and Allied Sciences (INMAS), Mohakhali, Dhaka.*
[4.] *Senior Medical Officer, Institute of Nuclear Medicine and Allied Sciences (INMAS), Dhaka.*

Abstract

Mesenteric cysts are rare intra-abdominal lesions in pediatric patients and are often misdiagnosed due to non-specific clinical and imaging findings. Their ultrasonographic features may closely mimic adnexal pathologies such as hemorrhagic ovarian cysts or ovarian torsion, especially in female children presenting with acute lower abdominal pain. A 7-year-old girl presented with acute right lower abdominal pain. Transabdominal ultrasonography showed a cystic lesion with septations, echogenic internal materials suggestive of clots, and peripheral vascularity without internal flow. Findings were suspicious of a hemorrhagic ovarian cyst with possible torsion. However, surgical exploration revealed an infected mesenteric cyst originating from the lesser omentum and involving the terminal ileum, cecum, and appendix tip. Histopathology confirmed the diagnosis. This case highlights the diagnostic dilemma posed by mesenteric cysts in children, especially when their imaging features overlap with more common adnexal pathologies. Surgical exploration and histopathological analysis remain essential for definitive diagnosis in uncertain cases.

Keywords: Mesenteric cyst, Hemorrhagic ovarian cyst, Pediatric ultrasonography, Abdominal pain, Diagnostic dilemma

Introduction

Mesenteric cysts are uncommon intra-abdominal lesions, with an estimated incidence of approximately 1 per 100,000 pediatric hospital admissions [1]. They may arise anywhere along the mesentery of the gastrointestinal tract or the omentum, depending on their embryological origin, and are classified into lymphatic, mesothelial, enteric, urogenital, dermoid, or pseudocyst types. Occurrence in the lesser omentum is exceptionally rare, with only a handful of pediatric cases reported in the literature [2]. Most mesenteric cysts are benign, but complications can occur from infection, hemorrhage, rupture, volvulus, or obstruction, particularly in larger or inflamed cysts [3, 4].

In pediatric female patients, acute lower abdominal pain is frequently attributed to gynecologic or appendiceal etiologies, such as ovarian torsion, hemorrhagic ovarian cysts, or acute appendicitis. These are more commonly encountered in emergency settings and tend to bias the initial clinical impression [5]. Ultrasonography remains the first-line diagnostic modality due to its accessibility, lack of ionizing radiation, and ability to evaluate pelvic and abdominal structures [6]. However, when ovarian anatomy is obscured or distorted, ultrasonographic features of mesenteric cysts may overlap with adnexal pathologies, especially in the presence of hemorrhagic components or inflammatory changes [7, 8]. This diagnostic overlap can lead to unnecessary gynecologic interventions or delayed diagnosis of extra-ovarian conditions.

The case discusses a young girl with right iliac fossa pain, which initially appeared to be a hemorrhagic ovarian cyst but was later determined to be an infected mesenteric cyst from the lesser omentum. This case highlights the necessity of considering mesenteric cysts in the differential diagnosis of cystic pelvic masses in pediatric patients, especially with atypical or inconclusive imaging findings.

Case Summary

A 7-year-old girl with no significant medical history experienced sudden right lower abdominal pain for two days. She exhibited no vomiting, fever, or urinary symptoms. Examination revealed she was afebrile and hemodynamically stable, with localized tenderness and mild guarding in the right iliac fossa, but no palpable mass was found.

Transabdominal ultrasonography revealed a unilocular cystic lesion in the right iliac fossa, measuring about 5.1 × 3.5 cm, characterized by internal reticular septations, hyperechoic clots, posterior acoustic enhancement, and peripheral wall vascularity without internal flow. The right ovary was obscured, suggesting a hemorrhagic ovarian cyst possibly complicated by torsion, supported by acute pain and the lesion's adnexal positioning.

Due to diagnostic uncertainty and the possibility of adnexal torsion, a laparotomy was performed. Intraoperatively, a unilocular cystic mass arising from the lesser omentum was identified. The cyst was adherent to the terminal ileum and cecum, and notably, the tip of the appendix was found invaginated into the cyst wall. Both ovaries and fallopian tubes appeared anatomically normal. The cyst contained clear serous fluid and was completely excised along with the inflamed appendiceal tip, while preserving the base of the appendix.

Histopathological examination revealed a fibrous-walled cyst lined by flattened epithelium with infiltration of chronic inflammatory cells, consistent with an infected mesenteric cyst. There was no evidence of malignancy or ovarian tissue.

*Corresponding author: shetu0000@gmail.com

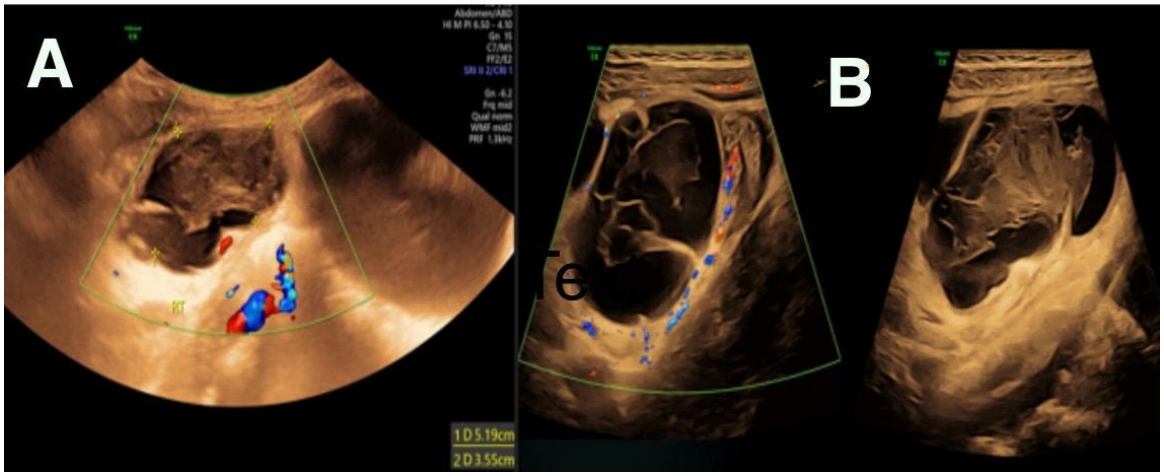

Fig. 1: Transabdominal ultrasound image of a 7-year-old girl, showing a well-defined, unilocular cystic lesion in the right iliac fossa (A). The lesion demonstrates internal reticular septations, hyperechoic retracted clots with concave borders, posterior acoustic enhancement, and peripheralwall vascularity on color Doppler (B).

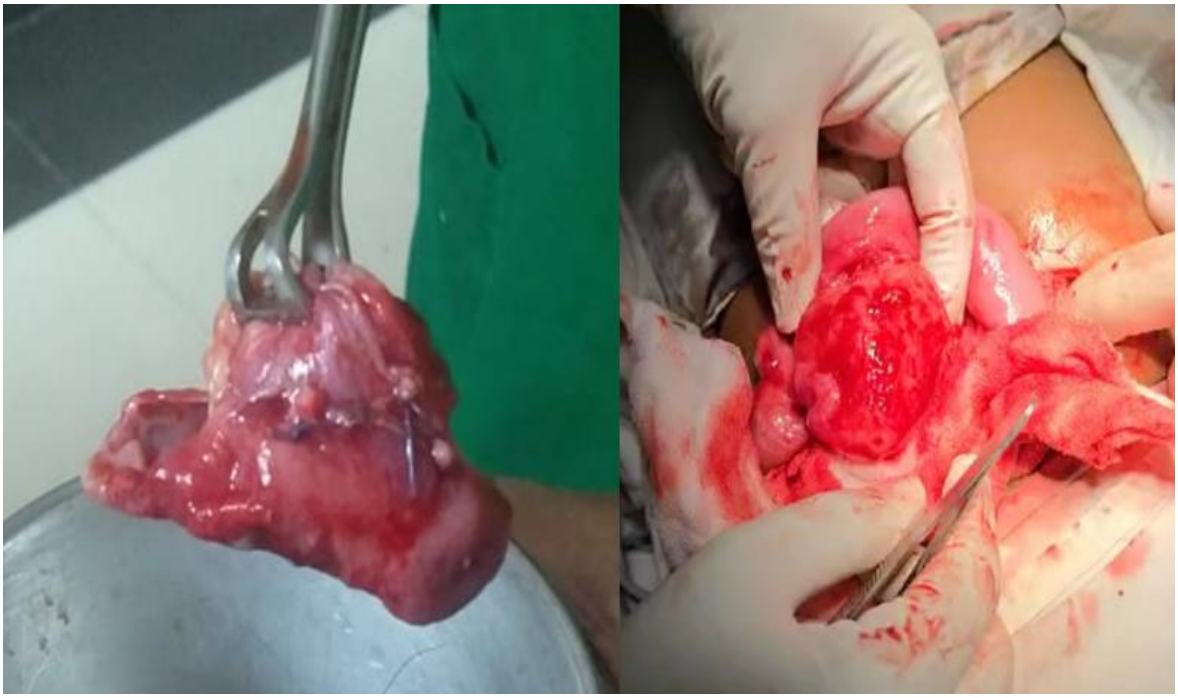

Fig. 2: Intraoperative image showing a unilocular cystic mass arising from the lesser omentum and adherent to the terminal ileum and cecum. The tip of the appendix is seen invaginated into the cyst wall.

Discussion

Though rare, mesenteric cysts exhibit a significant diagnostic challenge due to their diverse clinical presentation and nonspecific imaging characteristics. Their exact etiology remains uncertain, with theories suggesting embryologic lymphatic malformations, trauma, prior infection, or degeneration as contributing factors [9]. In children, these cysts are most commonly asymptomatic and discovered incidentally. However, when complicated by infection, hemorrhage, torsion, or rupture, they may present acutely with pain, distension, or intestinal obstruction [3,9].

The case involved an infected cyst near the adnexa, complicating diagnosis. Sonographically, mesenteric cysts may appear as fluid-filled structures with varying characteristics. This particular lesion showed echogenic clots and septations, resembling hemorrhagic ovarian cysts [6, 7]. The peripheral wall vascularity observed on Doppler is nonspecific and may also be seen in adnexal lesions, particularly with the “ring of fire” sign in ovarian torsion [6]. Furthermore, the non-visualization of the right ovary made the diagnosis even more equivocal [8].

Although certain imaging clues may suggest a mesenteric origin—such as separation from pelvic organs, lack of ovarian continuity, or higher location in the abdominal cavity—these are often subtle and unreliable in emergency settings [10]. To further highlight the overlapping and

distinguishing features, Table 1 compares the sonographic characteristics of mesenteric cysts with those of hemorrhagic ovarian cysts. While both may demonstrate internal echoes, septations, and peripheral vascularity, key differences such as ovarian continuity and anatomical location can aid in differentiation when carefully assessed.

Table 1: Imaging Comparison of Mesenteric Cysts vs. Hemorrhagic Ovarian Cysts

Features	Mesenteric Cyst	Hemorrhagic Ovarian Cyst
Location	Anywhere in mesentery or omentum	Ovarian/adnexal
Internal echoes/septae	May be present in infected/hemorrhagic type	Common due to clotting
Vascularity	Peripheral wall flow, avascular interior	Peripheral rim ("ring of fire")
Ovarian continuity	Absent	Present
Clinical suspicion	Rare, variable presentation	Common in acute lower abdominal pain

Real-time ultrasound features such as compressibility and mobility may help differentiate mesenteric cysts from fixed adnexal masses, but such signs are often absent in inflamed or adherent cysts [9, 10].

Intraoperatively, the cyst was found arising from the lesser omentum—a location exceptionally rare in the pediatric population [2]. Its unusual features include adherence to the terminal ileum and cecum and the invagination of the appendiceal tip into its wall. Similar findings have been sparsely reported and may reflect chronic inflammation or local irritation [9].

Literature indicates that mesenteric cysts are frequently misdiagnosed as appendiceal or ovarian issues due to overlapping clinical and imaging characteristics. Inappropriate surgical intervention may result from this tendency towards gynecologic problems, especially when the ovary is not readily visible. A retrospective review by Yang et al. found many mesenteric and omental cysts were mistakenly labeled as ovarian masses prior to surgery [10].

The reported case emphasizes the importance of surgical exploration—laparoscopic or open—in children with ambiguous imaging findings and clinical concerns. Laparoscopy is minimally invasive and facilitates quick recovery, whereas laparotomy is warranted for extensive dissection or uncertainty. Histopathological examination is crucial for diagnosis confirmation and excluding neoplasia or ectopic ovarian tissue. [4,9].

In pediatric patients, mesenteric cysts should be included in the differential diagnosis of cystic pelvic masses, particularly when ovarian anatomy is ambiguous and ultrasonographic features are unusual. Recognizing these diagnostic mimics is essential to prevent misdiagnosis and ensure prompt surgical intervention [8, 10].

Conclusion

Mesenteric cysts must be included in the differential diagnosis of cystic pelvic masses in children. While ultrasonography is vital, it may not clearly differentiate between adnexal and mesenteric origins if ovarian anatomy is ambiguous. Surgical intervention and histopathological analysis are critical for accurate diagnosis and treatment in these cases.

References

1. de Perrot M, Bründler MA, Tötsch M, Mentha G, Morel P. Mesenteric cysts: Toward less confusion? *Dig Surg*. 2000;17(4):323–8. doi: 10.1159/000018838
2. Ghai S, Metser U. Mesentery, omentum, peritoneum: cystic masses and neoplasms. InAbdominal Imaging 2013 (pp. 1589-1600). Springer, Berlin, Heidelberg.https://doi.org/10.1007/978-3-642-13327-5_170
3. Chou YH, Tiu CM, Lui WY, Chang T. Mesenteric and omental cysts: an ultrasonographic and clinical study of 15 patients. Gastrointestinal radiology. 1991 Dec;16(1):311-https://doi.org/10.1007/BF01887376
4. Kurtz RJ, Heimann TM, Holt J, Beck AR. Mesenteric and retroperitoneal cysts. *Ann Surg*. 1986;203(1):109–12. doi: 10.1097/00000658-198601000-00019
5. Tseng YC, Lee MS, Chang YJ, Wu HP. Acute abdomen in pediatric patients admitted to the pediatric emergency department. Pediatrics & Neonatology. 2008 Aug 1;49(4):126-34. https://doi.org/10.1016/S1875-9572(08)60027-3
6. Shetty J, Reddy G, Pandey D. Role of sonographic gray-scale pattern recognition in the diagnosis of adnexal masses. Journal of Clinical and Diagnostic Research: JCDR. 2017 Sep 1;11(9):QC12. doi: 10.7860/JCDR/2017/28533.10614
7. Levine D, Brown DL, Andreotti RF, Benacerraf BR, Benson CB, Brewster WR, et al. Management of asymptomatic ovarian and other adnexal cysts imaged at US: Society of Radiologists in Ultrasound consensus conference statement. *Radiology*. 2010;256(3):943–54. https://doi.org/10.1148/radiol.10100213
8. Leibman AJ, Kruse B, McSweeney MB. Transvaginal sonography: comparison with transabdominal sonography in the diagnosis of pelvic masses. American Journal of Roentgenology. 1988 Jul 1;151(1):89-92. https://doi.org/10.2214/ajr.151.1.89
9. de Carvalho NM, Lopes Filho JA, Plens IC, Camara VA, de Gois Teixeira CC, Figueiredo PH, de Araujo Junior ON. Mesenteric cyst presenting with acute abdomen pain and bowel obstruction: case report and brief literature review. Annals of Medicine and Surgery. 2020 Oct 1;58:134-7. DOI: 10.1016/j.amsu.2020.09.001
10. Levy AD, Shaw JC, Sobin LH. Secondary tumors and tumorlike lesions of the peritoneal cavity: imaging features with pathologic correlation. Radiographics. 2009 Mar;29(2):347-73. https://doi.org/10.1148/rg.292085189

Fetal Anomaly Scan: A Case Series of Three Fatal Congenital Anomalies

S. Akter[1], F.R. Adrita[2], U. Haque[3], N.K. Tamanna[4], S. Paul[4], A.K. Sarker[5], D. Ghosh[6] and M.F. Uddin[7]

[1.]*Medical officer, Institute of Nuclear Medicine and Allied Sciences, Gopalganj,*
[2]*Medical officer, Institute of Nuclear Medicine and Allied Sciences, Barishal,*
[3]*Medical Officer, 250 Bed Sadar Hospital, Gopalganj,*
[4.]*Scientific officer, Institute of Nuclear Medicine and Allied Sciences, Gopalganj,*
[5.]*Principal medical officer, Institute of Nuclear Medicine and Allied Sciences, Suhrawardy.*
[6.]*Director, Institute of Nuclear Medicine and Allied Sciences, Gopalganj.*
[7.]*Lecturer, microbiology department, Gopalganj Medical College.*

Abstract

Congenital anomalies are responsible for perinatal and neonatal morbidity and mortality. Commonly identified fetal abnormalities during prenatal ultrasonography are central nervous system and cardiovascular system malformations. Early detection of fetal anomalies is very important for making clinical decisions and management in the obstetric field. Presentation of three cases of fatal anomalies diagnosed during antenatal anomaly scans. Between September 2023 and October 2024, a total of 565 pregnant women underwent fetal anomaly scans as a part of routine obstetric ultrasonography at the Institute of Nuclear Medicine and Allied Sciences (INMAS), Gopalganj. Three fetuses were diagnosed with major congenital anomalies which included two cases of anencephaly/exencephaly with craniofacial abnormalities and one with multiple anomalies having sagittal craniosynostosis, sacral meningocele, pulmonary hypoplasia, and genitourinary tract anomaly. All appeared to be fatal. Timely detection of severe fetal anomalies through anomaly scans aids in parental counseling and management with consideration of pregnancy termination.

Keywords: Fetal anomaly, anencephaly, prenatal ultrasound, congenital malformations.

Introduction

Congenital anomalies have a major contribution to perinatal and neonatal mortality worldwide [1]. In Bangladesh, congenital anomalies prevail from 0.18% to 2.54% [2, 3]. The developmental malformations, affecting the central nervous system (CNS), are a significant cause of perinatal morbidity and mortality [4]. The late mid-trimester scan (LMTS) done between 18 to 22 weeks), is considered optimal for detection of a wide range of fetal anomalies due to the advanced development of fetal structures at this stage. This timing allows for a comprehensive assessment of fetal anatomy, improving the detection rates of anomalies [5]. Early detection of anomalies during the LMTS allows for timely counseling and decision-making regarding the pregnancy. This can include discussions about early interventions, delivery planning, and, in some cases, the option of pregnancy termination [6]. Here, we present a series of three fetal cases with severe congenital anomalies identified during anomaly scans at INMAS, Gopalganj.

Case Presentations

Case 1: Fetal Exencephaly/Anencephaly with Facial Cleft

A 19-year-old woman having a singleton pregnancy had an anomaly scan at 28 weeks of the gestational period. Bi-parietal Diameter (BPD) was immeasurable because the cranial bones were absent, and the brain parenchyma appeared to be replaced by an outwardly extruding cystic structure with choroid-like echogenic soft tissue (angiomatous stroma) exposed into the amniotic fluid. No definite cerebral hemisphere or organized lateral ventricle structure was seen. The paired orbits, the corpus callosum, caudate nuclei, thalami, and the cerebellum could not be identified. The facial features suggested the presence of a cleft in the upper lip and palate. The averaged gestational age, measured from femur length (FL) and abdominal circumference (AC), was 28 weeks and 3 days. The final diagnosis was fetal exencephaly or anencephaly with possible cleft lip and palate.

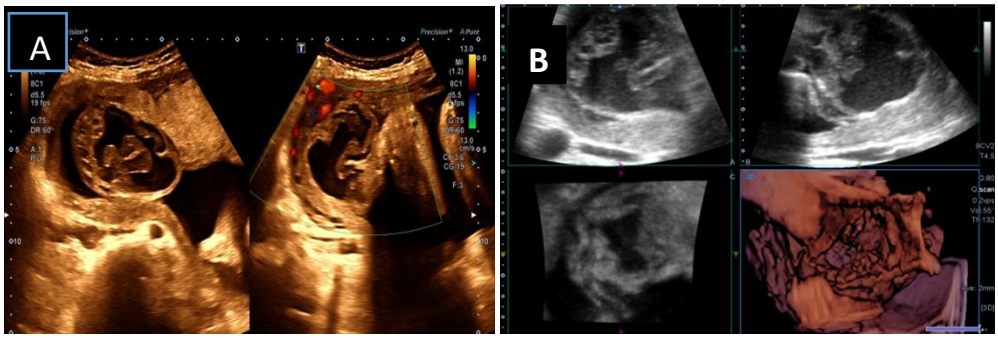

*Corresponding author: usanjida46@gmail.com.

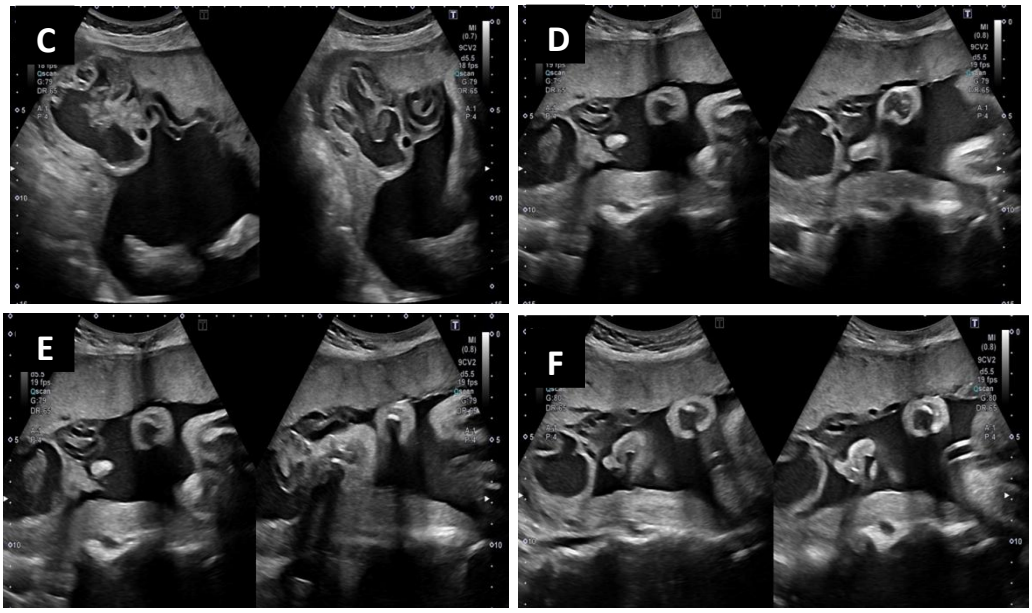

Fig. 1: Pregnancy profile in a 19 years old female. Absent cranial bones (A). No brain parenchyma (B). Outwardly extruding cystic structure with choroid like echogenic soft tissue (angiomatous stroma) exposed into the amniotic fluid (C). No cerebral hemisphere or lateral ventricle structure (D). No paired orbits, corpus callosum, caudate nuclei, thalami or cerebellum (E). Facial features s/o cleft in the upper lip and palate (F).

Case 2: Multiple Anomalies with Suspected Pulmonary Hypoplasia

A 28-year-old female came with a singleton pregnancy. The fetal cranium was antero-posteriorly elongated, indicating possible sagittal craniosynostosis (scaphocephaly). A 20 mm meningocele was noted in the sacral region. The chest appeared short and bell-shaped. The fetal cardiac/thoracic area ratio was 0.62 (ISUOG recommended normal ratio < 0.5), and the thorax-to-abdominal circumference ratio was 0.69, indicating possible pulmonary hypoplasia (ISUOG recommended thoracic/abdominal circumference ratio cutoff ≈ < 0.75-0.80 for pulmonary hypoplasia). The fetal stomach was possibly collapsed, and the urinary bladder was possibly empty. A 50 mm cystic structure is seen in the abdomen, which possibly represents a markedly dilated collecting system in the right kidney. The final diagnosis was IUGR of about 27 weeks size (estimated fetal weight 870 gm; <3rd centile, 30 weeks and 3 days according to L.M.P., cerebro-placental ratio <1), as well as disproportionate growth and anhydramnios, as AFI was <1 cm; fetal scaphocephaly, sacral meningocele, short and bell-shaped chest with possible pulmonary hypoplasia, and possible right-sided megaureter.

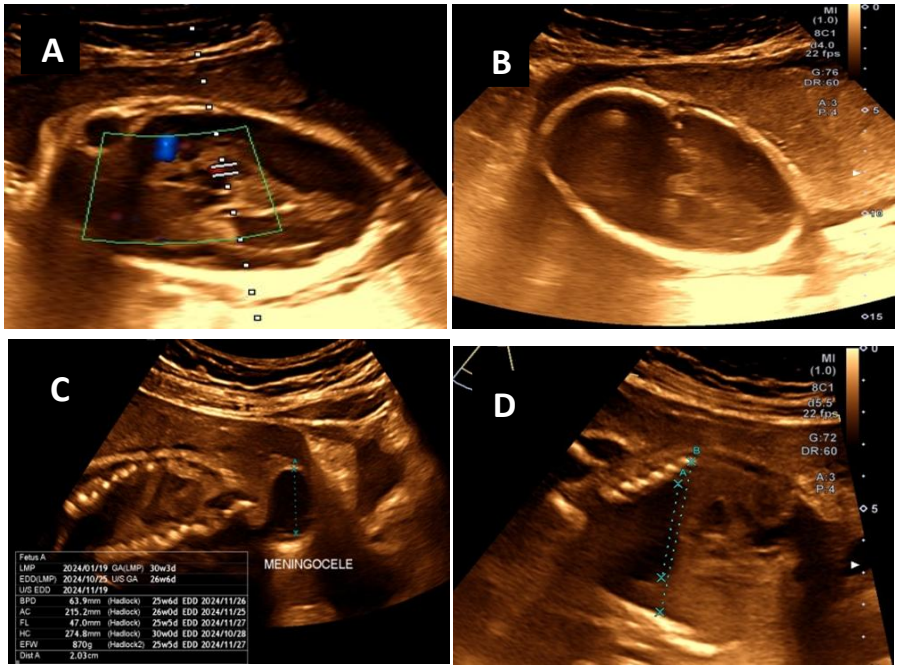

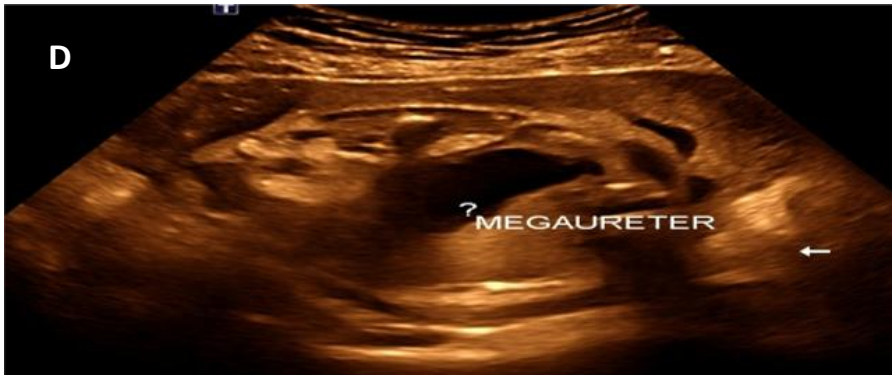

Fig. 2: Pregnancy profile in a 28 years old female. Anhydramnios(A). Antero-posteriorly elongated Cranium (possible sagittal craniosynostosis; scaphocephaly) (B). A 20 mm meningocele was noted in the sacral region (C). Short and bell-shaped chest. Heart-to-chest ratio 0.62 (normal < 0.5) and thorax-to-abdominal circumference ratio 14.3 (normal < 0.8) Possible pulmonary hypoplasia (D). A 50 mm cystic structure in the abdomen which possibly represent markedly dilated collecting system in the right kidney (E).

Case 3: Anencephaly

A 20-year-old woman with a singleton pregnancy of about 6 months was requested a fetal anomaly scan. Ultrasound scan showed absent fetal calvarium above the orbits. Small amounts of floating angiomatous stroma are seen. An abnormal frog-like craniofacial appearance was seen. A 19 × 6 mm elongated tube-like anechoic structure was noted in the right side of the abdomen, below the liver, with no apparent connection with the kidney or urinary bladder. The averaged gestational age, measured from FL and AC, was 21 weeks and 5 days. The final diagnosis was fetal anencephaly with an intra-abdominal anechoic cystic structure that possibly could be a diverticulum.

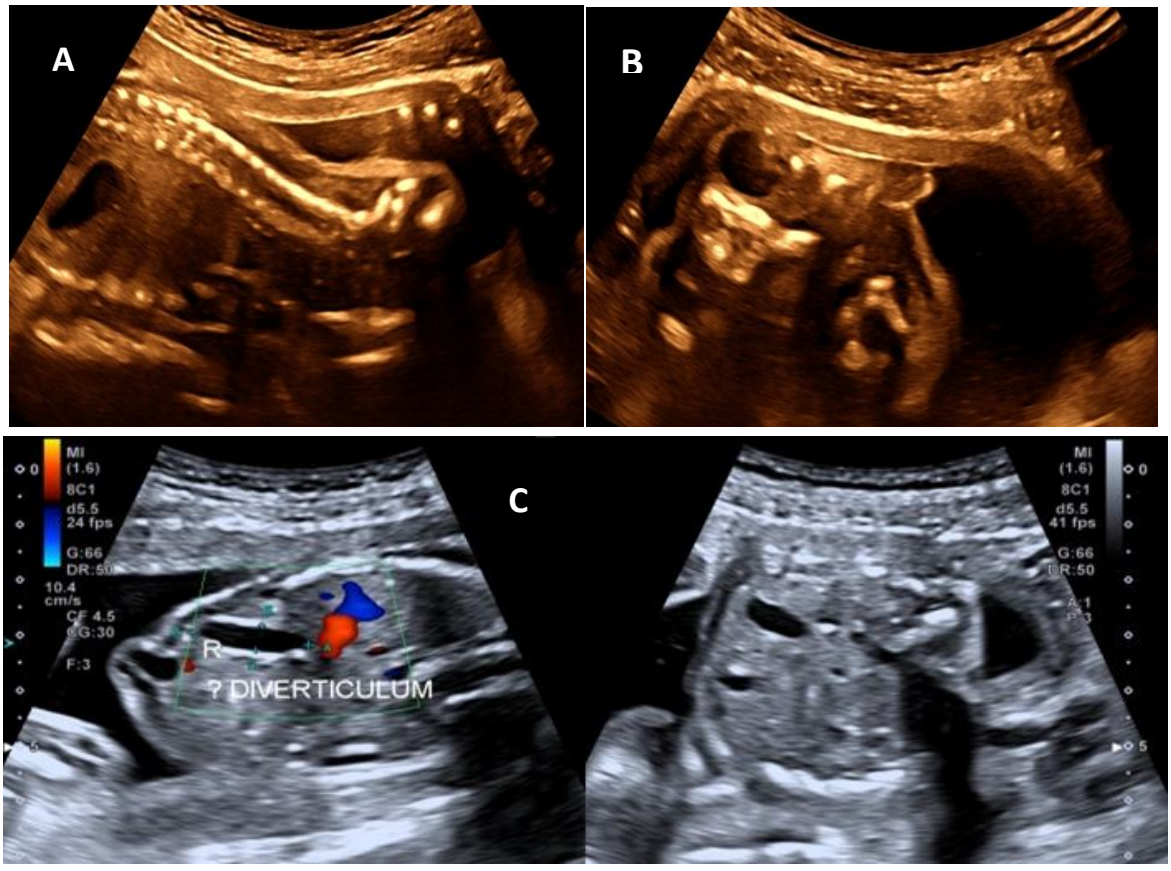

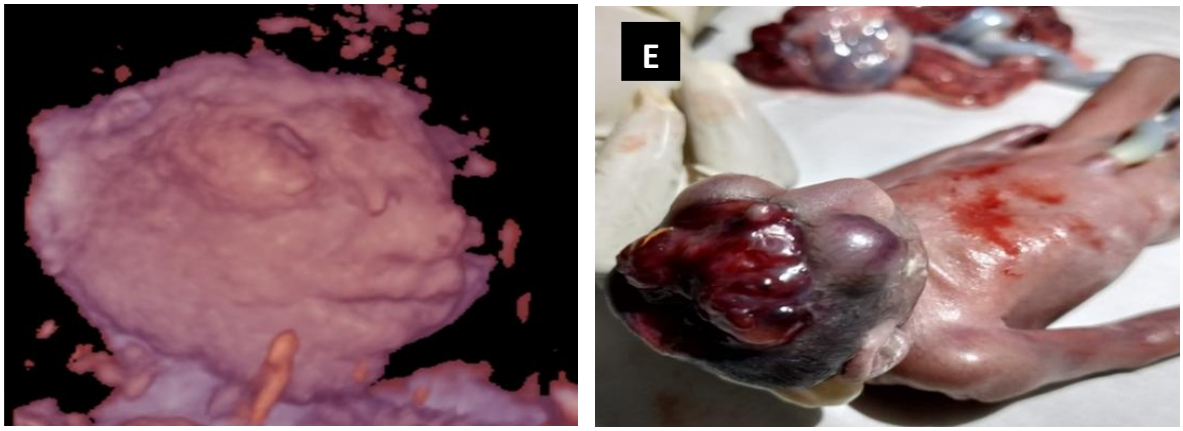

Fig. 3: Pregnancy profile in a 20 years old female. Calvarium was absent above the orbits (A). Small amounts of angiomatous stroma floating in the amniotic fluid is seen (B). A 19 × 6 mm elongated tube like structure was noted in the right side of abdomen, below the liver, with no apparent connection with the kidney or urinary bladder (C). An abnormal frog like craniofacial appearance (D). Images after termination of pregnancy (E).

Discussion

Fetal anomaly scans are essential in prenatal care, with central nervous system (CNS) anomalies being among the most frequently detected [2]. This case series highlighted the features of severe congenital anomalies of three fetuses diagnosed through second-trimester ultrasonography.

The first and third cases show **anencephaly**, a neural tube defect (NTD) that is characterized by the absence of the skull and cerebral hemispheres. In both cases, sonographic features included absent calvarium, presence of floating angiomatous stroma, and disrupted craniofacial morphology (including a "frog-eye" appearance). Early detection and diagnosis in these cases was vital, as anencephaly is inconsistent with life. Findings are accordant with global data, where anencephaly is one of the most common and fatal NTDs (prevalence rate from 5.1 to 8.6 per 10000 pregnancies) that depends on various factors like geographical, genetical, and nutritional ones, mainly folate deficiency [7].

The second case represented a **complex anomaly affecting multiple systems,** which includes cranial **scaphocephaly**, **sacral meningocele**, **short thorax**, **pulmonary hypoplasia,** and **right-sided megaureter**. All the findings are suggestive of multiple congenital anomalies consistent with a syndromic disorder [8]. Out of all features, pulmonary hypoplasia has a poor outcome as it progresses to postnatal respiratory failure [9].

Early diagnosis of fetal anomalies is important for making clinical decisions and helping further management consider the option of pregnancy termination. These cases underlined the importance of routine anomaly scans, also in resource-limited settings. Although major anomalies were diagnosed in only 0.5% out of the 565 pregnancies, their severity emphasizes the role of antenatal imaging in progressing fetomaternal outcomes. Further long-term studies on ultrasonography of anomaly scans in tertiary centers will be helpful to determine the real incidence, severity, and outcomes of fetal anomalies in Bangladesh.

Conclusion

Fetal congenital anomalies like anencephaly and then skeletal dysplasia are common after cardiac anomalies. For diagnosis and better management of a successful pregnancy outcome, an anomaly scan serves as an important component of routine antenatal care, especially in detecting life-threatening fetal abnormalities. This imaging procedure allows early parental counselling, planning for delivery, and immediate postnatal management if required.

References

1. R Verma, Evaluation and Risk Assessment of Congenital Anomalies in Neonates, Children, 8, 862 (2021).
2. A Maheshwari , MZ Alam, MR Tareq, DS Shapna , MH Sohel , N Rehnuma *et al.*, Epidemiological Study of Congenital Anomalies and Risk Factors in Newborn Infants at a Tertiary Care Hospital in Bangladesh, Newborn, 2(3),185–90(2023).
3. R Podder , D Zeba, K Fatema, S Alam, R Bilkis, Prevalence, Pattern and Outcome of Congenital Anomalies in Patients Admitted at a Tertiary Level Hospital in Bangladesh, Bangabandhu Sheikh Mujib Med Coll J., 3(1):27–31(2024).
4. A G tan, N Sethi, S Sulaiman, Evaluation of prenatal central nervous system anomalies: obstetric management, fetal outcomes and chromosome abnormalities, BMC Pregnancy and Childbirth**,** 22**,** 210 (2022).
5. Z Yehudit, M C Rachel, W Ari, S Ori, M Eyal, S H Yitzhak, Detection Rate of Fetal Anomalies in Early Mid-Trimester Compared to Late Mid-Trimester Detailed Scans: Possible Implications for First-Trimester Sonography, J. Clin. Med., 13 (19), 5750 (2024).
6. W Gudu, A Abdulkadir, M Wondafrash, Introducing second-trimester anatomic scanning for improved detection and management of congenital anomalies: Experience from a novice center in East Africa, Int. J. Gyn. Obs., 167 (3), 1237-1242 (2024).
7. N Salari, B Fatahi, R Fatahian *et al*., Global prevalence of congenital anencephaly: a comprehensive systematic review and meta-analysis, Reproductive Health, 19, 201 (2022).
8. S McCormack, C Thompson, K Hennigan, R Khan, N Al-assaf, P71 Skeletal dysplasia- case report of an infant with thanatophoric dysplasia, BMJ. J., 104, 3 (2019).
9. O R Tisekar and A Kumar, Hypoplastic Lung Disease. Updated Jan 2025. In: StatPearls[Internet]. Treasure Island: StatPearls Publishing. Available from: https://www.ncbi.nlm.nih.gov/books/NBK562139/

Hydatid Cysts Involving Multiple Abdominal Organs: A Case Report

T. Sultana[1], S. Hossain[2], T. Biswas[1], T. Hasan[3], R. Afrin[2], M. Hossain[2], R. Parveen[2], R.A. Sharmin[4]
F. Tuz Zohra[5], S.K. Biswas[6]

[1.]*Assistant Professor, Institute of Nuclear Medicine and Allied Sciences (INMAS), Dhaka.*
[2.]*Associate Professor, INMAS, Dhaka.*
[3]*Medical Officer, INMAS, Dhaka.*
[4]*Assistant Professor, INMAS, Mohakhali, Dhaka.*
[5]*Assistant Professor, INMP, AERE, Savar, Dhaka.*
[6.]*Professor & Director, INMAS, Dhaka.*

Abstract

Hydatid disease, or echinococcosis, is a parasitic infection caused by a tapeworm. The larvae of Echinococcus granulosus is a serious, potentially fatal disease that can be found anywhere in the world. The Hydatid cyst is mainly found in the liver (75% of the cases), lung (15%), and other organs, being asymptomatic in most cases and discovered incidentally on a routine abdominal ultrasound or an ultrasound performed for diagnosing other pathologies. A forty-year-old farmer woman with a history of cattle grazing requested an abdominal ultrasound while she was hospitalized with the complaints of mild abdominal pain and gradual abdominal distension for 3 months. Physical examination showed that the patient was afebrile, non-diabetic, non-asthmatic, non-icteric, and normotensive. Routine abdominal ultrasound revealed multiple cysts in the liver, spleen, both ovaries, and multiple areas of the peritoneal cavity. Sonographically, she was provisionally diagnosed with multiple intra-abdominal hydatid cysts. A CT scan of the whole abdomen on the same day also revealed multiple cystic lesions of variable sizes in the peritoneal cavity, liver, both ovaries, and spleen. After administration of IV contrast, no appreciable contrast enhancement was noted. ELISA for Echinococcus antibody on the next day was positive, and eosinophilia was observed in a peripheral blood sample. She has been treated accordingly with a good outcome. Management and treatment approach of hydatid cyst depends on the involved organ, the number of cysts, presence of cystic-biliary communication, secondary bacterial infection and hemorrhage. Thus, it is very important to evaluate each case thoroughly and carefully to achieve the best possible outcome. Patients coming from rural areas with complaints of abdominal pain especially in right hypochondriac region should exclude hepatic hydatid cyst by ultrasonography as the infection is common in rural, underdeveloped areas. Early diagnosis and treatment of hydatid disease can avoid serious complications.

Keywords: Hydatid cyst, Echinococcosis, Echinococcus granulosus, abdominal ultrasound.

Introduction

Hydatid disease (HD), hydatidosis, hydatid cyst (HC) or classical cystic echinococcosis (CE) is a parasitic infection caused by a tapeworm, the larvae of Echinococcus species (Echinococcus granulosus) is a serious disease, potentially fatal which can be found anywhere in the world (1). Hydatid disease is very common parasitosis and health problems in endemic areas (4). The hydatid cyst is mainly found in the liver (75%) where the right lobe of liver is infected in 85% of cases, lung (15%) and other organs, being asymptomatic in most cases and discovered incidentally on a routine abdominal ultrasound or an ultrasound performed for diagnosing other pathologies (1,3). The infection is common in rural, underdeveloped areas where people raise livestock (2). Majority of patients present with early satiety, abdominal pain, abdominal distension, nausea and progressive dyspnea (5)

HD can involve various body organs, but it is less common for it to involve multiple organs simultaneously. The cysts can present unique manifestations in each organ. Any organ can be affected by Echinococcus granulosus except hair and nails. While the liver is the most commonly involved site, unusual affected sites include the heart, bones, spleen, pancreas, breasts, brain, ovaries, adnexae, fallopian tube, thyroid gland, skeletal muscle, common bile duct, etc. Involvement of the peritoneal cavity is only seen in 12% of patients with previous hydatid cyst surgery or micro-rupture of hepatic cysts. CE has variable clinical presentations, ranging from asymptomatic diseases to acute emergencies. Clinical manifestations of this disease depend on multiple factors, such as the organ involved, the site and size of the cyst, the interaction between the expanding cysts and the adjacent organ structures, complications related to cyst rupture, the spread of protoscolices, and bacterial infections. In patients with infection or cyst rupture, the presentation may be severe. These cysts usually remain asymptomatic until they reach a large size and incidentally discovered during course of abdominal pathology workup (9, 11).

According to the World Health Organization (WHO), it is an infection that affects about 1 million people worldwide (6). Hydatid disease (HD) is a significant health problem where animal husbandry is common. Dogs or other carnivores are definitive hosts, whereas sheep or other ruminants are intermediate hosts. Humans are the accidental intermediate host infected by ingestion of eggs through food or water, which develop into cysts, causing

*Corresponding author: taniahayder2009@gmail.com

complications and even death (3). HC affects both sexes equally at all age groups but is more often seen in middle-aged groups (8).

The typical hydatid cyst has a three-layered wall surrounding a fluid-filled cavity; the outer layer is called the pericyst/ectocyst, the middle layer is the exocyst/laminated membrane, and the endocyst/germinal layer is the inner layer (8). The pericyst is composed of inflammatory tissues of host origin. The laminated membrane is a middle, acellular layer that allows for nutrient passage. The inner germinal layer is where the scolices (the larval stage of the parasite) develop (13).

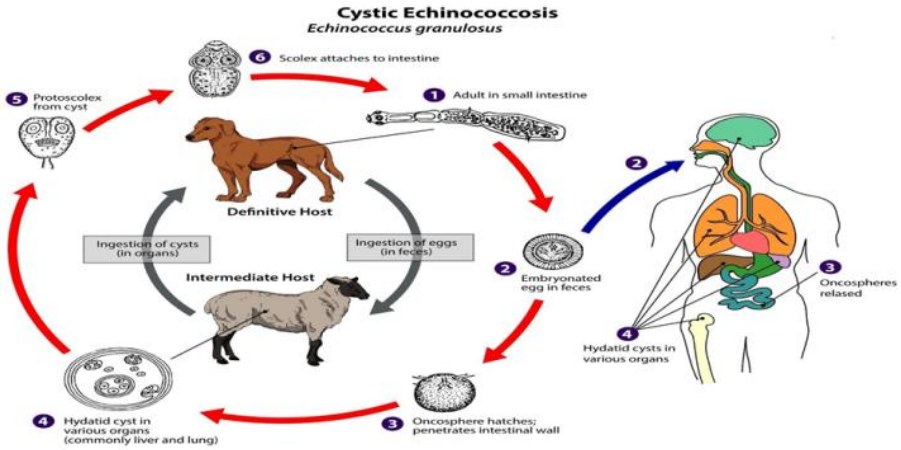

Fig. 1: Schematic presentation of life cycle of cystic echinococcosis

Case Report

A forty years old farmer woman visited INMAS, Dhaka for ultrasonography of whole abdomen. She was admitted in DMCH with the complaints of mild abdominal pain and abdominal distension for last 3 months. She had history of cattle grazing. She was afebrile, non-diabetic, non-asthmatic, non-icteric and normotensive. Ultrasound revealed multiple cysts in liver, spleen, both ovaries and multiple areas of peritoneal cavity. Sonologically, she was diagnosed as multiple intra-abdominal hydatid cysts. CT scan of whole abdomen in the same day also revealed multiple cystic lesions of variable sizes in peritoneal cavity, liver, both ovaries and spleen. After administration of i.v contrast, no appreciable contrast enhancement was noted. ELISA for Echinococcous antibodyin next day was positiveandeosinophilia was observed in a peripheral blood sample. Then she has treated conservatively by Tablet Albendazole 400 mg twice daily for 3 months (1 cycle) with a 14 days drug-free interval when first follow up was done sonologically with a good outcome as decreased in sizes of the cysts and patient's symptoms. Now she is waiting to repeat next 3 months treatment cycle. She received only medical treatment because of the multiple organs involvement.

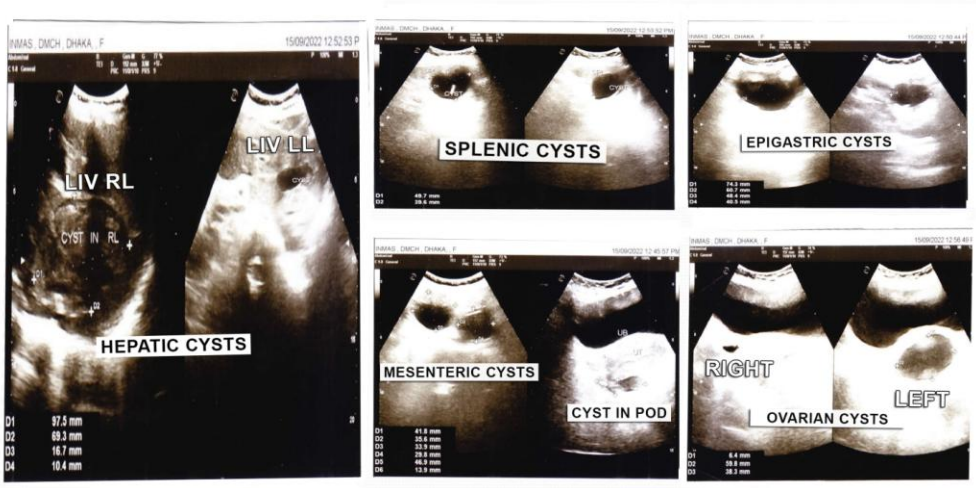

Fig. 2: Sonological images showed hydatid cysts in variousabdominal organs.

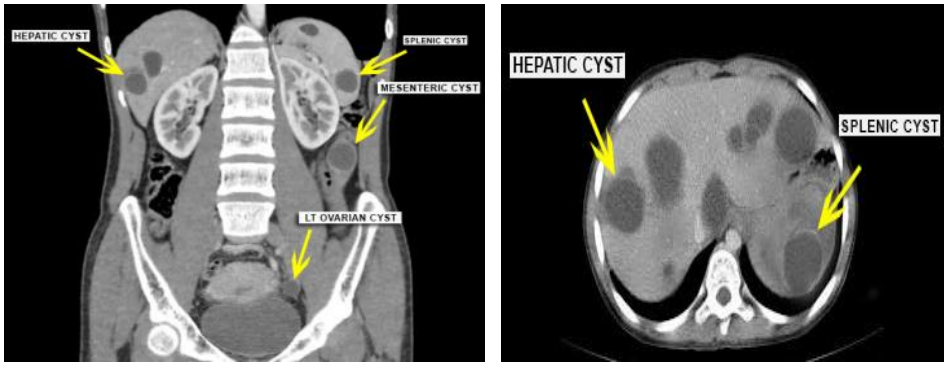

Fig. 3: Coronal and axial CT imagesrevealed hydatid cysts in different abdominal organs.

Discussion

Currently, ten (G1–G10) and lion strain (E. felids) genetically, biologically and morphologically distinct strains of E. granulosus have been identified from different parts of the world. The different strains of the parasite were reported to have different epidemiological and socio-economical significances and geographical ranges. From these, four of them (G1, G2, G5 and G6) were reported to infect humans in different parts of the world (2).

Echinococcus has a complicated taxonomy. CE is more common than AE. Although AE in animals in endemic areas are relatively common, human cases are rare. AE is more serious and poses a much greater health threat to people than CE causing parasitic tumors that can form in the liver, lungs, brain, and other organs. If the cysts are to rupture while in the body, whether during surgical extraction of the cysts or by trauma to the body, the person would most likely go into anaphylactic shock and have high fever, pruritus, edema of the lips and eyelids, dyspnea, stridor and rhinorrhea (10).

Diagnosis of HC can be done by ultrasonography (US), computed tomography (CT), magnetic resonance imaging (MRI), blood for Echinococcous antibody. Histories as contact with wildlife, vegetables not properly washed, travel to endemic areas are also helpful for diagnosis. Among them, US and CT remain the preferred imaging (1, 6, 8).

Both cystic echinococcosis and alveolar echinococcosis are often complicated to treat, sometimes requiring extensive surgery and/or prolonged drug therapy. There are 4 options for the treatment of cystic echinococcosis: percutaneous treatment of the hydatid cysts with the PAIR (Puncture, Aspiration, Injection, Re-aspiration) technique, surgery, anti-infective drug treatment (ex: albendazole which may be needed for years). “Watch and wait” may be the another option (1, 6, 10). Pre and postoperative albendazole reduces the rate of recurrence (8). Pre-operative courses of Albendazole should be considered in order to sterilize the cyst, decrease the chance of anaphylaxis, decrease the tension in the cyst wall (thus reducing the risk of spillage during surgery) and to reduce the recurrence rate post-operatively. Intra-operatively, the use of hypertonic saline or 0.5% silver nitrate solutions before opening the cavities tends to kill the daughter cysts and therefore prevent further spread or anaphylactic reaction (3).

Although the liver and lungs are the most involved organs, hydatid cysts can occur in all viscera and soft tissues with variable degrees of sign and symptoms (7). The reported case revealed the disease involving multiple abdominal organs like the liver, spleen, both ovaries, and multiple areas of the peritoneal cavity. De, Utpal, revealed a patient where the patient presented in emergency with a primary hydatid cyst as a peritoneal cyst followed by an appendicular lump. Disseminated intra-abdominal hydatid disease may occur following rupture of the hydatid cyst into the peritoneal cavity, producing secondary echinococcosis. Rarely, cysts may develop de novo in the peritoneal cavity without involvement of any other intra-abdominal organs (3).

Salih, A. M., et al. showed a case of abdominal wall HC and mentioned that HC of skeletal muscle is a rare condition accounting for 1–4% of all HC diseases (7). Alan, B., et al. conducted a case of hydatid cysts, which were present on the liver, right adrenal region, and also on the hepatic flexure (right hepatic colon lumen). In that case, a cyst adjacent to the ascending colon had ruptured into the colon lumen and developed a cystocolonic communication (4). Tekin, R., et al. presented a case of a 15-year-old girl with hydatid cysts in multiple organs, including the lungs, liver, spleen, kidney, and right iliacus and gluteus maximus muscle (5).

Abebe, E., et al. conducted a study of forty-two patients in Ethiopia where the liver was the primary site of the disease in 30 (71.4%) cases, the right lobe being the main side affected, 73%. Retroperitoneum was involved in 3 patients. The spleen, mesentery, and peritoneum were also harboring the cyst as a primary site (8). Ghassemof, H., et al. described a case where an open laparotomy was scheduled with the primary suspicion of peritonitis, but during the surgery, five omental cysts were observed within different parts of the abdomen (9).

Jangjoo, A., et al. found a case of isolated greater omentum solid mass, a rare manifestation of hydatid disease. Abdominal ultrasonography revealed a multiseptated cyst with a honeycomb appearance, which was suggestive of hydatid disease. Peritoneal hydatidosis is a common side

effect of surgical treatment for a hepatic or splenic hydatid cyst. Primary peritoneal hydatidosis is unusual, with almost about 2% of all instances of abdominal hydatid diseases. Dissemination into the peritoneal cavity can occur by lymphatic or systemic circulation. The third option is that a superficial hepatic hydatid cyst ruptured spontaneously, causing considerable peritoneal involvement (10). Burgazli, K.M., et al., revealed unusual localization of a primary hydatid cyst as a subcutaneous mass in the left paraumbilical region by using ultrasonography (12).

Conclusion

The management and treatment approach of hydatid cysts depends on the involved organ, the number of cysts, the presence of cystic-biliary communication, secondary bacterial infection, and hemorrhage.

The management and treatment approach of hydatid cysts depend on the involved organ, the number of cysts, the presence of cystic-biliary communication, secondary bacterial infection, and hemorrhage. Thus, it is very important to evaluate each case thoroughly and carefully to achieve the best possible outcome. Patients coming from rural areas with the complaints of abdominal pain, especially in the right hypochondriac region, should exclude hepatic hydatid cyst by ultrasonography, as the infection is common in rural, underdeveloped areas. Early diagnosis and treatment of hydatid disease can avoid serious complications. US is a very good noninvasive, available, and cheap imaging modality for patients suspected to have IAHC. Further imaging adds very little. Hydatid disease should be kept in mind in the differential diagnosis of multiple cysts in patients living in endemic areas.

References

1. Botezatu, C., Mastalier, B., Patrascu, T., 2018.Hepatic hydatid cyst - diagnose and treatment algorithm. J Med Life, Jul-Sep;11(3), pp.203-209.
2. Regassa, B., 2019. Review on Hydatidosis in Small Ruminant and its Economic and Public Health Significance. Dairy and Vet Sci J, 11(2).
3. De, Utpal, 2009. Primary abdominal hydatid cyst presenting in emergency as appendicular mass: a case report. World J Emerg Surg, Apr 3,4 (13).
4. Alan, B., Kapan, M., Budak, H., Kuzu, H., 2016. Intra-Abdominal Hydatidosis: Hydatid Cyst Related to Right Hepatic Colon Lumen. Journal of Clinical and Experimental Investigations, 7 (2),pp.207-210.
5. Tekin, R., Onat, S., Tekin, R.C., 2016. Hydatid cysts in a patient with multiple organ involvement Images in Infectious Diseases. Rev Soc Bras Med Trop,July-August, 49(4), pp.534.
6. Mihetiu, A., 2024. Optimized Strategies for Managing Abdominal Hydatid Cysts and Their Complications. Diagnostics, 14(13),1346.
7. Salih, A. M., Kakamad, F.H., Hammood, Z. D., Yasin, B., Ahmed, D. M., 2017. Abdominal wall Hydatid cyst: A review a literature with a case report. International Journal of Surgery Case Reports,37, pp.154-156.
8. Abebe, E., Kassa, T., Bekele, M., Tsehay, A., 2017. Intra-Abdominal Hydatid Cyst: Sociodemographics, Clinical Profiles, and Outcomes of Patients Operated on at a Tertiary Hospital in Addis Ababa, Ethiopia. Journal of Parasitology Research, 2017, 4837234.
9. Ghassemof, H., Esfehani, R. J., 2015. Hydatid Disease Presented as Acute Abdomen, an Interesting Incidental Finding: A Case Report. Arch Clin Infect Dis, October; 10(4), 29632.
10. Jangjoo, A., Norouzi, Asl. S., Azadmanesh, Y., Zandbaf, T., 2023. Isolated greater omentum solid mass, a rare manifestation of hydatid disease; A Case Report And Review Of Literature. Caspian J Intern Med, 14 (2), pp.386-390.
11. Jain, S., Khanduri, S., Sagar, U. F., Yadav, P., Husain, M., Imam, T., 2019. Abdominal Hydatidosis: Unusual and Usual Locations in a North Indian Population. Cureus, 11(4), 4380.
12. Burgazli, K.M., Ozdemir, C.S., Ozdemir, E. B., Mericliler, M., Polat, Z.P., 2013. Unusual localization of a primary hydatid cyst: a subcutaneous mass in the paraumbilical region. European Review for Medical and Pharmacological Sciences,17,pp.1766-1768.
13. Golzari, S. EJ., Sokouti, M., 2014. Pericyst: The outermost layer of hydatid cyst. World J Gastroenterol,Feb 7;20(5), pp.1377-1378.

Unilateral Extraconal Orbital Lymphoma Diagnosed by FDG PET-CT: A Rare & Interesting Case Report

M. Nusrat[1], Z. Jabin[2], A. Naznin[3], S. Das[4], K.R. Ahmed[4], J. Sultana[5], R.-Ul-Haque[5] and I. Tabassum[5]

[1]Medical Officer, Institute of Nuclear Medicine & Allied Sciences (INMAS), Mitford.
[2]Director & Professor, [3]Senior Medical Officer, [4]Scientific Officer, [5]Medical Officer, Institute of Nuclear Medicine & Allied Sciences (INMAS), Suhrawardy.

Abstract

Orbital lymphoma is an uncommon malignancy involving the structures of the orbit, accounting for a small proportion of extranodal lymphomas. Its insidious onset and nonspecific symptoms often delays diagnosis. We report a rare case of primary orbital lymphoma in a middle- aged female patient presenting with progressive unilateral proptosis and painless orbital swelling Following clinical suspicion, imaging was performed and the diagnosis was confirmed histopathologically. Whole-body FDG PET-CT was subsequently done in our department for staging. Multiple immunologic and molecular techniques have aided in the distinction between MALT lymphoma and other lymphoproliferative disorders which has identified the tissue markers of prognostic significance. Modern imaging modalities such as PET-CT provide invaluable tools for accurate staging and treatment planning. Besides radiotherapy and chemotherapy, a variety of new treatment options have emerged in the management including monoclonal antibody.

Keywords: Orbital lymphoma, Extranodal lymphoma, Proptosis, Non-Hodgkin's lymphoma.

Introduction

Lymphomas are neoplasms of lymphoid tissue that results from the proliferation of malignant B and T lymphocytes. It usually originates in lymph nodes but they can also arise from any organ in the body (extranodal disease) [1]. Extranodal marginal zone B-cell lymphoma (low-grade B-cell lymphoma of mucosa-associated lymphoid tissue [MALT] type) is a distinctive type of lymphoma that usually arises from mucosa or other epithelial structures [2]. Ocular adnexal lymphomas are a heterogeneous group of malignancies, comprising approximately 1% to 2% of non-Hodgkin lymphomas (NHLs) and 8% of extranodal lymphomas [3]. They constitute the most frequent malignant tumors of the ocular adnexa and reported up to 55% of all orbital tumors [4]. The majority of primary ocular adnexal lymphoma, is marginal zone lymphoma of mucosa-associated lymphoid tissue (MALT) type [5]. Clinical presentation is often nonspecific, mimicking inflammatory or benign orbital lesions, which makes early diagnosis challenging [6]. PET-CT plays a vital role in diagnosing extranodal sites and staging.

Case Presentation

A 54-year-old, hypertensive female presented with a history of painless swelling of the left eye for 5 months, associated with progressive proptosis and mild diplopia. There was no history of trauma, pain, vision loss, or systemic symptoms such as fever, night sweats, or weight loss. On examination, left eye shows mild proptosis, upper eyelid fullness and restricted ocular motility (especially on upward gaze). However, no lymphadenopathy or organomegaly was found. B- mode USG of her left eye showed, an oval hypoechoic lesion at lateral aspect of orbit at the site of lacrimal gland with evidence of bilateral vitreous hemorrhage. Possible differential diagnosis was given as 1. lymphoma and 2. granulomatous inflammation. She was advised for CT scan of orbit which revealed an enhancing extraconal mass in left orbit involving the lacrimal gland, superior and lateral recti muscles. The patient was then advised for histopathology, which revealed, lymphoproliferative disease and followed by immunohistochemistry showing extranodal marginal zone lymphoma (CD20, CD19 & BCL2 were strongly positive). After that, patient was referred to our department for PET-CT scan which revealed an FDG avid (SUVmax 4.8), homogeneously enhancing, extraconal soft tissue mass involving the lacrimal gland and adjacent extraocular muscles (levator palpebrate superioris, superior and lateral recti) causing proptosis, without bony erosion- Consistent with orbital lymphoma. However, no enlarged or hypermetabolic lymph node was seen in head- neck, thorax or abdominopelvic region. The patient was diagnosed as stage IE according to Lugano staging.

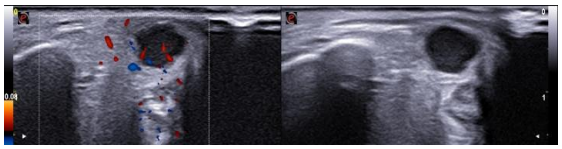

A B

Fig. 1: B-mode scan of swelling over left eye reveals an almost oval hypoechoic lesion (arrow head) at supero-lateral aspect of orbit, which on color flow shows internal vascularity (arrow mark).

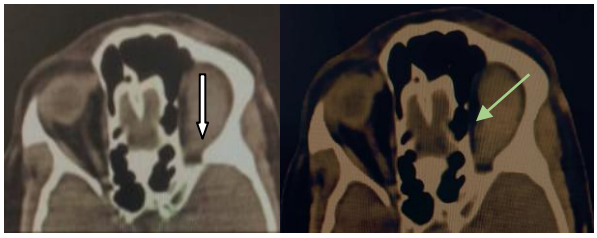

A B

Fig. 2: Pre-contrast (A) axial image on CT scan of orbit shows a lobulated soft tissue density mass (thick arrow) at extraconal compartment of left orbit. Post contrast (B) scan shows almost homogeneous enhancement of the mass (thin arrow).

*Corresponding author: mariomnusrat91@gmail.com.

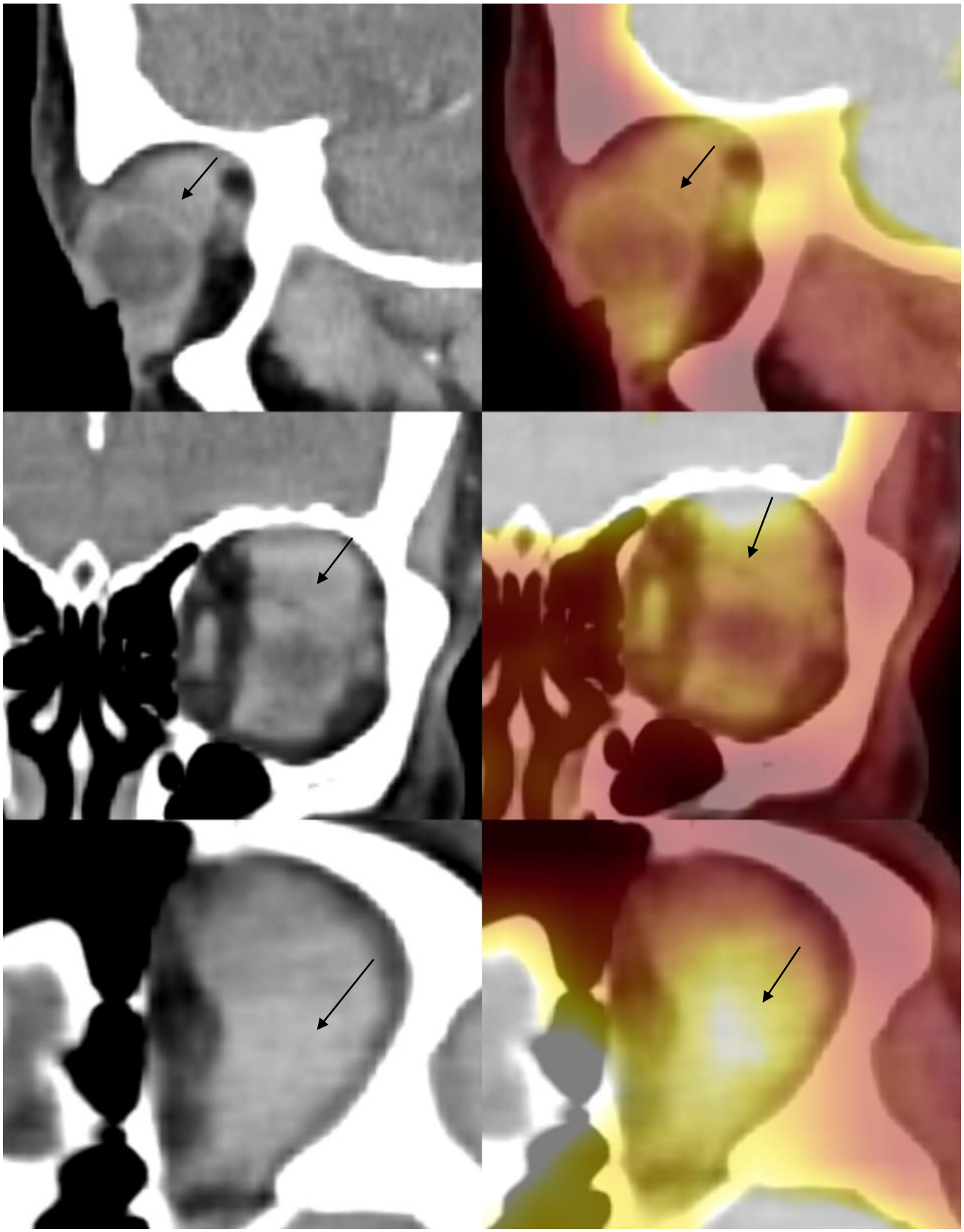

Fig. 3: Multiple axials, coronal and sagittal CT and PET- CT images of patient show a hypermetabolic, almost homogeneously enhancing, extraconal mass lesion (shown by arrow mark) at supero-lateral aspect of left orbit.

NUCLEAR SCIENCE AND APPLICATIONS

GENERAL INFORMATION AND INSTRUCTIONS TO AUTHOR(S)

Scope of the Journal

"Nuclear Science and Applications" is an indexed journal (ISSN 1016-197X). It provides scope for publication of original scientific research work of high standards in the form of full research articles, reviews and short communications. Preference is given to the works that are related to applications of nuclear science and technology.

Original papers should describe a complete investigation and short communications may represent important data, methods etc that are yet to be concluded or the original full paper manuscripts that are not justified for publication as original papers and recommended to be published as short communications by the designated reviewers. Review works of considerable scientific interests are also welcome. Efforts are made to publish the journal regularly in June and December every year.

Manuscript Submission

Manuscript should be submitted to the Chief Editor at any time of the year. Receipt of the manuscript will be acknowledged. Unpublished manuscript will not be returned to the author. Short communication should not exceed two published pages. Review articles may have an extended length but it must be approved by the editorial board.

Manuscript Preparation

In order to maintain uniformity and standard, the intending authors are requested to prepare their manuscripts by considering the following general requirements:

1. Two copies of the manuscript should be submitted and authors are advised to retain a third copy with them for reference.
2. The manuscript should be typed in double spacing on one side of A4 size paper and computer composed with 12 pt. Times New Roman Font. Adequate margin (2.54 cm on all sides) should be kept.
3. Each paper must contain a reasonable number of keywords in order to indicate the main topics discussed in the paper and to provide basic terms for indexing.
4. The manuscript should be arranged in the following order: Title of the paper, Author(s) name and affiliations, Abstract (not exceeding 150 words), Keywords, Introduction, Materials and Method/Experimental, Results and Discussion, Conclusion(s), Acknowledgement (if any) and Reference(s).
5. The Number of Tables and Figures should be kept as minimum as possible. Same data should not be reproduced both in table & figure.
6. Tables and Figures should be numbered in Arabic numerals. Figures should be eligibly drawn either with laser printer or Indian black ink. Tables and Figures should be placed in the same order in which they appear in the text.
7. S. I. units should be used to express scientific quantities.
8. For references inside the text the following style should be followed at the appropriate places: e.g. [1] or [1.3] or [5-8] etc. The references of author's name(s) in the text should appear in the following form: e.g., Chowdhury [1], Rahman and Khan [3], Hasan et al [5] etc.

   The references arranged at the end of the paper should be written in the following order:

   (a) Reference to a journal publication: author's name, title of the paper, abbreviated name of the journal (internationally approved form, sources: http://www.nlm.nih.gov/tsd/serials/lji.html), volume number in bold face, page number (range) and year of publication in first bracket: e.g.: S.Z. Sarker, A. Karim and M.M. Rahman, Complex Permeability Spectra of Polycrystalline Li-Cd Ferrites, Nucl. Sci. and Appl., 22(2), 10-17 (2010).

   (b) Reference to a book: author's name, book's title, edition, publisher's name and place, page numbers and year of publication in braket: e.g.: C.S. Piper, Soil and Plant Analysis, 2nd ed. (USA: John Wiley) 580-600 (2002).

   (c) Reference to Proceedings: author's name, title of the paper, Symposium Conference name, paper number, date and place. Corresponding author should be identified in the footnote of the first page with E-mail address.
9. Authors are advised to strickly follow the structure of the paper published recently in NSA in order to speed up the review and editing processes.

Contact Details

All Communications should be addressed to the Executive Editor, Editorial Board, Nuclear Science and Applications, Scientific Information Division, Bangladesh Atomic Energy Commission, Paramanu Bhaban, E-12/A, Agargaon, Sher-e-Bangla Nagar, Dhaka-1207. E-mail: sidhaec@gmail.com, Phone: 8802-223374972.

Subscription Information

The subscription rate for each volume is Tk. 500.00 for domestic or US $20.00 for foreign subscribers. Interested subscribers may contact the Executive Editor, Editorial Board, Nuclear Science and Applications, Scientific Information Division, Bangladesh Atomic Energy Commission for collection of the publication or of the reprints.

Discussion

Orbital lymphoma can be seen from 15 to 70 years, but most cases occur between 50 and 70 years. The major contributing factor to the pathophysiology of orbital lymphoma is immunocompromised conditions like ageing, HIV/AIDS, or immunosuppressive drugs. Recently, studies have suggested that pathogens like Chlamydia psittaci, H. pylori, and some viruses are associated with orbital lymphoma [7].

Orbital lymphoma involves the conjunctiva, lacrimal gland, soft tissues of the eyelid, or extraocular muscles and most commonly extraconal in location [8].

The clinical presentation is generally nonspecific and depends on the location of the lymphoma. Vision is usually preserved, as infiltration of the globe or optic nerve is rare. Orbital presentation is most commonly observed as a painless palpable mass in the superolateral quadrant. It may lead to proptosis, ptosis, diplopia, or abnormal ocular movement. Patients may also demonstrate a pink or red "salmon patch" of swollen conjunctiva or conjunctival hyperemia. Enlarged lacrimal gland can displace the eyeball inferomedially. Swelling and prolapse may also occur in the eyelid [6].

The differential diagnosis for masses includes inflammatory/metabolic disease (orbital inflammatory pseudotumor, thyroid orbitopathy, sarcoidosis) and neoplasm (lacrimal tumors, lymphoma and metastasis). Exceptional diseases—such as Sjögren, Wegener, and Kimura diseases are rare possibilities. Cystic retrobulbar lesions (such as dermoid and epidermoid cyst or mucocele) are differentials for intraconal ones [9].

MRI helps delineate the lesion, but histopathology with immunophenotyping remains the diagnostic gold standard. Combined PET-CT allows assessment of metabolism and morphologic data in one single examination. However, PET metabolism shows no significant difference between histologically graded lymphomas in low or high malignancy. So, we can find high metabolic activity (high SUV_{max} values) in the active stage of low-grade lymphomas also [10].

Treatment depends on disease stage. Localized disease (stage IE) is highly radiosensitive with excellent prognosis. Disseminated disease requires systemic chemotherapy, typically R-CHOP (rituximab, cyclophosphamide, doxorubicin, vincristine, and prednisone) [11].

Conclusion

Orbital lymphoma should be an important consideration in any patient presenting with progressive, painless proptosis. Early recognition and biopsy are essential for accurate diagnosis and optimal treatment. Proper staging done by PET-CT scan can help in timely and proper management.

References

1. Moussaly E, Nazha B, Zaarour M, Atallah JP. Primary non-Hodgkin's lymphoma of the spine: a case report and literature review. World journal of oncology. 2015 Oct 26;6(5):459.
2. Bailey EM, Ferry JA, Harris NL, Mihm MC, Jacobson JO, Duncan LM. Marginal zone lymphoma (low-grade B-cell lymphoma of mucosa-associated lymphoid tissue type) of skin and subcutaneous tissue: a study of 15 patients. The American journal of surgical pathology. 1996 Aug 1;20(8):1011-23.
3. Freeman C, Berg JW, Cutler SJ. Occurrence and prognosis of extranodal lymphomas. Cancer. 1972 Jan;29(1):252-60.
4. Margo CE, Mulla ZD. Malignant tumors of the orbit: analysis of the Florida Cancer Registry. Ophthalmology. 1998 Jan 1;105(1):185-90.
5. McKelvie PA, McNab A, Francis IC, Fox R, O'Day J. Ocular adnexal lymphoproliferative disease: a series of 73 cases. Clin Exp Ophthalmol. 2001 Dec;29(6):387-93.
6. Gerbino G, Boffano P, Benech R, Baietto F, Gallesio C, Arcuri F, Benech A. Orbital lymphomas: clinical and radiological features. Journal of Cranio-Maxillofacial Surgery. 2014 Jul 1;42(5):508-12.
7. Chaurasiya BD, Agrawal G, Chaudhary S, Shah S, Pradhan A, Lavaju P. Orbital lymphoma masquerading as orbital cellulitis. Case Reports in Ophthalmological Medicine. 2021;2021(1):8832783.
8. Sharma T, Kamath MM, Fekrat S, Scott IU. Diagnosis and management of orbital lymphoma. American Academy of Ophthalmology. 2015.
9. Priego G, Majos C, Climent F, Muntane A. Orbital lymphoma: imaging features and differential diagnosis. Insights Imaging. 2012 Aug;3(4):337-44. doi: 10.1007/s13244-012-0156-1. Epub 2012 Apr 18. PMID: 22695946; PMCID: PMC3481074.
10. Klingenstein A, Garip- Kuebler A, Mueller- Lisse UG, Hintschich C. Combined positron emission tomography/computed tomography for diagnosis and monitoring of orbital adnexal lymphoma. Acta ophthalmologica. 2018 Sep;96(6):e712-7.
11. Ferreri AJ, Dolcetti R, Du MQ, Doglioni C, Resti AG, Politi LS, De Conciliis C, Radford J, Bertoni F, Zucca E, Cavalli F, Ponzoni M. Ocular adnexal MALT lymphoma: an intriguing model for antigen-driven lymphomagenesis and microbial-targeted therapy. Ann Oncol. 2008 May;19(5):835-46.

NUCLEAR SCIENCE AND APPLICATIONS

GENERAL INFORMATION AND INSTRUCTIONS TO AUTHOR(S)

Scope of the Journal

"Nuclear Science and Applications" is an indexed journal (ISSN 1016-197X). It provides scope for publication of original scientific research work of high standards in the form of full research articles, reviews and short communications. Preference is given to the works that are related to applications of nuclear science and technology.

Original papers should describe a complete investigation and short communications may represent important data, methods etc that are yet to be concluded or the original full paper manuscripts that are not justified for publication as original papers and recommended to be published as short communications by the designated reviewers. Review works of considerable scientific interests are also welcome. Efforts are made to publish the journal regularly in June and December every year.

Manuscript Submission

Manuscript should be submitted to the Chief Editor at any time of the year. Receipt of the manuscript will be acknowledged. Unpublished manuscript will not be returned to the author. Short communication should not exceed two published pages. Review articles may have an extended length but it must be approved by the editorial board.

Manuscript Preparation

In order to maintain uniformity and standard, the intending authors are requested to prepare their manuscripts by considering the following general requirements:

1. Two copies of the manuscript should be submitted and authors are advised to retain a third copy with them for reference.
2. The manuscript should be typed in double spacing on one side of A4 size paper and computer composed with 12 pt. Times New Roman Font. Adequate margin (2.54 cm on all sides) should be kept.
3. Each paper must contain a reasonable number of keywords in order to indicate the main topics discussed in the paper and to provide basic terms for indexing.
4. The manuscript should be arranged in the following order: Title of the paper, Author(s) name and affiliations, Abstract (not exceeding 150 words), Keywords, Introduction, Materials and Method/Experimental, Results and Discussion, Conclusion(s), Acknowledgement (if any) and Reference(s).
5. The Number of Tables and Figures should be kept as minimum as possible. Same data should not be reproduced both in table & figure.
6. Tables and Figures should be numbered in Arabic numerals. Figures should be eligibly drawn either with laser printer or Indian black ink. Tables and Figures should be placed in the same order in which they appear in the text.
7. S. I. units should be used to express scientific quantities.
8. For references inside the text the following style should be followed at the appropriate places: e.g. [1] or [1.3] or [5-8] etc. The references of author's name(s) in the text should appear in the following form: e.g., Chowdhury [1], Rahman and Khan [3], Hasan et al [5] etc.

   The references arranged at the end of the paper should be written in the following order:

   (a) Reference to a journal publication: author's name, title of the paper, abbreviated name of the journal (internationally approved form, sources: http://www.nlm.nih.gov/tsd/serials/lji.html), volume number in bold face, page number (range) and year of publication in first bracket: e.g.: S.Z. Sarker, A. Karim and M.M. Rahman, Complex Permeability Spectra of Polycrystalline Li-Cd Ferrites, Nucl. Sci. and Appl., 22(2), 10-17 (2010).

   (b) Reference to a book: author's name, book's title, edition, publisher's name and place, page numbers and year of publication in braket: e.g.: C.S. Piper, Soil and Plant Analysis, 2nd ed. (USA: John Wiley) 580-600 (2002).

   (c) Reference to Proceedings: author's name, title of the paper, Symposium Conference name, paper number, date and place. Corresponding author should be identified in the footnote of the first page with E-mail address.
9. Authors are advised to strickly follow the structure of the paper published recently in NSA in order to speed up the review and editing processes.

Contact Details

All Communications should be addressed to the Executive Editor, Editorial Board, Nuclear Science and Applications, Scientific Information Division, Bangladesh Atomic Energy Commission, Paramanu Bhaban, E-12/A, Agargaon, Sher-e-Bangla Nagar, Dhaka-1207. E-mail: sidhaec@gmail.com, Phone: 8802-223374972.

Subscription Information

The subscription rate for each volume is Tk. 500.00 for domestic or US $20.00 for foreign subscribers. Interested subscribers may contact the Executive Editor, Editorial Board, Nuclear Science and Applications, Scientific Information Division, Bangladesh Atomic Energy Commission for collection of the publication or of the reprints.

CONTENTS

NUCLEAR SCIENCE AND APPLICATIONS VOLUME 30 NUMBER 1 & 2 June, December 2025

Price Tk. 500.00 (For Bangladeshi), US$ 20.00 (For Foreigner)

Published by: Bangladesh Atomic Energy Commission, E-12/A, Agargaon, Sher-e-Bangla Nagar Dhaka-1207, Bangladesh

Printed by: Natundhara Printing Press, 314/D Elephant Road (Kataban Dhal), Dhaka-1205
Cell: 01711019691, 01911294855, Email: natundhara2014@gmail.com